



UNIVERSITY
OF ŽILINA

Faculty of Management Science and Informatics

**DEVELOPMENT, VALIDATION AND APPLICATION
OF THE CELL CLUSTER MODEL**

DISSERTATION THESIS

Registration number: 28360020243003

Ing. MICHAL MULÍK

Study program: Applied Informatics
Field of study: Informatics
Affiliation: Faculty of Management Science and Informatics,
Department of Software Technologies,
University of Žilina
Supervisor: prof. Mgr. Ivan Cimrák, Dr.

Žilina, 2024

Statutory declaration

I declare that I have prepared the assigned dissertation thesis independently, under the professional guidance of the thesis supervisor and have used only the literature listed in the thesis.

In Žilina, 6. May 2024

Author sign

Annotation

Type of the work:	Dissertation thesis
Academic year:	2023/2024
Title of the work:	Development, validation and application of the cell cluster model
Author:	Ing. Michal Mulík
Supervisor:	prof. Mgr. Ivan Cimrak, PhD.
Language:	English
Number of pages:	135
Number of figures:	86
Number of tables:	12
Number of equations:	10
Number of references:	48
Keywords:	Microfluidics, Cell Cluster Model, Computer Simulations, Fluid Dynamics, Shear Flow, Dean Flows, Adhesion Strength, Cell Separation, Constricted Capillaries

Acknowledgements

First of all, I would like to thank my supervisor Prof. Mgr. Ivan Cimrák, Ph.D., with whom I have worked throughout my doctoral studies. Thanks to him, I learned what research means and how to present it correctly to the public. Without his help, I would not have been able to work on several interesting projects. Moreover, I never dreamed that I would ever communicate, let alone collaborate, with an MIT research group in America. Few people ever have the opportunity in their lifetime to see MIT in Boston up close and even to walk around its campus. The view of the Empire State Building in New York is still vivid in my mind's eye. I will never forget that experience. None of this would have been possible without my mentor's undying passion for science and research. It was a privilege to be mentored by someone with extensive experience of research abroad. Slowly but surely, over the course of three years, I came to realise that research doesn't have to be as boring and uninteresting as it is commonly described by those around me.

I must also mention my supervisor assistant, Mgr. Iveta Jančigová, who gave me my first insight into research issues and guided me until she left the faculty. Together with my supervisor, they formed a strong research duo in the field of biomedical informatics. For me personally, it was always an experience to be part of their conversation when I didn't have as much insight into the topic as I do now. So, I thank her for the opportunity to move forward, as she taught me to tolerate constructive criticism.

I would like to thank our entire research team, who together were able to find solutions that were sometimes not obvious at first glance. Namely, our team leader Prof. Dr. Ivan Cimrák and fellow colleagues Dr. Monika Smiešková and Dr. Alžbeta Bugáňová. I have worked very well with you during my studies. I would especially like to thank Betka for guiding me through my studies and answering all my questions.

I would also like to thank all my colleagues in the legendary RA316 office, where I experienced everything from the greatest disappointments and surprises to the greatest successes. It has been an honour to share with you all the feelings of three years of study, my fellow heroes Dominika Petříková, Lucia Piatriková, Adam Mračko and Samuel Molčan. I know that you will never get lost in life.

Finally, my family is my greatest support. A family without whom everything would be indescribably harder. Words cannot describe the constant support I have received from you. I have always had a place to come back to when things were at their worst, something I cherish and will always cherish. It is only in the hardest of times that we know

who we can count on. Mum, Dad and brother, thank you for believing in me and always being there for me. I'm grateful that we have such an honest relationship. And of course I'm also grateful to my three little fur babies, my cats Iris, Luna and Jackie, who are also part of the family and a big part of the support. They always know how to put a smile on my face.

At the very end, thanks to my dearest friends, who are the strongest fuel for my heart that beats also for them. "A good friend is a connection to life — a tie to the past, a road to the future, the key to sanity in a totally insane world." — Lois Wyse

Abstract

Michal Mulík: Development, validation and application of the cell cluster model (Dissertation thesis) – The University of Žilina, Faculty of Management Science and Informatics, Department of Software Technologies – Supervisor: prof. Mgr. Ivan Cimrák, Dr. – Qualification level: Doctor of Philosophy in Applied Informatics – EDIS Žilina, April 2024 – 135 pages.

The work is concerned with an in-depth investigation of the dynamics of cancer cell clusters in a variety of fluid environments, including scenarios such as shear flow, branched channels, constricted capillaries and Dean inertial flow. The introductory section outlines the biomedical motivation for this research and clarifies the specific objectives underlying the study. A comprehensive review of the state of the art in the relevant literature introduces critical concepts such as shear flow, bifurcations, Dean flow and the simulation tools, including ESPResSo and PyOIF, used throughout the research.

A substantial part of the thesis consists of investigating the behaviour of cell clusters in shear flow at the wall and in simple bifurcation channels. The analysis includes various parameters such as shear rate, elasticity and initial rotation and elucidates how these factors affect the trajectory and deposition patterns of the cell clusters. In addition, the paper addresses the passage of cell clusters through constricted capillaries and introduces an innovative model of flattened cancer cells. A thorough comparison of the simulation results with experimental data will be performed, providing a critical validation of the model's predictive capabilities.

A key aspect of the research is the role of Dean inertial flows in the separation of cancer cell clusters. The theoretical underpinnings of inertial concentration and separation are elucidated, and computational models are systematically employed to analyse flow patterns within both the initial and evolved channel geometries. The presentation of the results includes both quantitative and qualitative analyses that provide a detailed understanding of the effectiveness of inertial flows in achieving cluster separation.

The thesis extends its focus to the collaborative efforts with the MIT research group, clarifying the goals of the collaboration, navigating the inherent trade-offs, and presenting the joint findings resulting from these collaborative efforts.

At the conclusion of this scientific exploration, the thesis provides a comprehensive summary that brings together the findings, advances and real-world applications resulting

from the developed cancer cell clustering model. At the very end, there are sections dedicated to references and a list of publications that have been published progressively during the thesis.

Keywords: Microfluidics, Cell Cluster Model, Computer Simulations, Fluid Dynamics, Shear Flow, Dean Flows, Adhesion Strength, Cell Separation, Constricted Capillaries

Abstrakt

Michal Mulík: Vývoj, validácia a aplikácia modelu zhlukov buniek (dizertačná práca) – Žilinská univerzita v Žiline, Fakulta riadenia a informatiky, Katedra softvérových technológií – Školiteľ: prof. Mgr. Ivan Cimrák, Dr. – Stupeň odbornej kvalifikácie: philosophiae doctor v odbore Aplikovaná informatika – EDIS Žilina, April 2024 – 135 strán.

Práca sa zaoberá hĺbkovým skúmaním dynamiky zhlukov rakovinových buniek v rôznych fluidných prostrediach, ktoré zahŕňajú scenáre, ako je šmykový tok, rozvetvené kanály, zúžené kapiláry a dekanové inerciálne toky. V úvodnej časti sa uvádza biomedicínska motivácia tohto výskumu a objasňujú sa konkrétne ciele, ktoré sú základom štúdie. Komplexný prehľad súčasného stavu v príslušnej literatúre uvádza kritické pojmy, ako je šmykový tok, bifurkácie, Deanov tok, a simulačné nástroje vrátane ESPResSo a PyOIF, ktoré sa použili počas celého výskumu.

Podstatnú časť práce tvorí skúmanie správania sa zhlukov buniek v šmykovom toku pri stene a v jednoduchých bifurkačných kanáloch. Analýza zahŕňa rôzne parametre vrátane šmykovej rýchlosti, elasticity a počiatovej rotácie a objasňuje, ako tieto faktory ovplyvňujú trajektóriu a spôsoby usadzovania zhlukov buniek. Okrem toho sa práca zaoberá prechodom zhlukov buniek cez zúžené kapiláry, pričom zavádza inovatívny model sploštených rakovinových buniek. Vykonáva sa dôkladné porovnanie výsledkov simulácie s experimentálnymi údajmi, ktoré poskytuje kritické overenie predpovedných schopností modelu.

Kľúčovým aspektom výskumu je úloha Deanových inerciálnych tokov pri separácii zhlukov rakovinových buniek. Teoretické základy inerciálneho sústredenia a separácie sú objasnené a výpočtové modely sú systematicky nasadené na rozbor vzorcov prúdenia v rámci počiatovej aj rozvinutej geometrie kanála. Prezentácia výsledkov zahŕňa kvantitatívne aj kvalitatívne analýzy, ktoré umožňujú detailné pochopenie účinnosti inerciálnych tokov pri dosahovaní separácie zhlukov.

Ďalej práca rozširuje svoj záber na spoločné úsilie s výskumnou skupinou MIT, objasňuje ciele spolupráce, orientuje sa v prirodzených kompromisoch a prezentuje spoločné zistenia vyplývajúce z tohto spoločného úsilia.

Na záver tohto vedeckého skúmania práca poskytuje komplexné zhrnutie, ktoré spája poznatky, pokroky a reálne aplikácie vyplývajúce z vyvinutého modelu zhlukovania

rakovinových buniek. Na samotnom konci sa nachádzajú časti venované referenciám a zoznamu publikácií, ktoré boli postupne v priebehu práce vypublikované.

Kľúčové slová: mikrofluidika, model zhľuku buniek, počítačové simulácie, dynamika tekutín, šmykové prúdenie, deanové toky, adhézna sila, separácia buniek, zúžené kapiláry

Contents

1	Introduction	23
1.1	Biomedical motivation.....	24
1.2	Objectives of this thesis	26
1.3	Dissertation thesis outline.....	28
2	State of the art.....	30
2.1	Shear flow and narrow capillaries	30
2.2	Bifurcations.....	31
2.3	Dean flow	31
2.4	ESPReso and PyOIF.....	32
2.4.1	Simulation box.....	33
2.4.2	Fluid properties	33
2.4.3	Bonded interactions.....	34
2.4.4	Non-bonded interactions	36
2.4.5	Attraction-repulsion interactions	38
2.5	Cell and cluster models	41
2.5.1	Red blood cell	41
2.5.2	Circulating tumour cell.....	41
2.5.3	Circulating tumour cell cluster	42
2.6	Method of joining cells into a cluster	43
2.6.1	A well-known method of creating a cluster model.....	44
2.6.2	Method of creating our cluster model	45
2.7	Hardware and supporting software	47
3	Exploring cell cluster behavior in simple shear flow and in bifurcated channels	50
3.1	Modelling cell clusters and their dynamics in near-wall shear flow.....	50
3.1.1	Cluster parameters and models.....	51
3.1.2	Results based on different shear rate, elasticity and initial rotation	57
3.1.3	Conclusion	66
3.2	Simple bifurcation analysis	67
3.2.1	Cluster parameters.....	67
3.2.2	Microfluidic channel geometry	69
3.2.3	Contact area measurement	70
3.2.4	Results of simulation experiments	71
3.2.5	Conclusion	74
4	Passage of Cell Cluster Through Constricted Capillary: Viscosity Analysis	75

4.1	Theory about cluster flowing through constricted capillaries	75
4.2	Flattened cancer cell model.....	77
4.3	Modified flattened cancer cell model.....	78
4.4	Comparison between our simulations and biological experiments	79
4.5	Conclusion	81
5	Dean Inertial Flows for Cell and Cluster Separation	82
5.1	Theory about inertial focusing and object separation	82
5.2	Computational models.....	83
5.3	Dean flow in curved channels.....	85
5.4	Inertial focusing and separation using initial geometry.....	86
5.4.1	Microfluidic channel geometry.....	86
5.4.2	Fluid set-up.....	87
5.5	Results using initial geometry	89
5.5.1	Quantitative analysis of flow patterns	90
5.5.2	Qualitative analysis of flow patterns	98
5.6	Inertial focusing and separation of clusters in using larger geometry	99
5.6.1	Microfluidic channel geometry.....	100
5.6.2	Fluid set-up.....	101
5.6.3	Cell and cluster models.....	102
5.7	Results using larger geometry	104
5.7.1	Quantitative analysis of flow patterns	105
5.7.2	Qualitative analysis of flow patterns	111
5.8	Collaboration with MIT Research Group: Goals and Trade-offs.....	112
5.8.1	Microfluidic channel geometry.....	113
5.8.2	Fluid set-up.....	113
5.8.3	Cell models.....	115
5.9	Results from collaboration with MIT Research group.....	115
5.9.1	Quantitative analysis of flow patterns	117
5.10	Conclusion.....	120
5.10.1	Inertial focusing and separation using initial geometry	120
5.10.2	Inertial focusing and separation using larger geometry	120
5.10.3	MIT Research group collaboration	121
6	Discussion	123
6.1	Contribution of this thesis	125
6.2	Future research directions.....	126
7	References.....	127

Attachments	132
List of publications.....	133

List of Figures

Figure 1: Differential strength of cell bonds and their behaviour in a constricted capillary [3].....	24
Figure 2: Spiral microchannel with trapezoidal cross-section [5].....	26
Figure 3: Example of triangulation on a red blood cell	35
Figure 4: Schematic illustration with interactions highlighted	36
Figure 5: Red blood cell model	41
Figure 6: Circulating tumour cell model	41
Figure 7: Circulating tumour cell model with inner particles	42
Figure 8: Basic cancer cell cluster model	43
Figure 9: Transparent model of a cancer cell cluster with inner particles [33]	43
Figure 10: Creating a cluster of cells according to Andersen [2]	44
Figure 11: Different geometric shapes formed by a cluster of cells [2]	45
Figure 12: 2D illustration of the process for creating a flat adhesion surface	46
Figure 13: a) LJ potential coupling b) Unified network model [32].....	46
Figure 14: The process of joining two cells into a cluster with a unified network [33]	47
Figure 15: Optical microscopy images of Colo205 cells and their clusters [2]	51
Figure 16: Cluster geometries bi, L3, tetra and tri as represented by the two models. Model I in the first row, Model II in the second row [33]	52
Figure 17: Joining process for creating a bi-cluster from two single cells [33].....	53
Figure 18: Cell separation based on the micropipette principle [33].....	54
Figure 19: Cell separation using fluid flow [33]	55
Figure 20: Contact area of two cells (represented by the number of contact points) in a pulling experiment with different magnitudes of separation forces (in nN) [33].....	56
Figure 21: Illustration of x-axis and z-axis orientation	58
Figure 22: Model I. cluster centre coordinate z_c and minimum coordinate z_{min} shown after rescaling for (left) stiff doublet, (right) soft doublet [33]	58
Figure 23: Doublet z_c and z_{min} at shear rate $400s^{-1}$. (left) Strong adhesion (Model I) (right) Weak adhesion (Model II) [33].....	59
Figure 24: Contact area of stiff tri (left), L3 (mid), tetra (right) clusters at a shear rate of $400s^{-1}$. Only the tri-cluster Model I continue to repeatedly contact the wall. All other types investigated tend to move away from the wall [33]	59
Figure 25: Contact area of stiff tri (left), L3 (mid), tetra (right) clusters at a shear rate of $100s^{-1}$ [33].....	60

Figure 26: Tri-cluster with different stiffness in flow with shear rate $100s^{-1}$. (left) Model I strong adhesion, (right) Model II weak adhesion [33]	61
Figure 27: Model II, stiff bi, tri, L3 and tetra-clusters in flow with initial cell-cell contact areas are coloured red [33].....	63
Figure 28: Snapshots of bi-cluster in shear flow near the wall [33].....	63
Figure 29: Snapshots of tri-cluster in shear flow near the wall [33].....	63
Figure 30: Snapshots of L3-cluster in shear flow near the wall [33].....	63
Figure 31: Snapshots of tetra-cluster in shear flow near the wall [33].....	63
Figure 32: Heatmaps for soft and stiff clusters using both models [33].....	64
Figure 33: Doublet orientations named x, y, z and general ($\pi/4, \pi/6, 2\pi/5$) [33]	65
Figure 34: Minimum Z coordinate of the same stiff doublet cluster with four different initial orientations [33]	65
Figure 35: Contact area of the same stiff doublet cluster starting from four different orientations: x, y, z and general at a shear flow of $100s^{-1}$ [33]	66
Figure 36: Difference between the contact area of soft (left) and stiff (right) cells [32].....	68
Figure 37: Simple bifurcation model [32]	69
Figure 38: Fluid velocity in the model [32]	70
Figure 39: Contact area of clusters of two types - doublet, with different elasticity [32]....	71
Figure 40: Soft (a) and stiff (b) doublet in horizontal initial position entering the bifurcation, both Model I	71
Figure 41: Contact area of clusters of two types - L4, with different elasticity [32]	72
Figure 42: Soft (a) and stiff (b) L4 cluster entering the bifurcation, both Model I	72
Figure 43: Horizontal and vertical initial position of the doublet [32]	73
Figure 44: Soft (a) and stiff (b) doublet in vertical initial position entering the bifurcation, both Model I	73
Figure 45: Comparison of strong and medium adhesion [3]	75
Figure 46: Different adhesion forces in the same cluster will cause a change in the order of the cells in the chain as they pass through the capillary [3]	76
Figure 47: First model of a flattened cancer cell filled with internal particles.....	77
Figure 48: Initial model of a constricted capillary with a cancer cell.....	77
Figure 49: Final model of a flattened cancer cell filled with internal particles	79
Figure 50: A modified model of a constricted capillary with a cancer cell	79
Figure 51: Comparison of the speed of cells and cell clusters with respect to their size and the size of the constricted capillary [3] - biological experiment	80
Figure 52: Comparison of the velocity of cells and cell clusters with respect to their size and the size of the constricted capillary - our model.....	80

Figure 53: Different cell cluster models.....	84
Figure 54: Competing inertial forces in curved channels	85
Figure 55: Rectangular channel geometry	86
Figure 56: 72 Simulations after 21 passes, where each column represents different fluid velocity (Re = 19.2, 37.3, 48, 64).....	91
Figure 57: Behavior Analysis of Different Models in cross-section $60 \times 52 \mu m$ with 40 passes.....	92
Figure 58: Behavior Analysis of Different Models in cross-section $80 \times 40 \mu m$ with 40 passes.....	92
Figure 59: Behavior Analysis of Different Models in cross-section $100 \times 32 \mu m$ with 40 passes.....	93
Figure 60: Particle Dynamics in Fluid Flow: Varied Models in a cross-section $60 \times 52 \mu m$.	94
Figure 61: Particle Dynamics in Fluid Flow: Varied Models in a cross-section $80 \times 40 \mu m$.	95
Figure 62: Particle Dynamics in Fluid Flow: Varied Models in a cross-section $100 \times 32 \mu m$	96
Figure 63: Comparative Analysis of Three Diagrams for a cross-section $80 \times 40 \mu m$	97
Figure 64: Cluster Motion in High Reynolds Microfluidic Channels	99
Figure 65: Separation of cells in repeating curved channel.....	100
Figure 66: Detailed description of cross-section $160 \times 80 \mu m$	100
Figure 67: Detailed description of cross-section $200 \times 64 \mu m$	101
Figure 68: The fluid flowing in the channel at the Reynolds number of 64	102
Figure 69: Cluster models and their cuts	103
Figure 70: Sizes of cell and cluster models	103
Figure 71: Deformations of a two-in-line cluster.....	104
Figure 72: Quantitative Analysis of Cluster Dynamics CTC with $10 \mu m$ and 80 passes ..	106
Figure 73: Quantitative Analysis of Cluster Dynamics CTC with $15 \mu m$ and 80 passes ..	106
Figure 74: Quantitative Analysis of Cluster Dynamics CTC with $20 \mu m$ and 80 passes ..	106
Figure 75: 96 Simulations after 40 passes and 80 passes (green rectangles), where each column represents different fluid velocity (Re = 19.2, 37.3, 48, 64).....	108
Figure 76: Settling Dynamics of Elastic CTCs in a $200 \times 64 \mu m$ S-Channel Across Varied Fluid Velocities with 40 passes.....	109
Figure 77: S-Channel Dynamics: Largest Solid Two-in-Line Cluster at High Velocity	111
Figure 78: Detailed description of curved channels with cross-sections $160 \times 48 \mu m$, $200 \times 48 \mu m$ and $250 \times 48 \mu m$ from the top to the bottom	113
Figure 79: The fluid flowing in the channel at the Reynolds number of 171.56	114
Figure 80: Sizes of cell models.....	115

Figure 81: Cell positions at the beginning (left) and at the end (right) of the experiment using $Re = 35.44$	116
Figure 82: Cell positions at the beginning (left) and at the end (right) of the experiment using $Re = 178.79$	116
Figure 83: Comparison between positions taken after 8 S-section passes with $Re = 35.44$ (left) and $Re = 178.79$ (right).....	117
Figure 84: Comparisons between our simulations (blue) and MIT experiments (orange) after 8 S-section passes using $8\mu m$ solid CTCs	118
Figure 85: Comparison between different cells using cross-section $200 \times 48\mu m$ after 40 S-section passes	118
Figure 86: Comparison between different cells using cross-section $160 \times 48\mu m$ after 40 S-section passes	119

List of Tables

Table 1: Time comparison between machines.....	49
Table 2: Cluster characteristics [33]	51
Table 3: Simulation parameters of cluster membrane [33].....	56
Table 4: Adhesion parameters of cell clusters [33]	56
Table 5: Physiological shear rates in vessels with different diameters [41], [42]	57
Table 6: Contact area metrics without recording the initial contact [33].....	62
Table 7: Values of local elasticity coefficients at lower and higher elasticity	68
Table 8: Typical diameters/thicknesses of blood vessel walls in humans in μm	75
Table 9: Fluid parameter in rectangular channel with cross-section $80 \times 40 \mu m$	87
Table 10: Overview of cluster parameters	89
Table 11: Fluid velocity parameters.....	102
Table 12: Fluid parameter in curved channels with different cross-sections	114

List of Equations

Equation 1: Defining cell-cell adhesion using the LJ potential.....	38
Equation 2: HAT potential.....	39
Equation 3: DPD – Conservative Force	39
Equation 4: DPD – Dissipative Force	40
Equation 5: DPD – Random Force	40
Equation 6: Calculation for shear rate	57
Equation 7: Calculation of cluster contact area.....	70
Equation 8: Definition of Dean Number	85
Equation 9: Volumetric flow rate.....	88
Equation 10: Reynolds number	88

List of Abbreviations

Abbreviation	English meaning
CIF	C ell I n F luid
RBC	R ed B lood C ell
WBC	W hite B lood C ell
CTC	C irculating T umour C ell
ESPResSo	E xtensible S imulation P ackage for R esearch on S oft Matter Systems
MIT	M assachusetts I nstitute of T echnology
PyOIF	P ython O bject – I n – F luid
RBC	R ed B lood C ell
LJ	L ennard – J ones interaction
DPD	D issipative P article D ynamics
HAT	H ard – A sphere – T ree
CTMs	C irculating T umour M icro emboli
LB	L attice – B oltzmann

List of Symbols

Symbol	English meaning
k_s	Modulus of elasticity
k_b	Bending modulus
k_{al}	Local area preservation module
k_{ag}	Module for preserving the total area
k_v	Volume conservation module
r	Distance between two particles
r_{cut}, r_{cutoff}	Cutoff distance
r_{min}	Distance where repulsion turns into attraction
r_{core}	Hard – core diameter
r_{ij}	Distance between particles i and j
ϵ	Energy scale

σ	Magnitude of the Random Force
$r_{\text{soft}}, \sigma_{\text{soft}}$	Soft – Core Diameter
A	Parameter determining the strength of the interaction
γ	Dissipative coefficient
$\omega(r_{ij})$	Weight function that typically decreases smoothly with r_{ij}
v_{ij}	Relative velocity of particles i and j
\hat{r}_{ij}	Unit vector pointing from particle i to particle j
η_{ij}	Random number drawn from a Gaussian distribution
$\dot{\gamma}$	Shear rate
Q	Volumetric flow rate
w	Width of microchannel
h	Height of microchannel
n	Total number of all grid points contained in the cluster
n_{contact}	Total number of all grid points closer to the dividing wall
S_{cluster}	Total surface area of the cluster
tT	Total contact time during a specified period
A_{contact}	Variable contact area
A_{max}	Total contact area
TICA	Time integral of contact area over a designated time span
Re	Reynolds number
R_c	Curvature radius of the channel
D_h	Hydraulic diameter of the channel

1 INTRODUCTION

Recently, there has been an increasing focus on modelling biomedical processes, particularly those occurring in the human body. Various methods are used for such modelling, including the use of medical instruments, microscopes and microfluidic devices to collect data. However, this approach is labour-intensive, difficult to perform and expensive. An alternative is the use of computer simulations that closely mimic actual processes. By creating a simulation environment with flowing fluid and objects such as particles, red blood cells or cancer cells, we can efficiently tailor the properties of the model for specific investigations.

Cancer, especially its metastatic process, is a widely discussed and critical topic worldwide. With countless people succumbing to cancer every year, active participation in global research into its treatment is imperative. One potential strategy to prevent metastasis is to minimise contact between clusters and vessel walls. Recognising that cancer cell clusters pose a greater threat than individual circulating cancer cells (CTCs), alternatives include preventing cluster fusion after passage through narrowed capillaries or developing devices to separate red blood cells and blood plasma from cancer cell clusters. Although prototypes exist, further development remains time consuming and costly.

The Cell-in-fluid Biomedical Modelling and Computations Group (Cif-BMCG) at the University of Žilina [1] is committed to continually enhancing a model divided into fluid and elastic objects. The Lattice-Boltzmann method models the fluid (representing blood plasma or saline) using the Navier-Stokes equations. Objects such as particles and cells can be inserted into the fluid, and the triangular network forming the cell membrane allows deformation in the fluid.

The work focuses on the analysis of cancer cells or clusters, studying their properties and behaviour in different environments. Investigations include movement through constricted capillaries, adhesion strength and size of contact area with model walls under shear flow. In addition, Dean flows are studied to observe cell separation. The introduction discusses the biomedical motivation and outlines the main objectives of the thesis. Subsequent sections present simulation results, accompanied by tables, figures and graphs, along with suggestions for further development. Scientific articles support the thesis, providing inspiration and theoretical knowledge.

The research is timely and in line with global efforts in microfluidic devices. The incorporation of cell models in simulations aims to provide valuable results to address challenging questions in the field.

1.1 Biomedical motivation

From a biological point of view, microfluidic channels have great potential for studying complex biological processes. Our initial focus was to explore methods to effectively separate clusters of cancer cells into individual cells, which are technically considered to be single entities or singletons.

The human body has a complex network of blood vessels that branch into smaller and narrower capillaries through which cells or clusters must pass. A promising strategy to inhibit metastasis involves guiding clusters of cancer cells through narrowed capillaries, causing significant deformation and, in some cases, rearrangement of the cells within the cluster. This approach aims to break down the more dangerous clusters into individual cells, making them safer for the human organism.

In a study referenced as [2], researchers investigated how the strength of bonds between cells in a cluster influences their arrangement, deformation, and division within a narrowed capillary. Figure 1 presents the outcomes of this exploration, categorizing bonds into three types: strong, medium, and weak adhesion, in that order as mentioned in [3]. The study showed that the likelihood of cluster splitting in the constricted capillary is highest for the weakest bonds, and conversely, the likelihood is lowest for clusters with the strongest adhesion. This finding provides valuable information for understanding and manipulating the dynamics of cancer cell clusters in constricted capillaries, offering potential avenues for reducing metastatic risk.

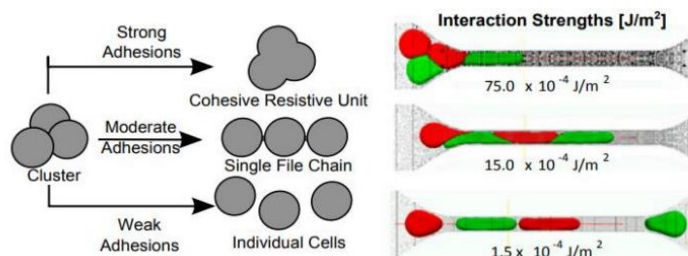


Figure 1: Differential strength of cell bonds and their behaviour in a constricted capillary

[3]

The adhesion strength between two cells can be quantified using different methods. One approach involves virtually stretching the cells apart with hypothetical tweezers and assessing the force required to separate them. Another method is based on shear stress, a naturally occurring force within the channel that acts on the cell as it flows. The magnitude of the shear stress is primarily influenced by the chosen channel width and fluid velocity, with the highest shear stress concentrated at the capillary walls.

This phenomenon allows the study of the conditions under which a cell cluster can disintegrate into individual cells, as well as how different cluster geometries encounter the capillary walls. It is well known that increased contact between a cluster and the walls, as well as a larger contact area, increases the likelihood of a cancerous tumour forming at that location [4]. Fragmentation of a cluster with weak cell-to-cell adhesion can also occur, for example, when the cluster hits a bifurcation wall at a higher speed. To investigate this scenario, we will use a simple bifurcation model in which the shear stress, the impact and the contact of the cluster with the wall are considered in this phenomenon. This comprehensive investigation aims to deepen our understanding of the dynamics involved and provide valuable insights into the potential formation of cancerous tumours at specific sites.

Our most recent and extensive research focuses on the study of the Dean effect and a detailed analysis of its implications. The significance of this is that in secondary inertial flows, the movement of cells in different segments of the channel stabilises over time. This phenomenon holds out the prospect of effective separation of different objects commonly found in the blood. Initially, different types of cells are scattered across the width of the channel, but over time they organise themselves into distinct, uniform flows.

For example, smaller cells, such as red blood cells (RBCs), may cluster around the edges of the channel, while larger cancer cells may concentrate towards the centre. This dynamic offers the potential to separate red blood cells from cell clusters. A visual representation of this separation is depicted in Figure 2 of [5], where we can see the mixture of white blood cells (WBC) and circulating tumour cells (CTC), illustrating the phenomenon in a helix model. Our aim is to explore the possibility of using Dean flow to separate cancer cluster geometries from other cluster geometries or individual cells.

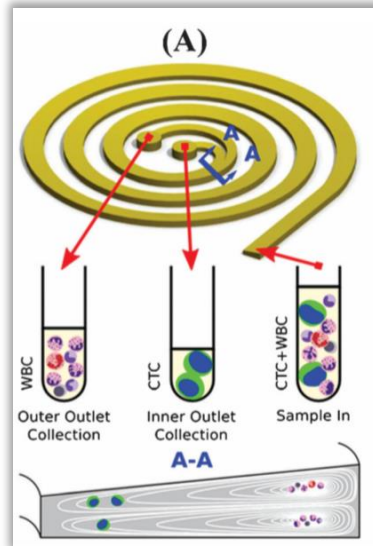


Figure 2: Spiral microchannel with trapezoidal cross-section [5]

The current interest in the Dean flow phenomenon is reflected in the active collaboration between our research group and the American research group at the Massachusetts Institute of Technology (MIT). This collaboration reflects the current fascination with exploring and understanding the Dean effect, with the aim of advancing knowledge and potentially opening up new avenues for practical applications in the separation of blood components.

1.2 Objectives of this thesis

The primary objective of our research was to explore, develop, validate and apply different models of cell clusters, particularly in the context of microfluidics. There are many approaches to studying the behaviour of cell clusters in microfluidic environments, and for our simulations we used the ESPResSo environment with the PyOIF module, which allows us to run simulations based on specified input parameters.

The simulation process was complex and involved creating a representative model of the microfluidic device. This included the insertion of fluid to mimic realistic movement and the inclusion of objects representing cell clusters. For our model of a uniform cancer cell, we chose a generalised spherical shape. Morse or Lennard-Jones attraction-repulsion interactions were then used to facilitate the combination of these cells into different cluster geometries, with two-cluster, three-cluster and four-cluster configurations chosen to match typical cluster structures found in the human body.

Given the scarcity of publications on the properties of cancer cells and clusters, periodic calibration of the parameters of our cell cluster model was essential to ensure that the computational model accurately represented reality. Our research was organised into three overarching and thematically distinct units:

- ***Analysis of Cluster Passage Through a Constricted Capillary***
 - Investigating the behaviour of cell clusters as they navigate through narrow capillaries.
- ***Measurement of Contact Area Size Under Shear Flow***
 - Assessment of the size of the contact area between the cell cluster and the wall in straight channels and simple bifurcations under shear flow conditions.
- ***Analysis of Cell and Cell Cluster Separation in a Curved S-Shaped Channel***
 - Examining the phenomenon of cell and cell cluster separation within a curved S-shaped channel.

These thematic units provided a structured framework for our investigation, allowing us to systematically address key aspects of cell cluster dynamics in microfluidic environments.

To define the goals of exploring, creating, validating and applying different models of cell clusters in microfluidics, we established specific subtasks that contributed to the overall success of our research. These subtasks were instrumental in guiding our progress and addressing key aspects of our investigation. The general subtasks included:

1. Microfluidic Device Modelling:
 - Create a suitable microfluidic device model that accurately represents the physical environment for our simulations.
 - Related sections: 2.4.1, 3.1.2, 3.2.2, 4.2, 4.3, 5.4.1, 5.6.1, 5.8.1
 - Ensure the model allows for the proper insertion of fluid, mimicking realistic movement, and the integration of objects representing cell clusters.
 - Related sections: 2.4.2, 3.2.2, 5.4.2, 5.6.2, 5.8.2
2. Cell Cluster Model Development:
 - Choose a representative model for a uniform cancer cell, such as a generalized sphere.
 - Related sections: 2.5.2, 2.5.3, 3.1.1, 3.2.1, 4.2, 4.3, 5.2
 - Implement Morse or Lennard-Jones attraction-repulsion interactions to combine individual cells into various cluster geometries.
 - Related sections: 2.4.5, 2.5.3, 2.6.2, 3.1.1, 3.2.1, 5.2

- Calibrate the cell cluster model to ensure its accuracy and reliability in simulating real-world scenarios.
 - Related sections: 2.5.3, 3.1.1, 3.2.1, 5.2
- 3. Simulation Execution:
 - Utilize the ESPResSo environment with the PyOIF module to run simulations based on the established input parameters.
 - Related sections: 2.4.1, 2.4.2, 2.4.3, 2.4.4, 2.4.5
 - Conduct simulations for different channel geometries and under various conditions to comprehensively explore cell cluster behaviour in microfluidics.
 - Related sections: 3.2.2, 4.2, 4.3, 5.4, 5.6
- 4. Thematic Investigation Units:
 - Organize the research into distinct thematic units focusing on specific aspects, such as the passage of clusters through constricted capillaries, measurement of contact area size under shear flow, and analysis of cell separation in curved channels.
 - Related sections: 3, 4, 5
 - Systematically address each thematic unit to gain a comprehensive understanding of cell cluster dynamics in different microfluidic scenarios.
 - Related sections: 3.1.2, 3.1.3, 3.2.4, 3.2.5, 4.4, 4.5, 5.5, 5.7, 5.9, 5.10

These subtasks collectively contributed to the successful achievement of our research objectives and provided a structured approach to exploring and understanding the behaviour of cell clusters in microfluidic environments. Each subtask contains a number of sections that apply to it.

1.3 Dissertation thesis outline

Chapter 1 serves as an introductory part of the thesis and provides an overview of our main research focus. In **Chapter 2**, we present the current state of knowledge derived from experimental studies, with particular emphasis on the behaviour of cell clustering in microfluidics and numerical simulations.

Chapter 3 is logically divided into two parts. In the first part, we will discuss an experiment investigating the dynamics of cell clusters in shear flow, especially in the vicinity of the walls. This section will include a comprehensive review of different cluster models and the channel model through which these clusters will pass. The influence of the initial rotation of the cluster on the simulation results will be investigated. We will then

define the adhesion force and consider the shear rate in relation to the elasticity of the cells within the cluster. In the second part of **Chapter 3**, an additional obstacle is introduced in the centre of the channel, transforming it from a straight channel to a simple bifurcation. The magnitude of the influence of all parameters on the simulation results is analysed and compared.

Chapter 4 focuses on the passage of a cluster of cells through a constricted capillary. Starting with a single cancer cell, we will explore the possibility of filling it with internal particles to detect the viscosity contrast between the inner part of the cell and the surrounding fluid. This is based on the hypothesis that the cell, which undergoes significant deformation throughout its passage through the narrowed capillary, may be better able to maintain its shape in this scenario. The width of the channel, the size of the cell and the velocity of the fluid will be key factors in the investigation. Finally, we present the simulation results and the refined cluster model that has been developed.

Chapter 5 is the largest of the preceding chapters. It focuses on Dean inertial flows and explores their utility in separating different cells and clusters within twisted channels. The parameters of investigation will include appropriate channel geometry sizes, cluster shapes and sizes, elasticity and fluid velocity, mirroring the initial setup of biological experiments. The results will be presented in the form of intricate plots, providing a nuanced understanding of the potential combinations between cells, clusters and their properties, particularly in relation to their mutual separation at the end of channels with three or more outlets. This section will also outline the collaboration with the MIT research group and discuss specific objectives for the coming months. As our environmental setup, cell cluster model and microfluidic device converge, a trade-off emerges that requires precision and time in its creation. Both technological and computational constraints affect the development of these components.

The final **chapter 6** will serve as a comprehensive summary, encapsulating the overall contribution of the thesis to the research in the analysis, development and application of the cancer cell cluster model. Future steps and experimental areas worth exploring with the computational model will be highlighted. This part will conclude with an enumeration of published and submitted papers during the PhD.

2 STATE OF THE ART

2.1 Shear flow and narrow capillaries

In the context of metastatic cancer, a 10 mL blood sample taken from a patient's peripheral circulation is expected to contain approximately 100 individual circulating tumour cells (CTCs) and up to 5 CTC clusters. These cells coexist with approximately 50 billion red blood cells, 80 million white blood cells and 3 billion platelets [3]. Estimates, which depend on the type of cancer and stage of treatment, are subject to variation due to the isolation and enumeration methods used, contributing to the wide range observed.

While CTC clusters are less commonly observed than their individual counterparts, their metastatic potential is noteworthy, being up to 50 times more metastatic than individual CTCs [6]. Understanding the dynamics of CTC clusters, particularly their ability to navigate through narrow capillaries [3] and initiate metastases, is crucial. Protection of cancerous cells within clusters from circulating shear stress has been suggested as a possible mechanism.

Shear stress is known to be detrimental to CTCs, as shown in a study investigating its effect on various cancer cells, including breast, ovarian, lung and leukemic cells [7]. Elevated shear stress, such as that experienced during intense exercise, can rapidly eliminate a significant number of CTCs, and prolonged exposure reduces the viability of highly metastatic and drug-resistant breast cancer cells.

For CTC clusters to initiate metastasis, extravasation, involving sustained contact with blood vessel walls at low velocities, is required. This study introduces two different cluster models - one with fixed geometry and another capable of cell rearrangement. Factors such as elasticity, morphological differences (spherical vs. less spherical) and shear rates are considered in the evaluation of contact time and areas of CTC clusters in flow.

Computational analysis using these models explores the dynamics under different shear rates. Existing results suggest that larger clusters or micro embolisms with intermediate non-sphericity exhibit increased adhesion potential, albeit at high shear rates $150\text{-}1600\text{s}^{-1}$, using rigid models with fixed geometry where individual cells lack deformability or ability to slide, affecting cluster conformation [2].

2.2 Bifurcations

In the intricate microvascular networks of the human body, gas exchange and nutrient delivery occur through a series of successive bifurcations in the main branches. Following these bifurcations, the flow enters narrow capillaries, which promote numerous cell wall contacts essential for facilitating exchange processes. While this vascular architecture is conducive to the functioning of healthy cells and normal physiological activities, it poses a challenge to CTCs.

Tumour-derived CTCs are transported through the bloodstream, potentially leading to metastases if they escape damage or destruction in the circulation. Research has shown that clusters of CTCs have a higher metastatic potential than individual CTCs, with the outer cluster cells forming a protective barrier for the inner cells [8]. The isolation of viable CTC clusters from large volumes of whole blood remains a challenging task, and the use of microfluidic devices to concentrate these clusters in blood represents a first step in experimental investigations [9].

The metastatic potential of CTC clusters is influenced by several factors, some of which are not fully understood. One critical factor is the extent of cell-wall contact that the cells have [4]. In addition, the formation of tethers between tumour cells and endothelial selectins plays a role in initiating cell rolling, a process that can lead to firm adhesion [10] and extravasation [2].

The cluster-wall contact in bifurcations is of particular interest, as studies have shown a correlation between hydrodynamic forces arising from the vessel topology and the properties of CTCs in the attachment regions, as demonstrated by the transport of CTCs in idealised bifurcated vessels [11]. This complexity is further increased in the presence of blood cells. Although the time-averaged partitioning at a bifurcation can appear as either classical or inverse partitioning, the time-dependent behaviour can switch cyclically between these two types, affecting the behaviour of CTC clusters [12].

2.3 Dean flow

Under certain micro-flow conditions, the dominance of fluid inertia over viscous forces allows precise control and manipulation of suspended particles, leading to the development of techniques for sorting and separating particles based on size, shape and deformability [13], [14], [15], [16], [5]. Meandering channels, which induce complex flow

patterns and particle behaviour due to inertial effects, have been the subject of experimental studies [17], [18], [19].

The work by Buganova et al. [20] deals with the inertial migration of solid particles in curved channels of rectangular shape. In particular, larger particles concentrate and stabilise in the centre of the channel, leaving space for smaller particles along the edges, allowing successful separation. The study explores the intriguing possibility of triple separation, demonstrating the potential of inertial effects in particle manipulation.

Microfluidics, with its breakthroughs and advances, offers opportunities to exploit inertial effects in biomedicine. In living organisms, inertial flows, such as those at vascular bifurcations, provide insights into the movement of cells. This could be used to capture rare cells from blood [21] or separate diseased red blood cells from healthy ones [22].

This study extends the exploration of inertial microfluidics by introducing rounded edges in channel geometries to mimic the curvature of blood vessels. Larger geometries are used compared to previous work to account for the size of cells and cell clusters. The model incorporates cell deformability, a property that has not been extensively addressed in previous research [20].

2.4 ESPResSo and PyOIF

ESPResSo, an open-source software described in the [23], enables the continuous simulation of the flow of elastic objects in a fluid. ESPResSo is widely used in physics, chemistry, and molecular biology, and features advanced simulation algorithms that focus primarily on molecular dynamics. It effectively extends its capabilities to the simulation of microscopic elastic objects.

In addition to contributing to the development of ESPResSo, the Cif-BMCG research group is actively involved in the implementation of the PyOIF (Python Object-in-fluid) software package. Designed specifically for ESPResSo, PyOIF excels in simulating the flow of elastic objects, particularly in scenarios such as blood cell suspensions. This module, based on a two-component model of fluid and immersed objects, is programmed in C++ and uses a Python scripting interface for simulation execution, data management and rendering.

PyOIF integrates a cell flow model with three core components: a fluid model, models of various elastic objects, and various interaction types. The focus is on the elastic objects and their interactions within the environment, a central aspect of the model used.

There is also a nuanced focus on the fluid model, as fluid flow with immersed particles is the primary focus of our research efforts.

2.4.1 Simulation box

When starting any simulation, the first step is to create a simulation box, which requires the definition of boundaries. This crucial step is achieved using geometric shapes, mainly rhomboids and cylinders, within ESPResSo. Although there are other types of boundaries, these shapes are the main focus. Although the ability to define obstacles is available, it is not a central objective of our current work.

Our simulations operate with a time step of $0.1\mu\text{s}$, signifying that each step in the simulation corresponds to a time interval of $0.1\mu\text{s}$. This temporal granularity provides a framework for the dynamic evolution of the simulated scenarios.

2.4.2 Fluid properties

The fluid is undoubtedly the largest moving part in the model and is an integral part of it. As it is a laminar flow, the fluid is calculated using the Lattice Boltzmann (LB) D3Q19 method, which uses a static cubic lattice. Each non-boundary grid point contains 19 populations of fictitious particles that propagate and collide with particles from neighbouring grid points. Macroscopic fluid properties such as velocity and density are then obtained from these populations. More details on the LB method can be found at [24]. The cell is coupled to the fluid using the bidirectional dissipative immersed boundary method [25]. At each time step, the elastic forces, fluid forces, cell-cell interaction forces and cell-wall interaction forces at each node of the cell membrane are summed and used to propagate the node using Newton's second law of motion. In the ESPResSo software we define three different fluid properties:

- I. *Direction* - there are two ways to define fluid motion:
 - External force density:
 - One approach is to assign an external force to each discretisation point within the fluid mesh. This external force is parameterised by the external force density, allowing precise control of its influence on the fluid dynamics.

- Moving boundary:
 - The second method involves implementing constant Dirichlet boundary conditions at a given boundary, imparting a constant velocity to the fluid and thereby inducing a gradual motion. This boundary, which serves either as a wall element or as an obstacle, is characterised by predefined constant values at its boundary points. In our simulations, a rhomboid wall is used as the boundary, facilitating the controlled movement of the fluid.
- II. *Velocity* – affects the speed at which blood cells flow. It allows us to get closer to the biological or experimental conditions we need to study. The faster the velocity, the faster the cells are sorted.
- III. *Periodicity* – We only model the slice with periodic terms, so it can be thought of as a moving window in a much larger geometry. Therefore, we do not need to use more computing power for even larger geometries. The model uses periodic boundary conditions which must be considered when creating the geometry. It is necessary to ensure that opposing boundaries have the same velocity profile. Where the velocity is zero, there is a wall at either end. We have provided periodicity by using stacks. For ease of visualisation, objects are always shown in the same basic geometry, i.e. an object leaving it on the right will re-enter it on the left. The advantage of this is that we can see all the moving objects and the fluid behaviour at once on one periodic part.

In our experimental investigations, we have chosen to use the 'moving boundary' method to study fluid dynamics because of its universal applicability. This approach can be adapted to both linear and meandering channel configurations. Initially, a simple syringe mechanism is used to ensure a consistent fluid velocity throughout the model.

However, the introduction of an external force density results in a unidirectional fluid drive throughout the mesh. This representation does not accurately mimic the complex flow patterns observed in serpentine channels.

2.4.3 Bonded interactions

The elastic object model is primarily intended for modelling red blood cells but can also accommodate objects of different shapes. In this model, the membrane of the object is represented by triangulation of its surface, Figure 3. To model the elastic properties of the membrane we use 'bonded' interactions, i.e. they are predefined between pairs or tuples

of membrane points. The elastic properties of the object are governed by five elastic modules, each of which exerts a defined force on the vertices of the mesh. The magnitude of the force depends on the corresponding elastic coefficient for the given module and the positional change of the vertex.

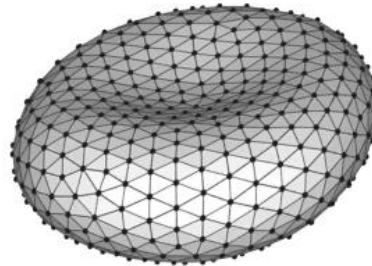


Figure 3: Example of triangulation on a red blood cell

The **modulus of elasticity** (k_s) characterizes the stiffness of the object, exerting an opposing force when part of the membrane undergoes stretching. Conceptually, the edges of the triangulation can be likened to springs trying to maintain their rest length.

The **bending modulus** (k_b) contributes to preserving the object's shape. It operates by ensuring the maintenance of angles between adjacent triangles, thereby sustaining the object in its relaxed state.

The **local area preservation module** (k_{al}) is designed to uphold the area of individual triangles within the triangulation, employing mechanisms akin to the elasticity module.

The **module for preserving the total area** (k_{ag}) contributes to the global properties of the object. Unlike the previous modules that embody measurable mechanisms, this module focuses on maintaining the overall surface of the object.

The **volume conservation module** (k_v) ensures the object maintains a constant volume. Unlike specific biophysical mechanisms observable in other modules, this global module is not tied to a particular mechanism but serves to maintain the object's volume, which generally remains constant in typical circumstances.

The initial geometry of each elastic object is defined in two sets: 'nodes', which contain the coordinates of the grid points, and 'triangles', which provide the triangular incidence. For the research, biconvex disc shapes were first used to represent red blood cells due to their elastic and easily deformable nature. The next step was to use simple spheres to represent circulating tumour cells, as this is the most common shape. In general, these objects are less elastic and more difficult to deform.

2.4.4 Non-bonded interactions

The ability of objects to deform and interact with the fluid is due to the discretisation of their surface using a triangular mesh. This interaction is facilitated by the use of nested objects. The study of interactions, both between different object models and between objects and the fluid, is critical to the research objectives. In addition, interactions with other entities present in the simulations, including the channel walls and various obstacles within the channel, are considered. The comprehensive study of these interactions is essential to gain insight into the dynamic behaviour of the simulated systems.

Individual cell points can also use 'non-bonded' interactions. For example, a cell can interact with itself or with its internal particles. Each particle has its own unique ID and belongs to a type. These interactions are defined not only by type but also by distance. This allows us, for example, to define the strength of adhesion between two cells in a cluster. Non-bonded interactions, unlike bonded interactions, are not fixed at the start of the simulation. They are activated and deactivated depending on the particle distance. They may be active for a while (when the particles are close together) and then deactivated (when the particles move apart). In our work, the following interactions stood out, as shown in Figure 4:

- a. Interactions between cell membranes in a cluster
- b. Cell membrane - wall
- c. Inner particle of cell - cell membrane
- d. Inner particle of cell - inner particle of cell
- e. Cell membrane - cell membrane (same cell)

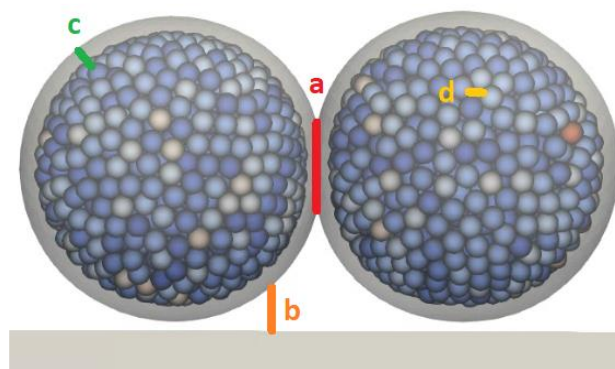


Figure 4: Schematic illustration with interactions highlighted

Option (e), not shown in the Figure 4, is a special interaction between points of the same cell membrane that facilitates bonded interactions to avoid excessive deformation of the cell. There are three main types of object-object interactions:

Object-object interaction (a)

Given the presence of two or more objects, we establish interactions between these objects, allowing them to be aware of each other. In our simulations, a consistent setup involves the use of 28 spheres or clusters. This number was chosen randomly due to the computational power of the simulations. As more cells are used, the computational effort increases either linearly or exponentially, depending on the number of different interactions used. When these objects are introduced into the channel, they form a group. This configuration is designed to meet the specific needs of our simulations, allowing the study of interactions and dynamics within the context of these multiple objects.

The interactions between the objects are point-wise. For example, each particle of type 0 (representing all mesh points of object 0) engages in a repulsive membrane collision interaction with each particle of type 1 (comprising all mesh points of object 1) as soon as the pair comes within a distance less than the membrane section, as described in [26]. This interaction ensures that the meshes of the two objects overlap during collisions but repel each other, preventing any fusion.

Notably, we did not initially set up any interactions between the two objects, as they are spaced apart along both the x-axis and the y-axis. There is no need to establish these interactions because the objects are deliberately positioned far apart at the start of the simulation. For more details on these models and their implementation in the ESPResSo software, see [26].

Object-boundary interaction (b)

The implementation of interactions extends to contact between objects and the walls of the simulation channel, as well as interactions with other solid obstacles within the channel. These interactions are also point-based. For example, any particle of type 0 (representing all mesh object points) will experience a repulsive soft sphere interaction with all boundaries of type 10 (encompassing all boundaries) as soon as their distance becomes less than the soft cut distance. The parameters `soft-a` and `soft-n` control the strength of this interaction, while `soft-offset`, a distance offset, remains zero for our specific purposes [27].

This repulsive force only comes into play when the distance between the points on the surface of the object and the obstacle is less than the specified threshold, a parameter that is integral to the configuration of the interaction forces between the nested object and the obstacle.

Interaction of the object surface with itself (e)

The interaction between different parts of the object's surface becomes critical when the object is bent and these parts come into contact. In such cases, it is essential to prevent the object from folding back on itself. This is achieved by implementing self-interaction for the surface of the object. Remarkably, this self-interaction is implemented in a manner analogous to the interaction between the object and other objects, ensuring a consistent approach across different interaction scenarios.

2.4.5 Attraction-repulsion interactions

Morse and Lennard-Jones interaction

We use Morse and Lennard-Jones (LJ) potentials to describe the interactions between cell membranes in a cluster. Both the Morse potential and the LJ attract and repel cells over a defined distance. The difference between them is that LJ has been more studied on our side, because our colleague Alžbeta Bohiniková spent a long time on it in her article [28], where she explains the different dependencies in more detail. Specifically, using LJ, we define the adhesion between cells in a cluster as follows in

Equation 1.

Equation 1: Defining cell-cell adhesion using the LJ potential

$$V_{LJ}(r) = \begin{cases} 4\epsilon \left[\left(\frac{\sigma}{r}\right)^{12} - \left(\frac{\sigma}{r}\right)^6 \right] & \text{if } r < r_{cut} \\ 0 & \text{else} \end{cases}$$

In equation, the parameter r represents the distance between two interacting particles. r_{cut} is the cutoff distance from which the cells can register with each other, and ϵ expresses the strength of the interaction by which the cells should attract or repel each other. The parameter σ determines the distance r_{min} where repulsion turns into attraction. This change occurs at the local minimum of the potential, so $r = r_{min} = \sqrt{2}\sigma$. Parameter r represents the distance between two particles that interact. r_{cut} is the threshold distance

from which the cells can register with each other, and ϵ expresses the strength of the interaction by which the cells should attract or repel each other.

Hard-Asphere-Tree interaction

The HAT (Hard-Asphere-Tree) potential is used to model interactions between particles with hard core repulsion and soft-shell attraction. It's particularly useful for modelling complex fluids where the particles have non-spherical shapes. The HAT potential is typically defined by two parameters: the hard-core diameter and the soft core diameter. The potential energy U_{ij} between two particles i and j is typically given by:

Equation 2: HAT potential

$$U_{ij} = \begin{cases} \infty & \text{if } r < r_{\text{core}} \\ 4\epsilon \left(\left(\frac{\sigma_{\text{soft}}}{r} \right)^{12} - \left(\frac{\sigma_{\text{soft}}}{r} \right)^6 \right) & \text{if } r_{\text{core}} \leq r \leq r_{\text{soft}} \\ 0 & \text{if } r > r_{\text{soft}} \end{cases}$$

Where:

- r is the distance between particles.
- r_{core} is the hard-core diameter.
- r_{soft} is the soft-core diameter.
- ϵ is the energy scale.
- σ_{soft} is the soft-core diameter.

Dissipative Particle Dynamics interaction

In DPD (Dissipative Particle Dynamics), the forces acting on a particle are divided into three components: conservative, dissipative and random. The DPD potential is often expressed in terms of these components:

1. **Conservative Force:** It acts to keep particles together and is typically given by a truncated and shifted Lennard-Jones potential:

Equation 3: DPD – Conservative Force

$$F_{ij}^C = \begin{cases} A(1 - r_{ij}/r_c) & \text{if } r_{ij} < r_c \\ 0 & \text{otherwise} \end{cases}$$

Where:

- r_{ij} is the distance between particles i and j .
- A is a parameter determining the strength of the interaction.
- r_c is the cutoff distance.

2. **Dissipative Force:** It removes kinetic energy from the system, mimicking viscosity:

Equation 4: DPD – Dissipative Force

$$F_{ij}^D = -\gamma w(r_{ij})(\mathbf{v}_{ij} \cdot \hat{\mathbf{r}}_{ij})\hat{\mathbf{r}}_{ij}$$

Where:

- γ is the dissipative coefficient.
- $w(r_{ij})$ is a weight function that typically decreases smoothly with r_{ij} .
- \mathbf{v}_{ij} is the relative velocity of particles i and j .
- $\hat{\mathbf{r}}_{ij}$ is the unit vector pointing from particle i to particle j .

3. **Random Force:** It introduces stochastic fluctuations:

Equation 5: DPD – Random Force

$$F_{ij}^R = \sigma \eta_{ij}$$

Where:

- σ is the magnitude of the random force.
- η_{ij} is a random number drawn from a Gaussian distribution.

In our research, these potentials are implemented to simulate microfluidic systems. Users can define the parameters of these potentials, such as the interaction strengths and characteristic lengths, to accurately model the behaviour of the particles in the microfluidic environment. This allows researchers to study phenomena such as fluid flow, particle transport, and mixing in microfluidic devices.

2.5 Cell and cluster models

2.5.1 Red blood cell

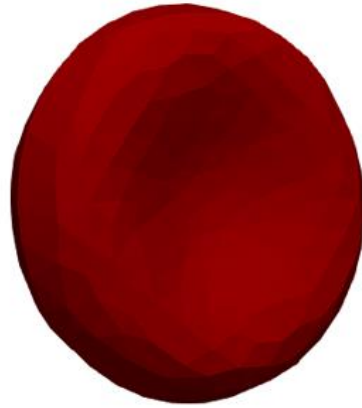


Figure 5: Red blood cell model

The red blood cell model in Figure 5 formed the initial basis of our research. On average, a red blood cell has a radius of $3.91\mu m$ with a volume of $90\mu m^3$ and a surface area of $128\mu m^2$. The red blood cell has a biconcave shape. The membrane of the cell is made up of a network of triangles. We have applied this triangular network to other cell models. The calibration of the red blood cell was based on the elasticity data in [29].

2.5.2 Circulating tumour cell



Figure 6: Circulating tumour cell model

As there are many different types of cancer cells, we chose the following spherical cell model, as shown in Figure 6, which represented the basic cancer cell model for us. Unlike the red blood cell model, where quantitative comparisons could be made with published data, the elasticity of the cancer cell model had to be calibrated indirectly using qualitative

comparisons. We did not have detailed information on the elastic properties, i.e. we calibrated the model to approximate its behaviour to previous biological experiments [30].

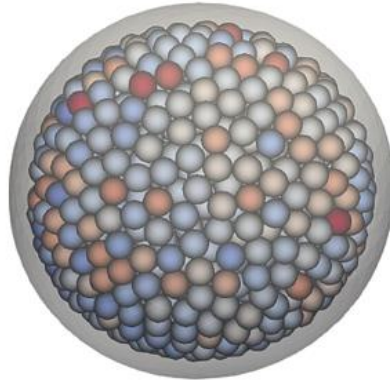


Figure 7: Circulating tumour cell model with inner particles

The intrinsic viscosity of a biological red blood cell is approximately five times greater than that of blood plasma. Therefore, we use dissipative particles to provide proper viscosity contrast in both red blood cell and cancer cell models. Figure 7 shows a white cancer cell with internal particles with a particle radius of $0.5\mu\text{m}$. The effective viscosity of the internal particle suspension achieved by DPD interactions according to [31] is 4.5mPas , with an external fluid viscosity of 1.55mPas and a density of 1000kg/m^3 . The particles try to find a suitable location in the cell and repel each other until they pass just beyond the cutoff. If they fail to get beyond this limit, they "fog up".

This is the non-bonded interaction mentioned in Section 2.4.4. As each particle behaves in this way and is constantly moving around the cell, we see that each particle is affected by the interaction with a different force. A particle is affected by several other particles, and the direction in which the other particles affect a given particle is also important. A particle may be subject to large interactions, but it may not even move because the resultant of the interacting forces is zero. Small interactions acting in roughly the same direction will be sufficient to cause the particle to move. The colour of the particle depends on its velocity, which is determined by the resultant of the forces acting on it.

2.5.3 Circulating tumour cell cluster

The individual cells were then combined to form a cell cluster. We added more complex intercellular interactions to the model shown in Figure 8, which defined the strength of adhesion between cells. By adding this interaction, the cells began to deform to some extent according to the strength of their adhesion. We do not neglect the stiffness of the

cells in this interaction. The higher the stiffness of the cell, the less visible the deformation of the cell in the contact area and thus the lower the adhesion force. We discuss the difference between soft and stiff cells and their influence on the behaviour of the cluster in flow in [32], where the given comparison is made based on a simple bifurcation.



Figure 8: Basic cancer cell cluster model



Figure 9: Transparent model of a cancer cell cluster with inner particles [33]

In Figure 9 we see a cluster model with internal particles. Our model allows the properties of the internal particles to be set separately for each cell. This means, for example, that it is possible to create a cluster of cells, each with a different intrinsic viscosity.

2.6 Method of joining cells into a cluster

Metastases are secondary tumour deposits formed by cells that have become detached from the primary tumour and have spread to other tissues where they continue to grow. Cancer cells travel through the bloodstream as single cells or clusters of cells called circulating tumour micro emboli (CTMs) [2]. Clusters have better resistance and may have up to 100 times greater metastatic potential [34] than solitary cells. CTMs are also

associated with poorer patient outcomes. The movement of clusters in the flow depends, among other things, on their size and shape. To investigate the frequency and strength of contact with vessel walls, models of the Colo205 colorectal cancer cell line aggregates consisting of two, three and four cells in simple geometric conformations were created.

2.6.1 A well-known method of creating a cluster model

In [2], the triangulation of the cell surface in the model was created using MATLAB software. This divided the cell model into a spherical square mesh consisting of 96 elements. First, a cube-shaped geometry was created, each surface of which was later divided into 16 quadrilateral elements. The cube was then projected onto the surface of a sphere placed at the centre of the cube, Figure 10.

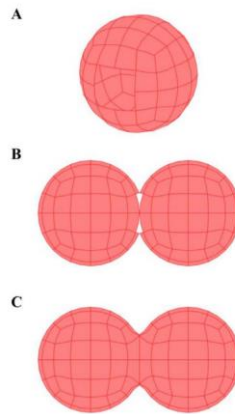


Figure 10: Creating a cluster of cells according to Andersen [2]

To create a connected pair, also called a 'doublet', the algorithm removed elements from one side of the sphere (A) and created a copy of the cell. It then rotated the duplicated cell so that the removed walls were side by side (B). Next, the points of the cells at the removed locations were joined to form a common mesh (C).

Next, triplets and quadruplets of cells, also known as 'triplet' and '4-mer aggregates', were joined in the same way, as shown in Figure 11.

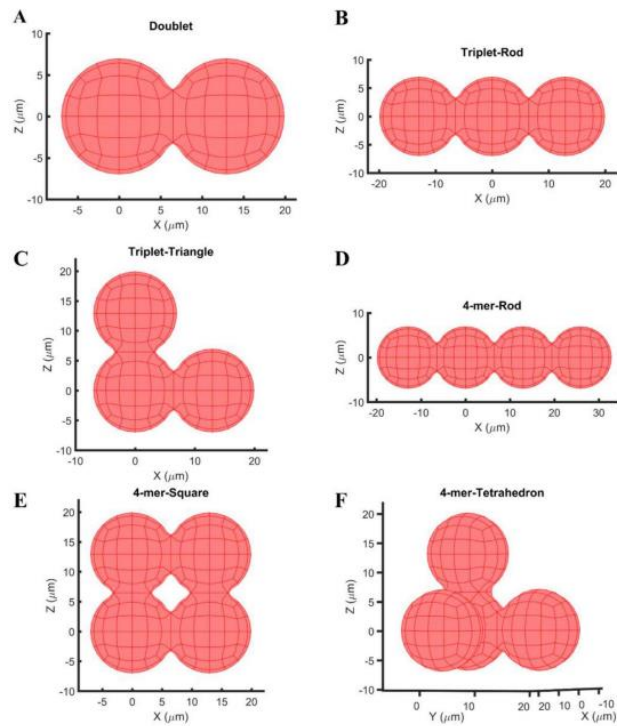


Figure 11: Different geometric shapes formed by a cluster of cells [2]

Pairs of cells (A) in a cluster are among the simpler and less implementation intensive. Larger and more complex clusters consist of inner and outer cells. The latter are more dangerous because the outer cells can protect the inner cells to some extent. More complex clusters are also more likely to form metastases. To better understand the behaviour of clusters, we start with simpler clusters where there are fewer cells (B-F).

2.6.2 Method of creating our cluster model

We performed the first method of coupling the cells in Figure 13(a) using the LJ potential. So, the cells were attracted at some distance, but repelled when they were very close together. The advantage of this type of coupling is that the cells can slide over each other in a cluster and reorganise themselves, changing the geometry of the model. Coupling procedure for any two cells with a common adhesion surface, Figure 12:

- I. *Identification* of the centre point of the contact area on both adjacent grids (the centre of contact is the midpoint between the centres of the two cells; the centre point on each surface is then defined as the grid point closest to the centre of contact).
- II. *Identification* of contact points (domes) on both adjacent grids (the threshold distance from the centre is determined from the desired radius of contact).

- III. *Defining* the adhesion plane for each cell with the normal vector determined by the centres of the two cells.
- IV. *Projection* of the points on the domes onto the adhesion plane.
- V. *Adjusting* the positions of the cells so that the adhesion planes are at a distance r_{min} , which marks such a point from the LJ potential, when attraction changes to repulsion.

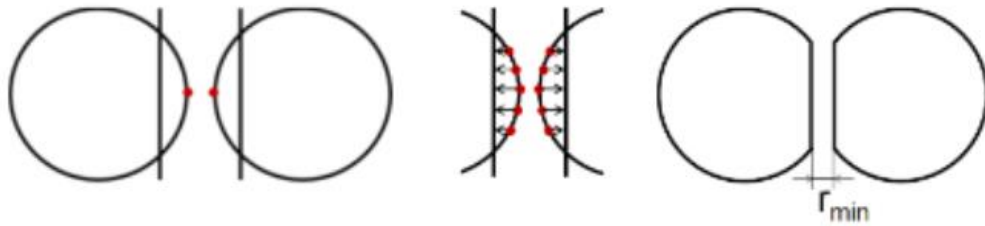


Figure 12: 2D illustration of the process for creating a flat adhesion surface

The algorithm can be repeated if we would like to add additional cells for more complex clusters connected by the LJ potential.

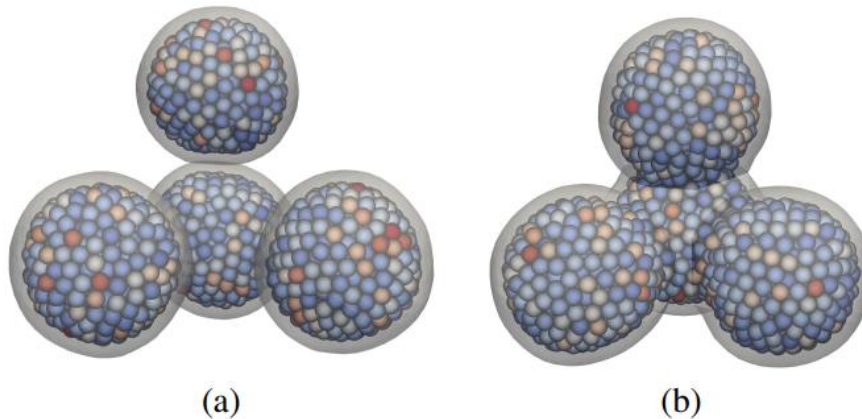


Figure 13: a) LJ potential coupling b) Unified network model [32]

According to [35], there exist clusters with so much adhesion that there are no fundamental changes in the cluster reorganization during the flow. Therefore, we modelled the cluster using the predefined geometry shown in Figure 13(b), where no additional cell joining is performed. Thus, cells are not able to reorganise and slide over each other. This uniform network model is only valid for clusters that do not change their morphology significantly over time. The advantage is that no additional calibration of adhesion properties is required. Figure 13 illustrates a type of cluster with four cells, hereafter referred to as "L4". Algorithm for creating a unified network for the entire cluster, Figure 14:

- I. Identification of the radius of the contact area.
- II. Calculation of the height of the spherical canopy of adjacent cells that we will want to remove.
- III. Identification of all grid points in the canopy.
- IV. Removing the grid points and triangles that the canopy contains.
- V. Identification of boundary rings on both adjacent grids.
- VI. Connecting corresponding points on the boundary rings.
- VII. Renumbering the triangles so that the new network is consistent.

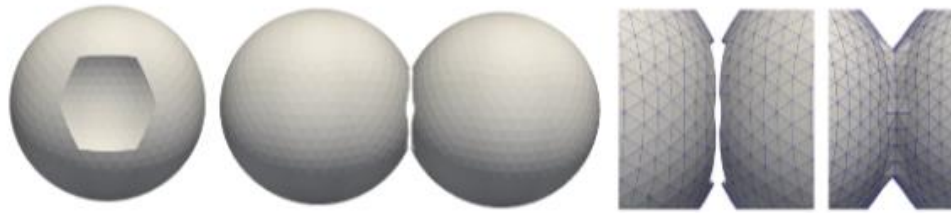


Figure 14: The process of joining two cells into a cluster with a unified network [33]

The algorithm can also be repeated if we would like to add additional cells for more complex clusters with a uniform network.

2.7 Hardware and supporting software

A computer server - Snorlax served as the primary computing device for running, processing and analysing the simulations. This allowed us to run multiple batches of simulations simultaneously or run extended simulations overnight, taking advantage of the machine's higher core count.

For visualizing the simulation results, we employed the software Paraview [36]. Most of the images presented in this work were created using Paraview, which directly processed the generated VTK files [37].

ESPResSo and PyOIF

In this work, we utilized the latest version available on GitHub [23] for the ESPResSo software. For the computational module PyOIF, we employed version 2.1. The parameters for the individual machines are as follows:

Acer Nitro v5

- Personal notebook information:
 - Processor: Intel(R) Core(TM) i7-8650U CPU, 1.90 GHz, 2.11 GHz
 - System type: x64
 - RAM: 32 GB
 - SSD: 500 GB
 - HDD: 1 TB
 - GPU: NVIDIA GeForce GTX 1080 Ti
 - Number of cores: 6

Lenovo Legion

- School notebook information:
 - Processor: I AMD Ryzen 5 5600H with Radeon Graphics, 3.30 GHz
 - System type: x64
 - RAM: 16 GB
 - SSD: 500 GB
 - HDD: 500 TB
 - GPU: NVIDIA GeForce RTX 3060 Laptop GPU
 - Number of cores: 6

Computer server - Snorlax

- Computer financed by the Slovak Research and Development Agency project (project number APVV-15-0751), information:
 - Processors: AMD Threadripper 2950X - 16/32T-Core, 3.5 GHz (180W), Boost 4.4 GHz
 - SSD: 1 TB NVME
 - HDD: 8 TB
 - GPU: NVIDIA GeForce GTX 1080 Ti
 - Number of cores: 32

To provide a real-time comparison of the performance of each machine used during the simulations, a table has been compiled detailing the relative speed of each machine. The use of the Snorlax machine generally accelerated the experiments run on the Dell laptop, affecting the duration of both the shortest and longest simulations.

Table 1: Time comparison between machines

Machine [type]	Computational Time [days]	Average velocity [m/s]
Acer Nitro	9	0.18
Acer Nitro	4	0.6
Lenovo Legion	7	0.18
Lenovo Legion	3	0.6
Computer server - Snorlax	7	0.18
Computer server - Snorlax	3	0.6

For specific values of the inlet conditions and corresponding flow rates, please refer to Table 1. It's important to note that the values in the table are approximate. In particular, the simulations carried out on the laptop took almost twice as long as those carried out on the virtual machine, highlighting the efficiency gains achieved with the latter.

3 DYNAMICS AND OBSTACLES: EXPLORING CELL CLUSTER BEHAVIOR IN SIMPLE SHEAR FLOW AND IN BIFURCATED CHANNELS

3.1 Modelling cell clusters and their dynamics in near-wall shear flow

Shear stress is known to have an adverse effect on CTC. A paper [38] investigated the effects of shear stress on breast cancer cells with different metastatic capabilities, ovarian, lung and leukaemia cancer cells and found that shear stress of 60 dyne/cm^2 (achievable during intense exercise) kills a significant number of CTCs within a few hours, and prolonged shear stress effectively reduces the viability of highly metastatic and drug-resistant breast cancer cells.

In this work we develop two different cluster models, Model I and Model II, we also consider the effects of elasticity and compare more spherical and less spherical morphologies at different shear rates. To quantify the presence of near-wall cells, we measured the adhesion potential of near-wall rolling clusters by evaluating metrics involving contact time and contact area in the flow at different shear rates.

Recent investigations [2] suggest that larger clusters or micro embolisms with intermediate non-sphericity have greater adhesion potential. However, this has only been done at high shear rates ($150\text{-}1600\text{s}^{-1}$) and with stiff models with fixed geometry, i.e. individual cells could not deform or slide over each other, thus changing the conformation of the cluster. The contribution of our models is that it will also allow the study of gliding clusters with possibly different elasticities.

3.1.1 Cluster parameters and models

Using two methods of joining cells into clusters, we formed clusters of CTC cells based on the geometry observed under the microscope, Figure 15.

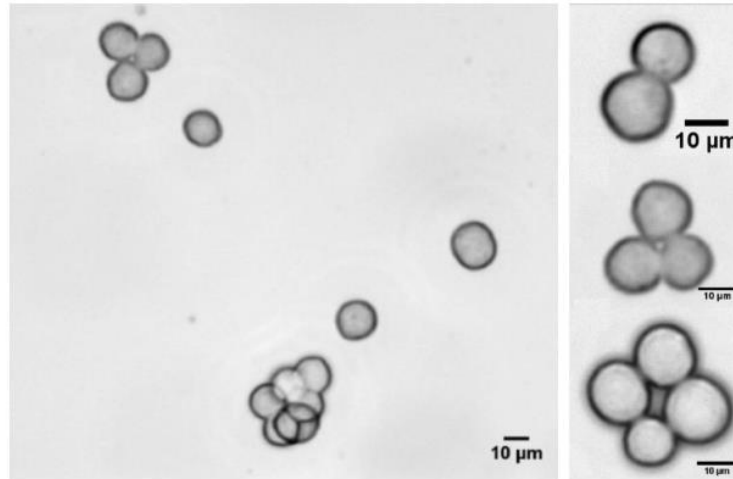


Figure 15: Optical microscopy images of Colo205 cells and their clusters [2]

With this observation, we considered using four different shapes of cell clusters: doublet (two cells), tri-cluster (three chain-shaped cells), L3-cluster (three L-shaped cells), and quad-cluster (four cells placed at the vertices of a regular tetrahedron) as we can see in Figure 16. Adhesion calibration was performed on two cells since the same principle can then be applied in multi-cell clusters.

Table 2: Cluster characteristics [33]

cluster type	Surface [μm^2]	volume [μm^3]
bi	1171	2851
tri	1730	4272
L3	1730	4272
tetra	2145	5676

In all geometries, we use cells with a radius of $7\mu m$ and an adhesion contact area with a radius of $2.7\mu m$ (for the four-cluster, the contact area is slightly smaller because the contact surfaces are close together). Both radii were determined from Figure 15 biological cells. The triangulation mesh of the cell membrane of one cell contains 1002 points on its surface.

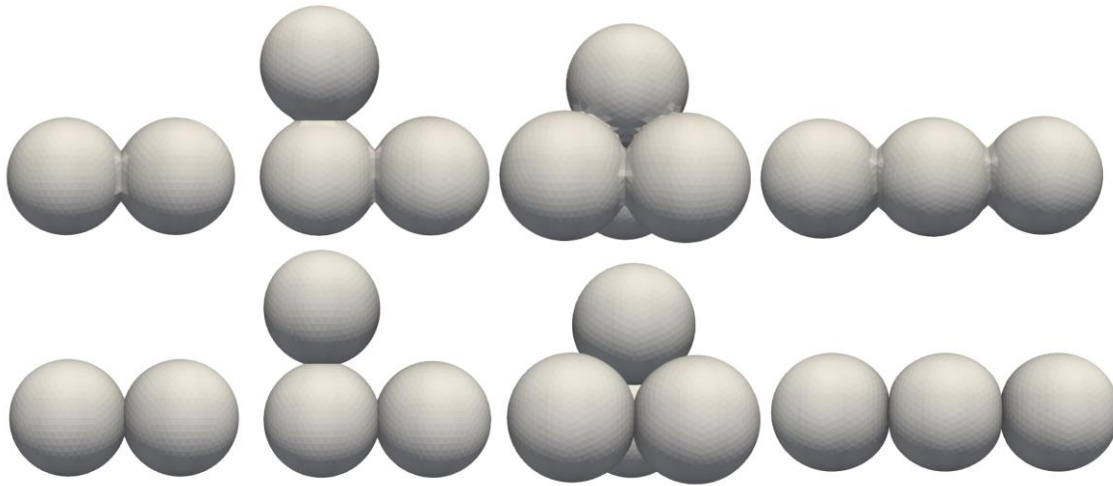


Figure 16: Cluster geometries bi, L3, tetra and tri as represented by the two models. Model I in the first row, Model II in the second row [33]

Model I is well suited to simulating robust adhesion, with mesh structures of individual cells merged into a unified cluster mesh. The cells remain connected throughout the simulation, and although the cluster can deform depending on the elastic properties of its membrane, it cannot change the relative positions of individual cells. In addition, both models allow for different cluster geometries, such as L4, a generalisation of L3, or complex clusters comprising more cells, although these configurations are not explored in this study.

Model II establishes connections between individual cells via a repulsive-attractive potential. Within this framework, cells have the ability to slide over each other or separate under significant stress, making this model suitable for clusters characterised by weak adhesion.

Model I: Clusters with strong adhesion

A simple cluster model, suitable for scenarios where cell-cell adhesion is strong and morphology remains constant, involves treating the cells as a single unified entity. This can be achieved by defining the shape of the cluster and then generating the corresponding triangulation mesh.

To generate the triangulation mesh for the entire cluster, we begin with multiple identical triangulations of a sphere, each with a radius r_s . Each triangulation comprises a list of node coordinates $[x, y, z]$ (with their IDs corresponding to their order in this list, starting at 0) and a list of triangles represented by triplets of integer node IDs. From these lists, nodes and triangles on the neighbouring caps are removed, and the neighbouring

meshes are merged (refer to Figure 3). The algorithm for merging two adjacent spheres involves the following steps (this process is repeated for clusters containing more cells):

- identify one point of contact on each sphere (not necessarily a mesh node)
- select the contact area radius r_c
- on both spheres remove caps, i.e. remove all mesh nodes closer to their respective points of contact than $\sqrt{r_c^2 + (r_s - \sqrt{r_s^2 - r_c^2})^2}$
- identify mesh nodes on the rings around the holes
- for each point on the ring, find the closest neighbour that belongs to the ring of the neighbouring mesh and replace this pair of nodes with one node which lies halfway between them
- change IDs of the nodes in triangles in the second mesh to reflect the fact that they were replaced by new nodes
- shift IDs of all triangles in the second mesh to remove the gaps in numbering left by removing the nodes
- join the nodes files and the triangles files



Figure 17: Joining process for creating a bi-cluster from two single cells [33]

Model II: Clusters with weak adhesion

Certain clusters of CTCs exhibit considerable flexibility in changing their morphology. Cell-cell adhesion within these clusters appears to possess a degree of adaptability such that, when dictated by the geometry of a microfluidic device, a cluster that is initially spherical can transform into a single chain of cells [39].

To simulate this dynamic behaviour, we have developed an approach that allows greater flexibility in the connection of cells compared to Model I. Instead of establishing fixed connections between adjacent mesh nodes, this method utilises non-bonded interactions. These interactions are similar to those used in our model to repel cells from

Dynamics and obstacles: Exploring cell cluster behavior in simple shear flow and in bifurcated channels

the channel wall or to prevent individual cells from overlapping in a flow environment. The mechanics of this interaction is based on a potential defined between two types of particles: particles belonging to one cell are classified as one type, while particles from the second cell are classified as another type. Depending on the specific potential used, the interaction can be repulsive, attractive or a combination of both.

Determination of strength adhesion

The strength of adhesion is determined by the size of the contact area and the parameters of the LJ potential between the two cells. We used the same adhesion force between each pair of cells in the cluster. To find out what the adhesion force between two cells is, we carried out two experiments. In both experiments, we tried to separate these cells by force. In the first experiment, we pulled away certain points of the membrane network using rings on opposite sides of the cells. This is a principle called micro pipetting, Figure 18.

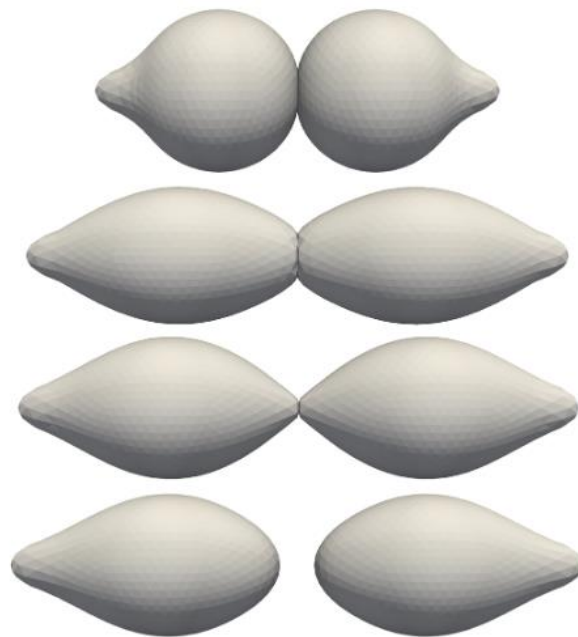


Figure 18: Cell separation based on the micropipette principle [33]

To assess the strength of a particular cell doublet, we performed two simulation experiments in which the doublet was separated by force. In the first experiment, as shown in Figure 18, a pulling force was applied to selected mesh points located on the outer copulas of the cells, simulating a micropipette. In addition, we verified the results by applying the tensile force to all membrane points. In this scenario, the cells separated at

nearly identical pulling forces, with only variations in shape transitions, as expected. In the second experiment, as shown in Figure 19, the cells were separated by flow.

Flow is induced by introducing inflow at two opposing sides of the microfluidic chamber, as depicted in Figure 19, with outflow established on two perpendicular sides. The cells are positioned in the centre of the chamber to ensure that the contact surface is perpendicular to the flow direction. This configuration allows the flow to act as the driving force for separation. By adjusting the boundary inflow velocity, we determine the velocities that facilitate separation and those that are not strong enough to do so. Further details of both experiments can be found in reference [28].

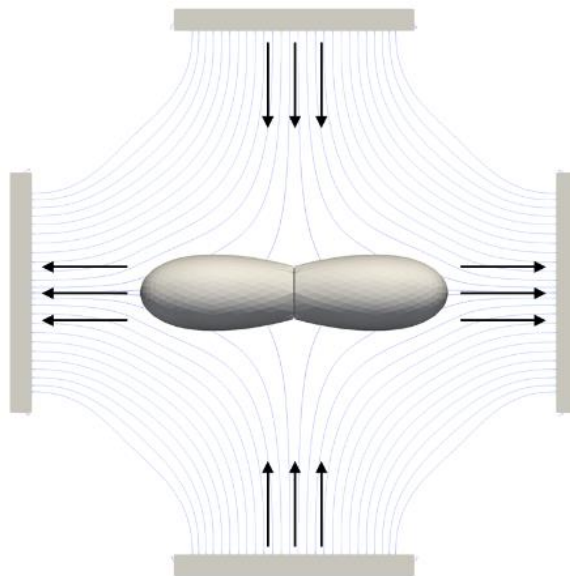


Figure 19: Cell separation using fluid flow [33]

By using both cell separation methods, we can adjust the adhesion parameters to achieve the desired adhesion strength. Considering cell adhesion measurements of other cell types found in the literature, $2 - 12nN$ between human embryonic kidney cells in [7] and $2 - 5nN$ for mesoderm and endoderm cells in [40], we have created a cluster that separates when an adhesion force of $1.6nN$ is applied. For a force lower than $1.6nN$, the cells in the cluster do not separate. The number of contact points determines the size of the contact area, with zero indicating that the cells have already separated. In Figure 20, the number of contact points is on the Y-axis and time is on the X-axis. The greater the separation force, the sooner the cells will detach. However, the smaller it is, the more it tends to settle at a constant number of contact points and the cells do not detach.

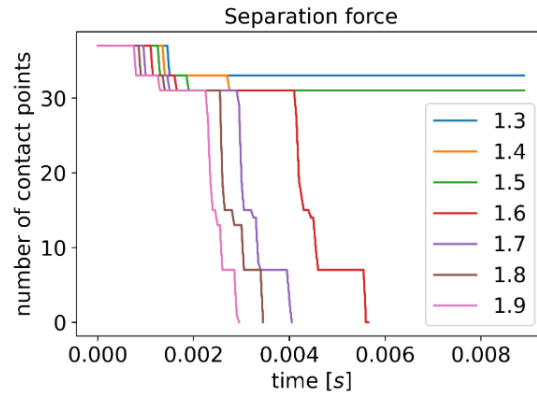


Figure 20: Contact area of two cells (represented by the number of contact points) in a pulling experiment with different magnitudes of separation forces (in nN) [33]

In [28], they studied the effects of elasticity on adhesion strength. Since we worked with three sets of elastic parameters in Table 3 for the cell membrane, we calibrated the LJ parameters in Table 4 for the most important soft and stiff elasticities.

Table 3: Simulation parameters of cluster membrane [33]

Elasticity:	Soft	Mid	Stiff
$k_s \left[\frac{\mu N}{m} \right]$	50	100	500
$k_b * 10^{-17} [Nm]$	5	10	50
$k_{al} \left[\frac{\mu N}{m} \right]$	20	100	500
$k_{ag} \left[\frac{\mu N}{m} \right]$	700	700	700
$k_v \left[\frac{N}{m^2} \right]$	900	900	900
no. of nodes per sphere	1002	1002	1002
cell radius [μm]	7.0	7.0	7.0

Table 4: Adhesion parameters of cell clusters [33]

	$\epsilon_{LJ} [fNm]$	$r_{min} [\mu m]$	$r_{cutoff} [\mu m]$
Soft	0.009	0.225	0.35
Stiff	0.02	0.25	0.4

3.1.2 Results based on different shear rate, elasticity and initial rotation

Results using different shear rate

In microfluidics, shear rate ($\dot{\gamma}$) is a measure of the rate at which adjacent fluid layers move relative to each other. It's often calculated using the following formula:

Equation 6: Calculation for shear rate

$$\dot{\gamma} = \frac{6Q}{wh^2}$$

Where:

- Q is the volumetric flow rate of the fluid (in m^3/s)
- w is the width of the microchannel (in meters),
- h is the height of the microchannel (in meters).

This formula assumes that the fluid flow is laminar and that the microchannel has a rectangular cross-section. In cases where the flow is not perfectly rectangular or laminar, more complex formulas or numerical simulations may be necessary to accurately calculate the shear rate.

Table 5: Physiological shear rates in vessels with different diameters [41], [42]

Type of blood vessel	Diameter of the blood vessel [μm]	Typical shear rate [s^{-1}]
carotid artery	4300 – 8200	260 – 500
coronary artery	2600 – 5000	100 – 350
mesenteric artery	410 – 660	170 – 330
intestinal vein	280	100
submucosal veins	120	200
capillaries	8	1000

The shear rate at the wall is affected by the diameter of the vessel. In large vessels such as the coronary artery with a diameter of 2 to 8mm, the wall shear rate reaches values between 100 and 500 s^{-1} . In medium-sized mesenteric arteries with a diameter of 410-660 μm , the wall shear velocity reaches values of 170-330 s^{-1} [41]. In smaller veins, e.g. submucosal veins with a diameter of 120 μm , the wall shear rate is up to 200 s^{-1} and in

Dynamics and obstacles: Exploring cell cluster behavior in simple shear flow and in bifurcated channels

capillaries with a diameter of $8\mu\text{m}$ it increases up to 1000s^{-1} [2]. An overview of the physiological shear rate in vessels of different sizes is summarized in Table 5.

In the upcoming sections, our focus will be on the z-axis, which we selected because we only need to consider one wall - the wall that the clusters may or may not encounter as shown in Figure 21. Both the centre of gravity coordinate z_c and the minimum coordinate z , z_{min} behave in a similar manner. This phenomenon was even more pronounced in [2], where they considered the cells to be completely stiff.

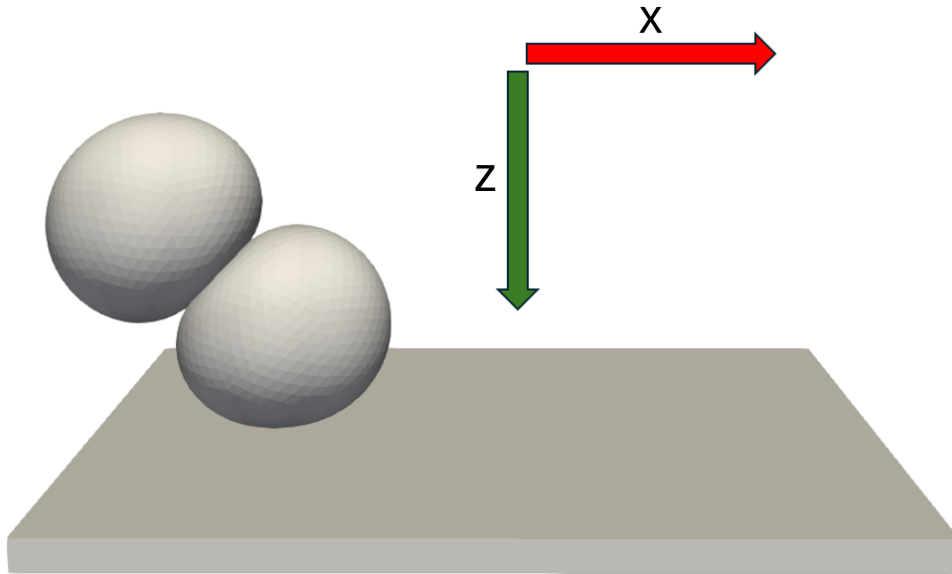


Figure 21: Illustration of x-axis and z-axis orientation

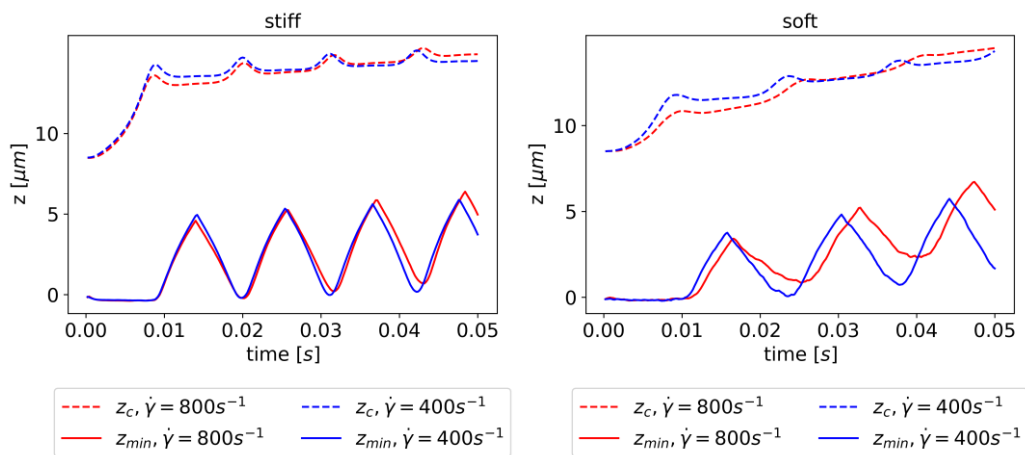


Figure 22: Model I. cluster centre coordinate z_c and minimum coordinate z_{min} shown after rescaling for (left) stiff doublet, (right) soft doublet [33]

The reason for considering different cluster models is shown in Figure 22 inspired by [2]. If we take two shear rates (400s^{-1} and 800s^{-1}), i.e. every second data point is taken

from the slower shear rate, we see that the behaviour for stiff Model I with strong adhesion is quite consistent - Figure 22(left).

If we do the same for the soft cluster Model I, Figure 22(right), we see that the correspondence is not as precise, and that the soft membrane slows down the overall motion of the cluster. Therefore, the use of Model I clusters is only appropriate when we know that the adhesive bonds of the modelled cells are very strong.

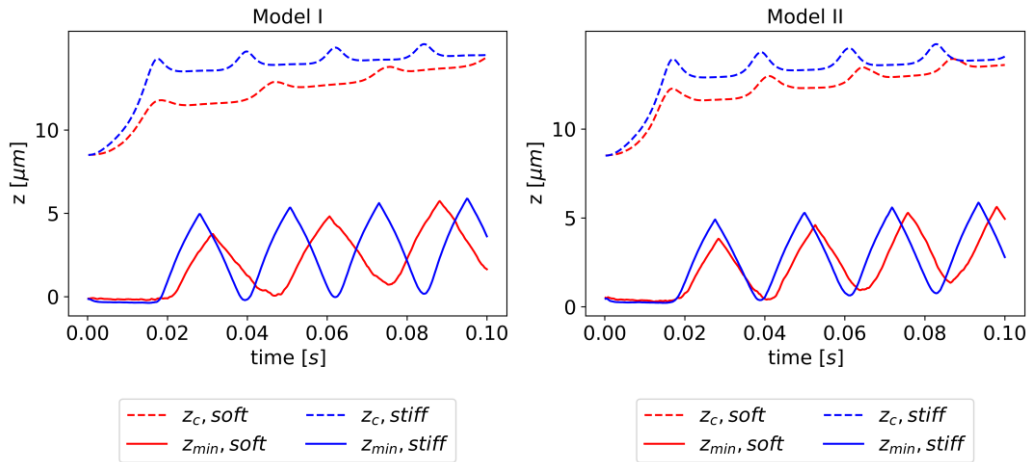


Figure 23: Doublet z_c and z_{min} at shear rate $400s^{-1}$. (left) Strong adhesion (Model I) (right) Weak adhesion (Model II) [33]

Allowing the cells to slide over each other (Model II) also changes the flow pattern, Figure 23. When we consider the contact area over time at exact shear rates of $400s^{-1}$ as shown in Figure 24, resulting in a cluster velocity of approximately $5mms^{-1}$, we see those clusters, with the exception of the stiff cluster with three Model I cells, tend to move away from the wall. At higher shear rates, this effect is even more pronounced.

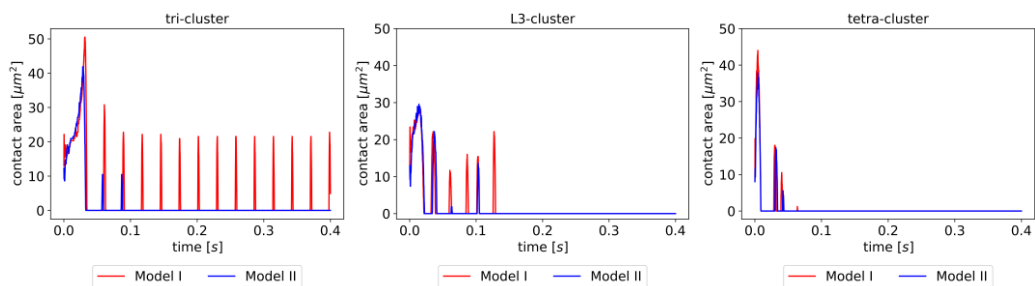


Figure 24: Contact area of stiff tri (left), L3 (mid), tetra (right) clusters at a shear rate of $400s^{-1}$. Only the tri-cluster Model I continue to repeatedly contact the wall. All other types investigated tend to move away from the wall [33]

Dynamics and obstacles: Exploring cell cluster behavior in simple shear flow and in bifurcated channels

In contrast, in simulations with lower shear rates, 100s^{-1} , simulated over 0.8s , Figure 25, we see that clusters other than the tetra-cluster encounter the wall more. At this shear rate, the cluster velocity is approximately 1.25mms^{-1} . The motion of the tri-cluster rod is the most regular, while the asymmetric shape of the L3-cluster causes irregular contacts with the walls.

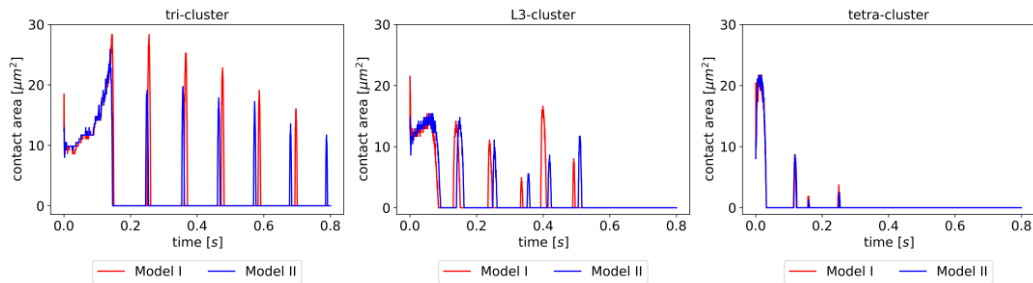


Figure 25: Contact area of stiff tri (left), L3 (mid), tetra (right) clusters at a shear rate of 100s^{-1} [33]

The previous observations can be summarized by saying that clusters made of more flexible cells tend to move away from the wall, and even this is true for clusters with weak adhesion composed of stiff cells. This suggests the general conclusion that non-stiff clusters made of either weak adhesion cells or soft elastic cells or both tend to move away from the walls at high shear rates.

We do not include the number of contacts as a separate metric because we are only able to see a few contacts during the simulated time, and the resulting number would be biased by an arbitrary time limit. However, comparing the two tri-cluster models, Figure 25 left, we see that Model II (more cells) results in a slightly higher rotation frequency and thus more contacts than Model I.

Results using different elasticity

In Figure 26 we can see the contact surfaces of the clusters with different elasticities while all other model parameters are the same. In Model II, the change in elasticity is more pronounced than in Model I. While the stiff clusters regularly contact the wall, the soft clusters stop contacting after the second contact. L3 and tetra-clusters travel away from the wall after the first few contacts.

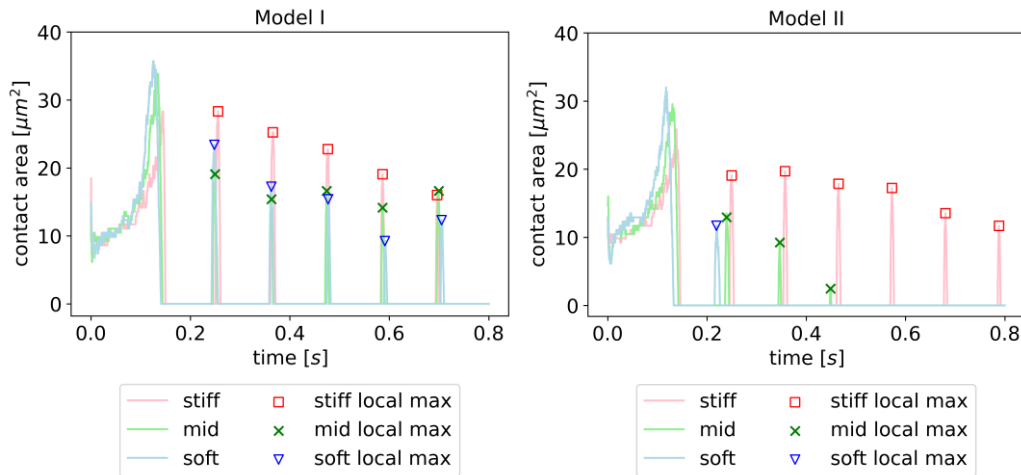


Figure 26: Tri-cluster with different stiffness in flow with shear rate 100s^{-1} . (left) Model I strong adhesion, (right) Model II weak adhesion [33]

The measurement of the contact area starts when there is no more initial contact. We measured at a shear rate of 100s^{-1} with a total simulation time of 0.8s. The last column indicates the number of contacts without initial contact during the observation period, with the + sign indicating that the cluster continues to move along the wall.

To assess and quantify the interaction between clusters and the channel walls, like our initial study of cluster models in branching points [32], we employ the following measures:

- tT – Total contact time during a specified period.
- $A_{contact}$ – Variable contact area
- A_{max} – Maximum contact area
- $TICA$ – Time integral of contact area over a designated time span.

The variable contact area enables the observation of variations in interactions among different models and their associated parameters. For example, Table 6 shows the contact metric for clusters at a shear rate of 100s^{-1} excluding the first contact. For soft cells, Model II has a shorter time and smaller contact area than Model I. The two models for stiff cells are similar in behaviour. The only difference is in the total contact area, which is slightly smaller in Model II than in Model I. Thus, if we use stiff clusters, we get similar results, but if soft, in which case we need to distinguish between the models to see which one is more suitable for our investigation.

Table 6: Contact area metrics without recording the initial contact [33]

Cluster type	Model	Elasticity	t_r [μ s]	TICA [μ m ²]	A_{max} [μ m ²]	Contacts
doublet	I	soft	13600	251	7.4	2
doublet	II	soft	4600	34	2.5	1
L3	I	soft	63000	2586	14.2	4+
L3	II	soft	52600	1796	14.2	4
Tri	I	soft	44000	2307	23.4	5+
Tri	II	soft	10600	401	11.7	1
Tetra	I	soft	32800	1229	17.3	3
Tetra	II	soft	19400	700	14.9	3
Doublet	I	stiff	6200	50	3.7	2
Doublet	II	stiff	6800	44	2.5	2
L3	I	stiff	65400	2753	16.6	5
L3	II	stiff	65200	2377	14.8	5
Tri	I	stiff	44200	3495	28.3	5+
Tri	II	stiff	43600	2476	19.7	6+
Tetra	I	stiff	17000	314	8.8	3
Tetra	II	stiff	16000	304	8.7	3

Another thing to notice in Table 6 is that the more spherical the geometries of the clusters are (tetra-cluster and doublet), the sooner they leave the contact wall. This property holds for both Models I and II.

To illustrate the cluster properties, we present snapshots obtained from the simulations. In Figure 27, we observe the intercellular sliding phenomenon occurring as the cluster moves; this observation pertains specifically to Model II. The initial contact area is highlighted in red, and each cluster's configuration is depicted after 0.2s of exposure to high shear rate 1200s^{-1} in shear flow. Notably, we observe a noticeable shift in the contact area over time.

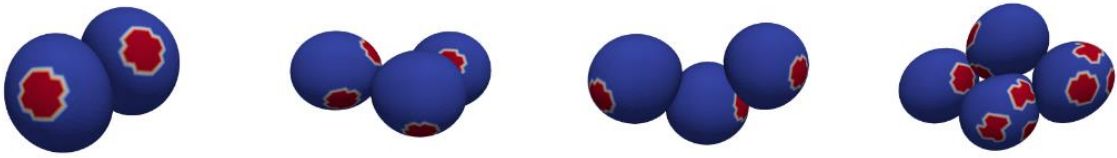


Figure 27: Model II, stiff bi, tri, L3 and tetra-clusters in flow with initial cell-cell contact areas are coloured red [33]

From Figure 28 to Figure 31 we can see the showcase of snapshots capturing the behaviour of the four cluster types near the wall. These snapshots offer insights into the flow dynamics in proximity to the boundary.



Figure 28: Snapshots of bi-cluster in shear flow near the wall [33]



Figure 29: Snapshots of tri-cluster in shear flow near the wall [33]



Figure 30: Snapshots of L3-cluster in shear flow near the wall [33]



Figure 31: Snapshots of tetra-cluster in shear flow near the wall [33]

Figure 32 provides a visualization of the physical regions of the cluster that encounter the channel wall during rotational movement. The intensity of the colouring corresponds to the duration for which individual mesh points remained in contact with the channel wall.

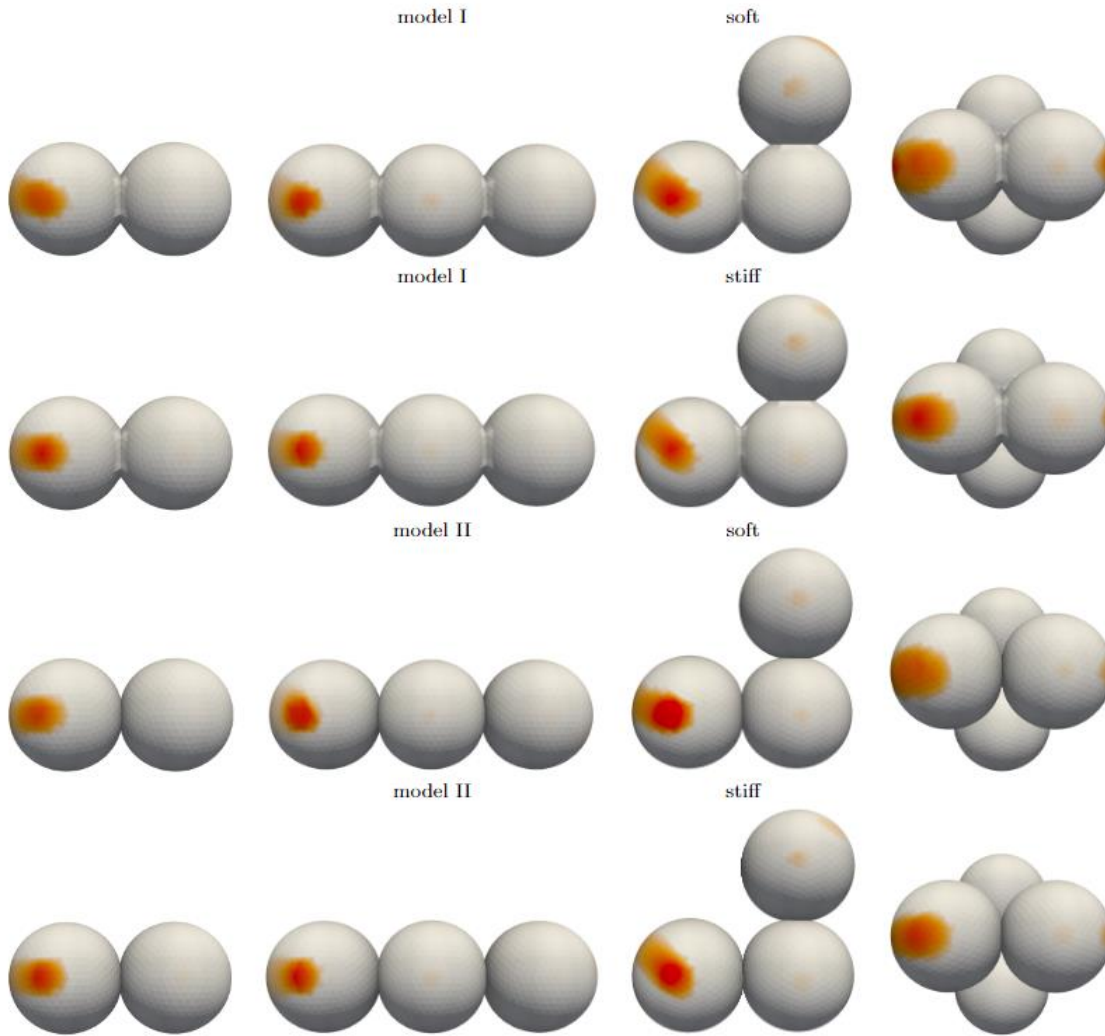


Figure 32: Heatmaps for soft and stiff clusters using both models [33]

The heatmaps depict the initial contact areas prominently. It's important to note that, for clarity, the colour scales vary between clusters, but remain consistent within each cluster type. For instance, the darkest colour represents $47ms$ of cell-wall contact for bi-clusters (first column), $118.4ms$ for tri-clusters (second column), $36.2ms$ for L3 clusters (third column), and $19.8ms$ for tetra-clusters (fourth column) over the 0.8-second simulation period.

Observations reveal that soft clusters exhibit larger contact areas, notably evident in tetra-clusters across both models. Furthermore, while the model does exert some influence on the placement of the contact area – as seen in comparisons between Model I and Model II soft bi-clusters – the primary determinant remains the geometric shape of the cluster.

Results using different initial rotation

Another important property that affects cell-wall contact. We used the four different orientations shown in Figure 33, where the x and y starting positions are all cells in contact with the wall, therefore these clusters have a larger initial contact area than the starting position z . To represent the *general* orientation, we used the initial rotation vector $[\pi/4, \pi/6, 2\pi/5]$, which means that the cluster was rotated $\pi/4$ in the X -axis direction, $\pi/6$ in the Y -axis direction, and $2\pi/5$ in the Z -axis direction.

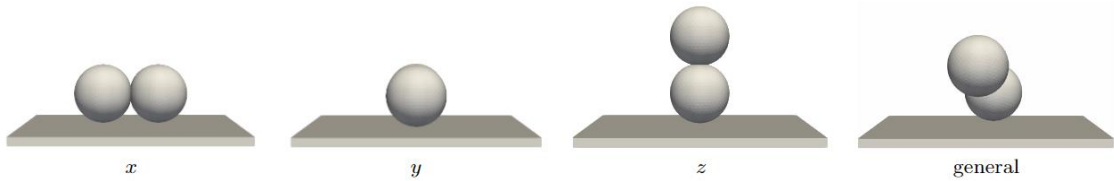


Figure 33: Doublet orientations named x , y , z and general $(\pi/4, \pi/6, 2\pi/5)$ [33]

In Figure 34 we see the minimum Z coordinate of the clusters that started from the initial four rotations. The x and z orientations resulted in a similar scrolling motion, with the x orientation reaching its first local maximum slightly later. This is due to the starting orientation having a larger area at the wall and being required to rotate to the z position.

In our understanding, a single period signifies the movement of a particular point (specifically, the lowest point in the initial z -axis position) around the entire circumference encircling the centre of the cluster. Consequently, this point effectively traverses an imaginary 360 degrees within one period.

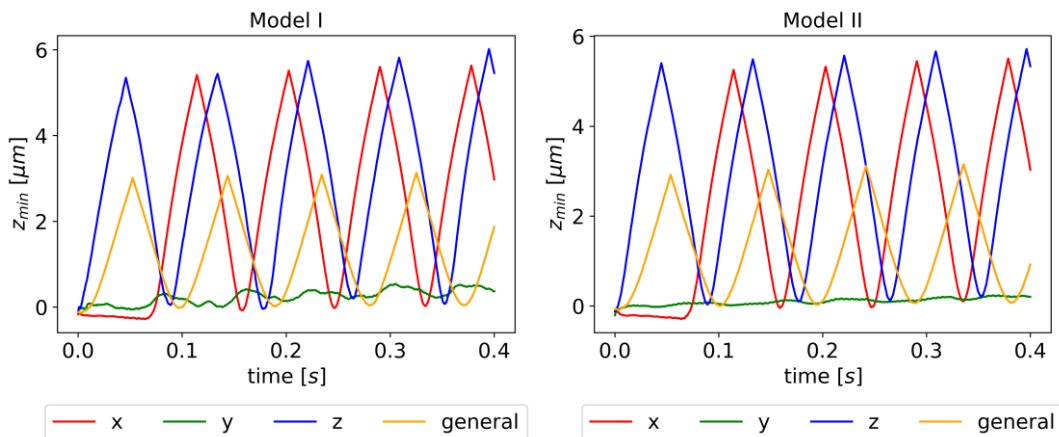


Figure 34: Minimum Z coordinate of the same stiff doublet cluster with four different initial orientations [33]

Therefore, the period and rotational frequency are the same for these two initial positions almost the same for the two models (0.175s , 5.71s^{-1} in Model I and Model II,

Dynamics and obstacles: Exploring cell cluster behavior in simple shear flow and in bifurcated channels

respectively). The general rotation shows a similar behaviour, but remains closer to the wall, up to $3\mu\text{m}$ (compared to almost $6\mu\text{m}$ for the x and z rotations) with slightly longer periods (0.182s in Model I and 0.188s in Model II), and hence a slightly lower rotational frequency (5.49s^{-1} in Model I and 5.32s^{-1} in Model II). Note that the y orientation is qualitatively different, as the two cells exhibit a movement along the wall like the wheels on an axle. In Model II, this motion is smoother.

The difference between the two models can also be seen in Figure 35, where the y orientation, z orientation, and *general* orientation have more contacts in Model I than in Model II.

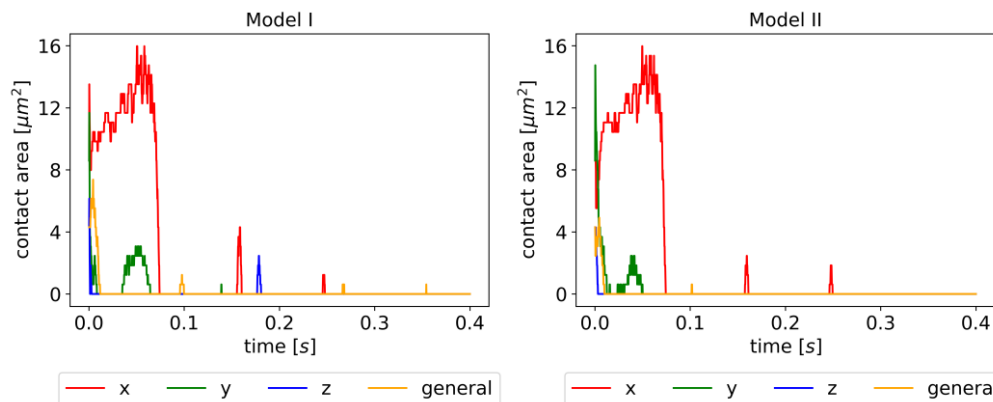


Figure 35: Contact area of the same stiff doublet cluster starting from four different orientations: x, y, z and general at a shear flow of 100s^{-1} [33]

3.1.3 Conclusion

In this paper we presented two types of models that could be used to simulate the behaviour of cell clusters under different flow conditions. The main aim was to represent the adhesion between two cells in a cluster. Model I brought the cells together in such a way that they were unable to separate. Model II, on the other hand, allowed gliding movement of one cell over another in the cluster and even allowed these cells to separate. We have described the construction of the cluster geometries for both models. We used the LJ potential to model the weaker adhesion that Model II had.

By varying the LJ potential, we were able to vary the adhesion strength to the desired values. We used two types of experiments for cell separation. The first mimicked separation using a micropipette and the second mimicked separation using only the forces of the fluid and its flow.

By varying the shear rate, we found that non-stiff clusters (consisting of either weakly adhesive cells or soft elastic cells or both) tend to move away from the walls at higher shear rates. This may seem surprising, as the general idea is that highly elastic cells stick to the walls of blood vessels and then move away. In this case, however, a different adhesion mechanism is involved, based on the formation of protein bonds between the cell membrane and the vessel wall [35]. In our work we have focused on purely hydrodynamic effects. The reason for this behaviour is the ability of the more elastic (or less adhesive) cells in the cluster to adapt to the surrounding fluid. This may be due to minimising rotational inertia by rearranging into a more spherical shape.

Clusters of soft cells associated with weak adhesion were able to adhere to the wall even at lower shear rates of 100s^{-1} . In general, however, it can be concluded that an increase in elasticity reduces the adhesion potential. We observed this behaviour both by reducing the total number of contacts and by reducing the contact area of individual cluster contacts with the wall.

Our final observation was related to the initial orientation of the clusters. In the case of vessel bifurcation, a cluster can enter one of the branches in different orientations. We have shown that this also affects the subsequent adhesion potential.

3.2 Simple bifurcation analysis

CTC clusters periodically divide from the main channel into daughter channels as they flow out of the primary tumour. Thus, during the division into daughter channels, there is regular contact with the vessel walls. We can model the behaviour of the clusters using a simple bifurcation. We will quantify CTC clusters based on the duration of contact and the size of the area of contact with the bifurcation wall. The main idea is that the longer the clusters stay near the cell wall, the higher their metastatic potential. If the time spent is the same, we take the size of the cluster contact area.

3.2.1 Cluster parameters

Important aspects of the observation were the duration of contact of the cluster or cell with the wall and the size of the contact area. We studied the effect of changing the following parameters on the touches:

- I. Elasticity of cells in a cluster
 - Lower and higher

II. Geometry of the cluster model

- Two or four-cell cluster

III. Microfluidic channel geometry

- Uncomplicated microfluidic bifurcation

IV. Initial cluster rotation

- Horizontal or vertical position in a two-cell cluster

We mainly distinguished between soft and hard cells. The change in membrane elasticity was also reflected in the size of the contact area of the cells in the cluster. It can be seen in Figure 36 that soft cells are able to deform more and thus have a larger contact area for the same LJ parameter settings.

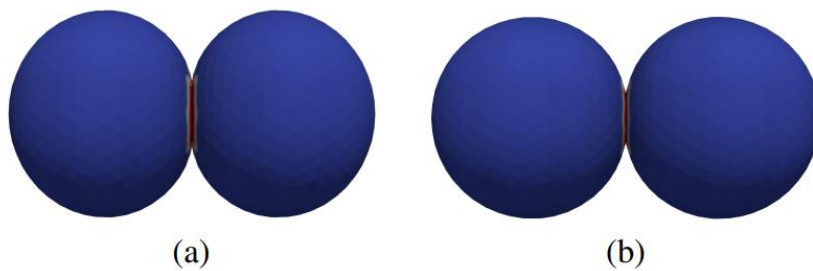


Figure 36: Difference between the contact area of soft (left) and stiff (right) cells [32]

The difference between softer and stiffer cells is in the local coefficients of elasticity. Soft cells are slightly stiffer than red blood cells, where stiffer cells are almost stiff. The values of the coefficients can be seen in Table 7:

Table 7: Values of local elasticity coefficients at lower and higher elasticity

	k_s [$\mu\text{N/m}$]	$k_b * 10^{-17}$ [Nm]	k_{al} [$\mu\text{N/m}$]	k_{ag} [$\mu\text{N/m}$]	k_v [N/m^2]
Soft	50	5	20	700	900
Medium	100	10	100	700	900
Stiff	500	50	500	700	900

For the experiments, we used the two-cell cluster model Figure 36 and the four-cell cluster model in Figure 13, which is a different four-cell cluster from the one in Section 3.1. Both models were populated with internal particles, and both ways of joining cells into a cluster were used in our simulations. We will refer to the model that was created by joining cells using the LJ potential as Model I and the model with uniform geometry as Model II. These models have been interchanged from the previous Section 3.1.

The initial rotation of the cluster is critical during its collision with the barrier. We have previously shown that clusters formed by LJ potential coupling can either reorganise or separate. When a doublet is oriented horizontally, the likelihood of cluster division into distinct cells is reduced. Conversely, vertical orientation of the doublet can induce cell separation upon impact, depending on adhesion forces and fluid velocity. The division of the initial cluster rotation into vertical and horizontal positions is due to the placement of the dividing wall, resulting in a straight bifurcation. The wall spans the entire width of the Z-axis, as shown in Figure 37. Since the cluster always repositions itself at the origin before colliding with the wall after a certain time, a vertically positioned doublet will hit its connected centre directly into the dividing wall. This phenomenon doesn't occur when the doublet is positioned horizontally.

3.2.2 Microfluidic channel geometry

Microvascular networks have a wide range of branching angles and daughter branch diameters, but to focus on the simple case, we designed an uncomplicated microfluidic bifurcation by placing the dividing wall in the centre of the 3D cuboid channel, Figure 37, where z-axis is represented by green arrow, y-axis by yellow arrow and x-axis by red arrow.

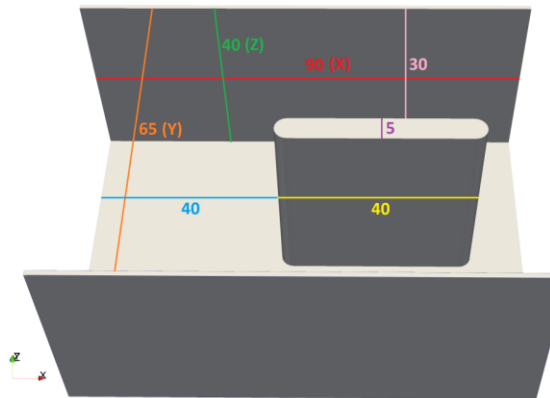


Figure 37: Simple bifurcation model [32]

The -coordinate of the centres of gravity of all clusters corresponded to the y-coordinate of the bifurcation wall, placing the clusters on a direct collision course with the bifurcation wall downstream from the x-direction. The length, width and height of the simulated region are $90\mu\text{m} \times 65\mu\text{m} \times 40\mu\text{m}$.

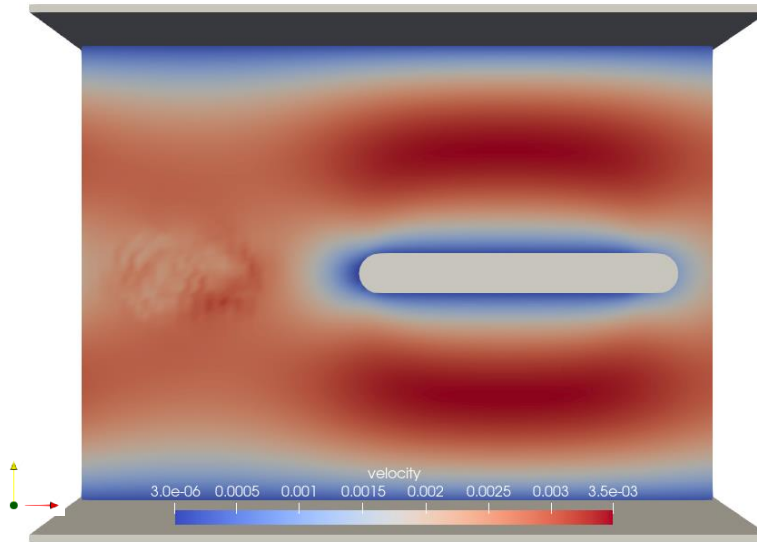


Figure 38: Fluid velocity in the model [32]

The fluid velocity profile shown in Figure 38 is located at the centre of the channel height. The maximum velocity was measured at the centre of the daughter channels, and it is approximately $\sim 35 \cdot 10^{-4} (\mu m) / (\mu s)$. The inhomogeneous region at the beginning of the model is due to the presence of a cluster at that location.

3.2.3 Contact area measurement

The basis for comparing the models and the elasticity effect is the examination of the contact area of the cluster with the partition wall. The contact area is calculated as:

Equation 7: Calculation of cluster contact area

$$A_{contact} = \frac{n_{contact}}{n} * S_{cluster}$$

Where:

- n is the total number of all grid points contained in the cluster,
- $n_{contact}$ denotes the number of grid points closer to the dividing wall than a certain distance, and
- $S_{cluster}$ represents the total surface area of the cluster.

For Model I, n excludes membrane points that form adhesive bonds with other cells in the cluster.

3.2.4 Results of simulation experiments

In Figure 39 we see the cluster-wall contact area (in % of total surface area) for the two two-cell models. The total cluster surface area was $598\mu\text{m}^2$. We can see that using both models, the softer clusters have a significantly larger contact area than the rigid clusters. This is most pronounced in model II, where the rigid relative position of the two cells leads to contact with over four percent of the total cluster area for almost the entire duration of the transition along the bifurcation wall.

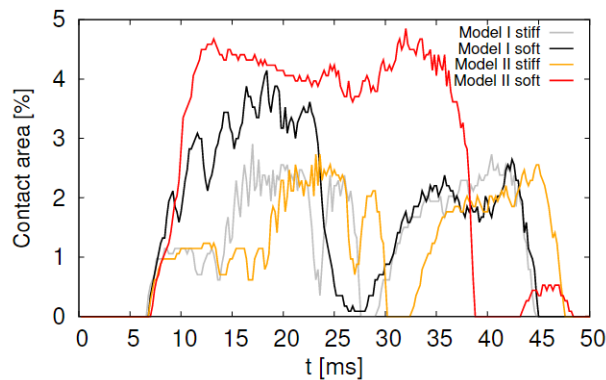


Figure 39: Contact area of clusters of two types - doublet, with different elasticity [32]

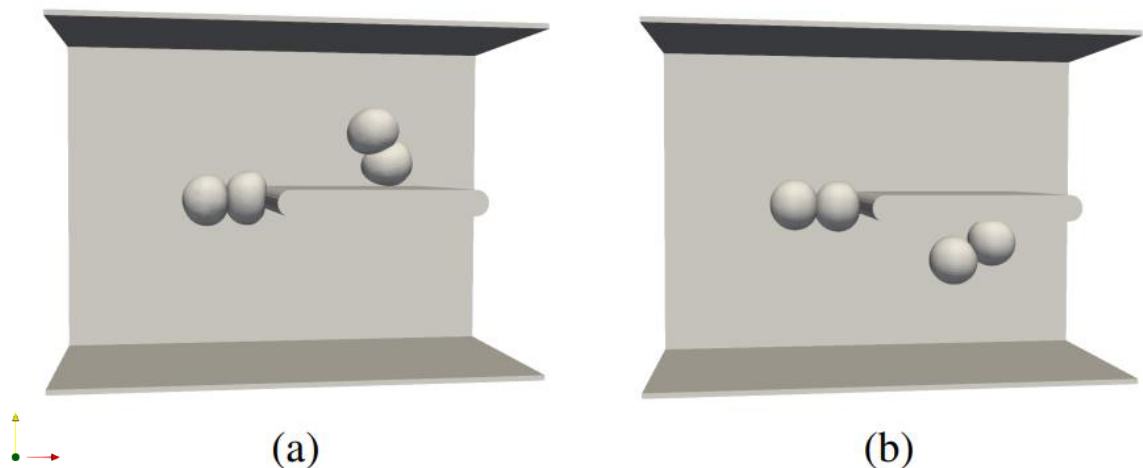


Figure 40: Soft (a) and stiff (b) doublet in horizontal initial position entering the bifurcation, both Model I

To illustrate, Figure 40 shows a doublet of Model I from Figure 39 at two different time steps. The cells are initially aligned horizontally and, in this position, encounter the bifurcation wall. The cluster then rotates either to the left or to the right with respect to the wall (the whole situation is symmetric except for the position of the inner particles) and moves along the dividing wall. The soft cells are compressed at the first impact.

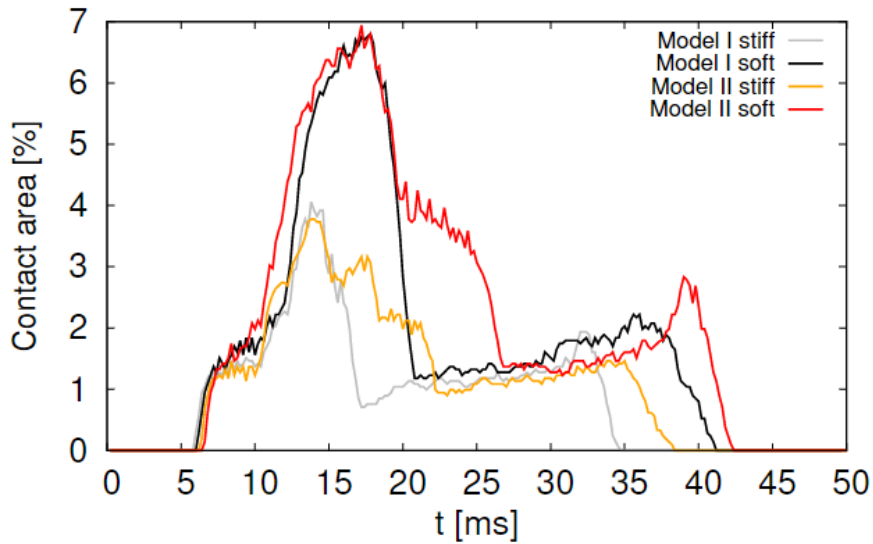


Figure 41: Contact area of clusters of two types - L4, with different elasticity [32]

In Figure 41 we see the contact area (% of total surface area) for two L4 cluster models with a total area of $1167\mu\text{m}^2$. Again, we see that the softer clusters have a larger contact area than the rigid clusters. We also see that in both the rigid and soft cases, Model II results in an elongated larger contact, again since the cells cannot change their relative position.

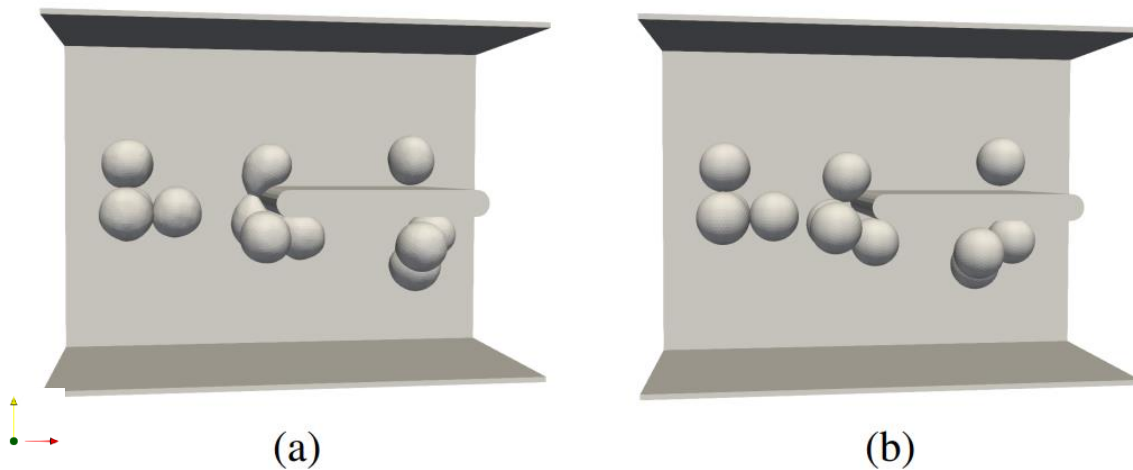


Figure 42: Soft (a) and stiff (b) L4 cluster entering the bifurcation, both Model I

Figure 42 shows a similar situation for the Model I - L4 cluster. Here we see that the cell adhesion bonds are not strong enough to hold the cluster together (unlike the Model II cluster, where the cells cannot separate, and all move together along one side of the dividing wall). To calculate the contact area over time, we include the contacts of all cells in the Model I cluster that are in contact with the wall, regardless of which side, because they should all be considered in terms of metastatic potential.

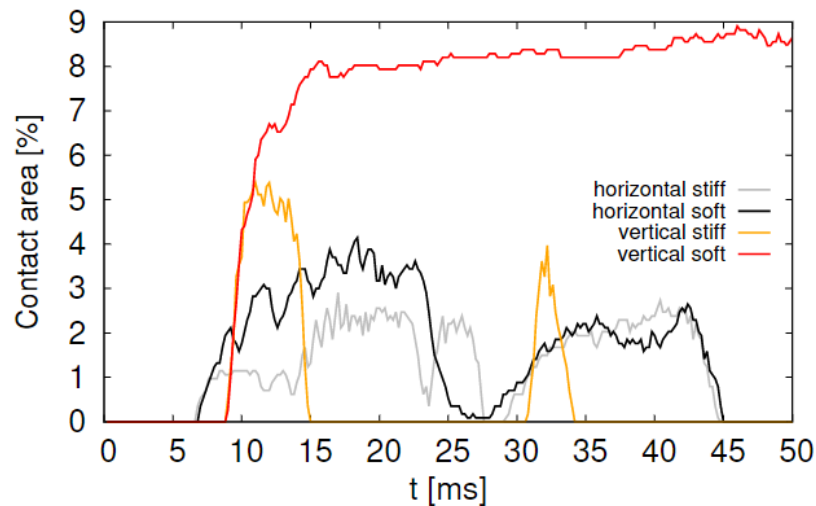


Figure 43: Horizontal and vertical initial position of the doublet [32]

Figure 43 compares the contact area over time for a Model I doublet with different initial orientations. We see that the soft cluster with vertical initial positioning spends significantly more time (and with a larger contact area; only the first 50ms shown) at the top of the bifurcation. During this time, it adapts and fits into one of the daughter branches.

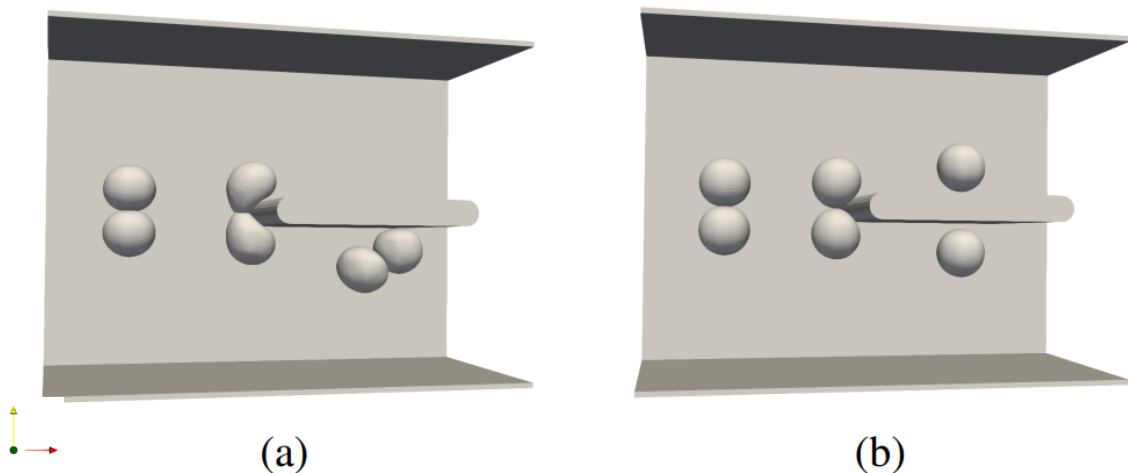


Figure 44: Soft (a) and stiff (b) doublet in vertical initial position entering the bifurcation, both Model I

Finally, Figure 44 shows the model I doublet with initial vertical placement. Like the L4 cluster result, in the rigid case, this initial orientation leads to the cluster breaking up when it hits the dividing wall. This does not happen for soft cells, which spend more time at the entrance of the bifurcation and thus have more time to break the symmetry of the situation, which then leads to the cluster slowly moving to one side of the dividing wall.

Dynamics and obstacles: Exploring cell cluster behavior in simple shear flow and in bifurcated channels

3.2.5 Conclusion

We have shown that although there are similarities between Model I and Model II, there is a significant difference in their behaviour. Model I can capture cells moving individually and even model cluster partitioning, so it appears to be more accurate. However, more research is needed because in some experiments with CTC clusters, e.g., [28], the clusters do not separate at the entrance of the bifurcation.

In both models, the softer clusters have a larger cell wall contact area than the rigid clusters over time, highlighting the need for careful biological measurements of CTC membrane properties.

We investigated the behaviour of two cluster geometries, a canonical case and a more complex one that offers more spatial variation. We used two different models that can capture the more complex cluster geometries. A similar analysis should be performed in the future with the inclusion of erythrocytes in the flow. Due to their typically larger volume fraction, they would influence the cell wall contact of the cluster and the pre-contact orientation (leading to differences in the results) through cell-cell interactions.

The model also offers the possibility to explore different bifurcation geometries, e.g. asymmetric cases, different bifurcation angles or simple channel networks. All of this can help elucidate the behaviour of CTC clusters and provide insight into the metastatic potential of cells in flow, which may lead to cancer treatment strategies.

4 PASSAGE OF CELL CLUSTER THROUGH CONSTRICTED CAPILLARY: VISCOSITY ANALYSIS

In the following chapters we discuss the geometry of the cluster, the strength of adhesion, the elastic properties of the cell and the effect of deformation on the cell in a confined environment.

4.1 Theory about cluster flowing through constricted capillaries

Human blood vessels, veins and capillaries have different diameters shown in Table 8:

Table 8: Typical diameters/thicknesses of blood vessel walls in humans in μm

	Aorta	Artery	Arteriola	Capillary	Venule	Veins
Human	2000-25000	1000-4000	20-30	1-8	2-20	500-5000

The smallest capillaries have a diameter of very few micrometres and a wall thickness of about one micrometre [43].

Sometimes the vessels are even narrower than the cell cluster, so it was long assumed that the cell cluster would not pass through the capillary or would split into individual cells that would no longer fuse together [3].

However, work [3] discusses the property of a cluster that "unrolls" just before entering the constricted capillary into a continuous chain of individual cells. At the end of the capillary, it can "collapse" again into a cluster of cells and travel further.

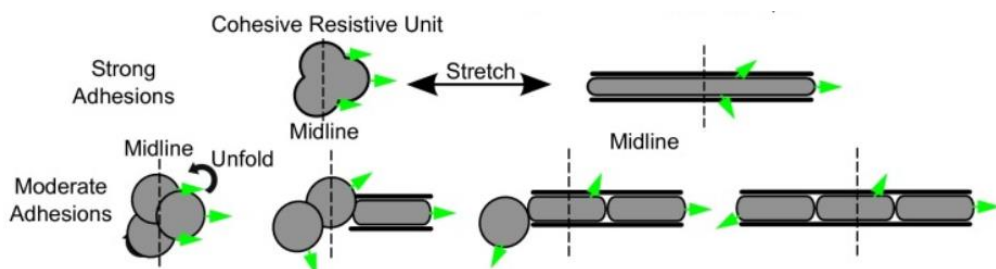


Figure 45: Comparison of strong and medium adhesion [3]

In Figure 45 we see the difference in the behaviour of clusters with different adhesion strengths in the constricted capillary. With strong adhesion, cell rotation is minimal, whereas with moderate adhesion, cell unrolling and rotation occurs. The strength of adhesion can also be identified in the simulation by the size of the area touched by the

cells in the cluster and a scalable parameter. The green arrows represent the direction of movement given by the resultant of the applied forces.

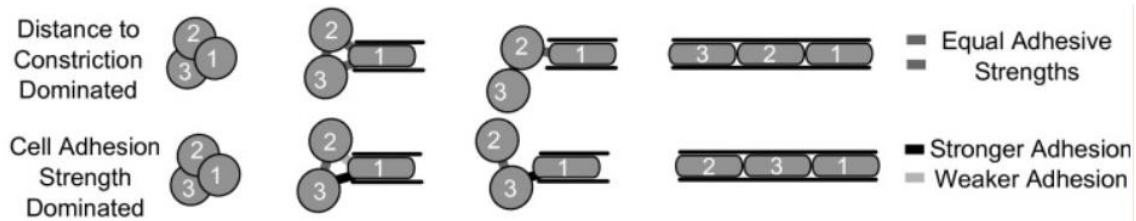


Figure 46: Different adhesion forces in the same cluster will cause a change in the order of the cells in the chain as they pass through the capillary [3]

In the first row in Figure 46, all pairs of cells have equally strong adhesion bonds. The second row does not have them the same, and this makes the weakest link break, and affects the order of the cells in the chain.

A cancer cell can pass through a constricted capillary at a certain fluid speed because of its ability to deform to fit the width of the capillary. In this chapter we will create a flattened model of a cancer cell with internal particles that we want to push through a constricted capillary. The deformation is done gradually, first flattening the spherical cell and then pushing the flattened cell into the capillary, to avoid many deformation forces acting on the cell as it enters the capillary. In biological experiments, a similar effect is achieved by using a gradually narrowing channel.

We will run our model of a flattened cancer cell with a thin and a dense membrane. A sparse membrane contains fewer lattice points, so fewer points interact with the capillary wall or internal particles.

Next, it depends on how the fluid is introduced into the model. We distinguish between fluid motion with a fixed boundary condition, which will be an imaginary initial wall at the beginning of the simulation domain, filling the entire simulation domain with fluid in this way. The advantage lies in the ability of the fluid points to change the direction of flow based on the geometry of the simulated region.

The entire simulation domain is filled with fluid points that do not move. The fluid is discretised and its velocity is calculated at each point of the discretisation. During the simulation these points do not change their flow direction.

4.2 Flattened cancer cell model

Initially, we chose the particle volume as 0.6 times the whole cell volume because of the assumed cell deformation. We started with a round cell radius of $10\mu\text{m}$. In Figure 47 we can see the free spaces for the internal particles at the top and bottom of the cell, so that the particles have more space to better accommodate the excessively large deformation of the cell as it enters the constricted capillary. The number of internal particles in the figure is 3727 and the number of membrane grid points is 4722.

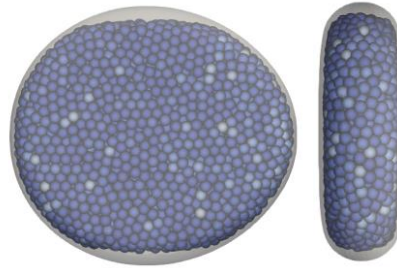


Figure 47: First model of a flattened cancer cell filled with internal particles



Figure 48: Initial model of a constricted capillary with a cancer cell

In the simulation domain, we initially set the fluid velocity to $4 \cdot 10^{-4}(\mu\text{m})/(\mu\text{s})$, [3]. The length, width and height of the simulated region are $120\mu\text{m} \times 60\mu\text{m} \times 9\mu\text{m}$, Figure 48. The width of the capillary in the figure is $8\mu\text{m}$ and the length is $50\mu\text{m}$. The disadvantage of the settings of the simulation region and cancer cell model was mainly that the cell failed to fit into the constricted capillary in most cases. The model and simulation region needed to change some of the key properties based on the results of the simulations performed to achieve the desired state:

- I. Fluid flow velocity
 - a. Fluid Acceleration
 - i. Less likelihood of the cell getting stuck on the walls when entering the constricted capillary
 - ii. Approximating cell velocity to a biological experiment [3]
- II. Ensuring numeric stability
 - a. Changing cell-wall interaction parameters
 - i. The cell can respond earlier to impending deformation due to a constricted capillary
 - b. Change in membrane network density from sparse to dense - average membrane edge length
 - i. Increasing the number of interactions with the cell membrane
 - ii. Preventing internal particles from exiting the cell in a constricted space
 - c. Change in internal particle volume relative to the cell
 - i. Sufficient filling of the internal environment of the cell
- III. Total fluid movement
 - a. Initialize fluid velocity at all points in the simulation domain, not just at the edge
 - i. Easier passage of a cell through a constricted capillary
- IV. Specified size range of the cancer cell model
 - a. Changing cell dimensions
 - i. Large cells could not enter the capillary, so we worked with smaller cell sizes

4.3 Modified flattened cancer cell model

We increased the particle volume to 0.74 times the whole cell volume because of the assumed cell deformation. We reduced the radius of the modified cell model to $6\mu m$. In Figure 49 we can see that almost the entire internal environment of the cell is filled with internal particles. The number of internal particles in the figure is 862 and the number of membrane grid points is 4022. To compare the membrane density, we measured the average edge length for the previous large cell - $0.64\mu m$ and this modified one - $0.39\mu m$.

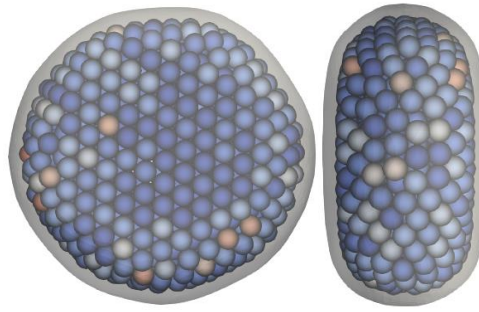


Figure 49: Final model of a flattened cancer cell filled with internal particles



Figure 50: A modified model of a constricted capillary with a cancer cell

In the simulation domain, we initially set the fluid velocity to $781 * 10^{-6} (\mu m) / (\mu s)$. For comparison, the capillary width is $7 \mu m$ and the length is $90 \mu m$. The length, width and height of the simulated region are $200 \mu m \times 60 \mu m \times 9 \mu m$, Figure 50.

4.4 Comparison between our simulations and biological experiments

Our aim was to approximate the results of the biological experiments in the paper [3], comparing results based on cell velocity (Y-axis) and cell size versus capillary width (X-axis), Figure 51. The graph shows the results for the individual cells (filled markers) that we wanted to compare with.

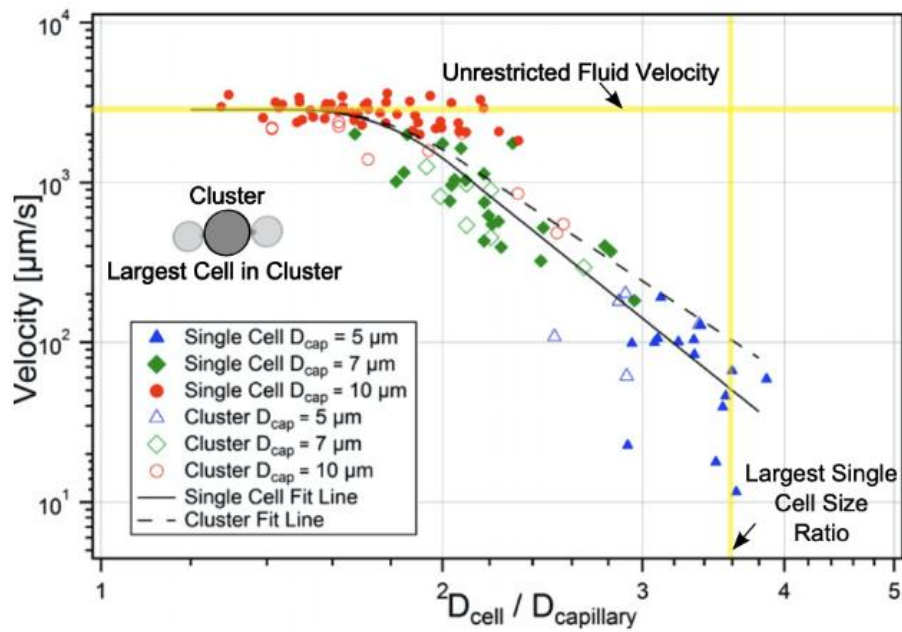


Figure 51: Comparison of the speed of cells and cell clusters with respect to their size and the size of the constricted capillary [3] - biological experiment

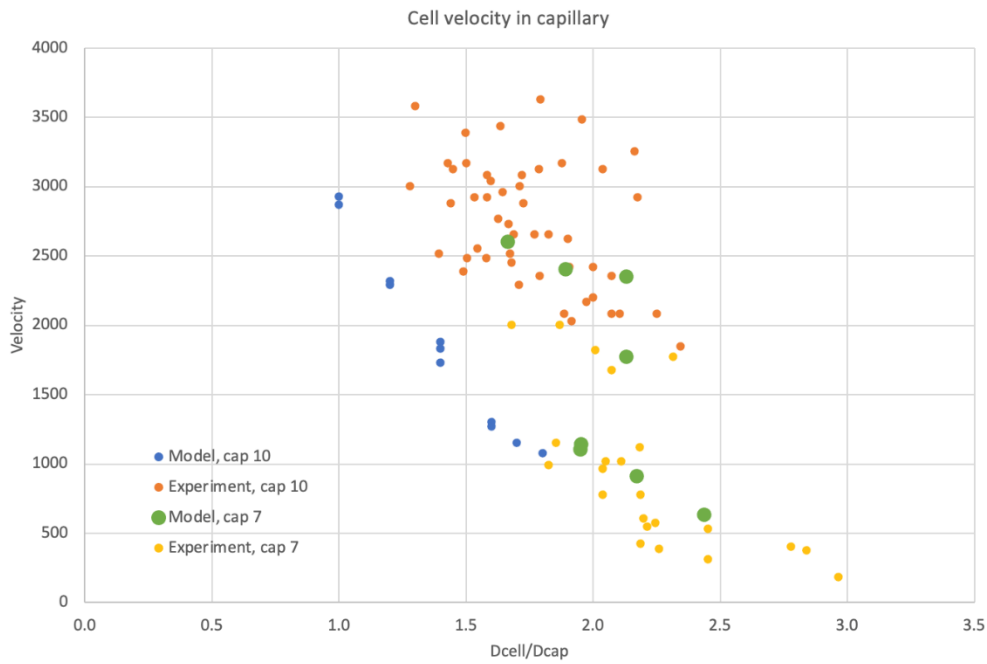


Figure 52: Comparison of the velocity of cells and cell clusters with respect to their size and the size of the constricted capillary - our model

In Figure 52, the green and blue points represent our experimental results, which we compared with the yellow and orange points. We can see that the results of the initial

model with a capillary width of $10\mu\text{m}$ differ from the biological experiments, while the modified model scaled down to a width of $7\mu\text{m}$ tends to acquire similar results.

The Y-axis represents a linear scale in our case, due to the better distribution of points on the graph for greater clarity. The labelling of the X-axis remains the same as in Figure 51. As an advantage, we can take the fact that cells of different sizes were able to pass through the constricted capillary at the desired velocity. However, the time requirement increased several times for the modified model. Thus, we created a model of a cell with internal particles that behaved similarly to a biological cell when passing through a $7\mu\text{m}$ wide capillary.

4.5 Conclusion

In conclusion, our study aimed to align computational simulations with biological experiments outlined in [3], focusing on the correlation between cell velocity (Y-axis) and cell size relative to capillary width (X-axis), as depicted in Figure 51. By comparing individual cell data (filled markers) with our experimental results illustrated in Figure 52 (green and blue points), juxtaposed with reference points (yellow and orange), we observed a notable discrepancy between the initial model, utilizing a capillary width of $10\mu\text{m}$, and the biological experiments. However, upon scaling down the model to a width of $7\mu\text{m}$, a closer resemblance to the experimental results emerged. Notably, our model allowed cells of varying sizes to traverse the constricted capillary at the desired velocity, underscoring its potential applicability. Nonetheless, the modification led to a substantial increase in computational time. Despite this, our refined model successfully mimicked biological cell behaviour within a $7\mu\text{m}$ wide capillary by incorporating internal particles.

5 DEAN INERTIAL FLOWS FOR CELL AND CLUSTER SEPARATION

5.1 Theory about inertial focusing and object separation

Inertial microfluidics is a rapidly developing field that exploits microscale fluid dynamics to precisely manipulate particles and cells. Specifically, under certain conditions in microfluidics, fluid inertia overcomes viscous forces, allowing for the precise control and manipulation of particles suspended in the fluid. This principle has led to the development of innovative techniques for sorting, focusing and separating particles based on size, shape and deformability. [13].

Applications of inertial microfluidics span a wide range of fields, including biomedical diagnostics, drug delivery systems, tissue engineering and environmental analysis. For example, inertial microfluidic devices have proven valuable in high-throughput cell sorting, facilitating the rapid and efficient isolation of specific cell populations for various biomedical research applications [21]. In drug delivery, inertial microfluidics enables controlled encapsulation and release of therapeutic agents, increasing the precision and efficiency of targeted drug delivery systems.

In straight channels, particles undergo lateral migration, known as cross-streamline migration. This migration results from the balance between wall interaction lift forces and shear gradient lift forces, enabling size-based particle focusing and sorting [14]. However, focusing cells in straight channels often requires extended lengths.

In curved channels, an additional cross-streamline effect known as the Dean effect comes into play. This effect results from centrifugal forces generated by curvature-induced secondary flows and is characterised by the Dean number. It induces a lateral displacement of particles towards the outer wall, leading to the formation of different equilibrium positions depending on particle size. Researchers have exploited the Dean effect to develop curved microfluidic platforms for size-based particle filtration and fractionation, facilitating efficient particle manipulation and enrichment [44].

Long spiral channels, characterised by a continuous and gradual curvature along their length, provide enhanced particle focusing and sorting capabilities. Particles experience a constant Dean drag defined by the cross-streamline velocity profile. At low Dean numbers, two opposing Dean vortices are formed, while at high Dean numbers, four Dean vortices can be formed [15]. The extended exposure of particles to the constant Dean flow in long spiral channels enhances their focusing and sorting capabilities [16].

In a study conducted by researchers [5], a spiral microchannel with a trapezoidal cross-section was employed to accentuate the Dean effect. In this experiment, a mixture of larger and smaller cells was injected at the inlet. As the mixture traversed the spiral, smaller cells tended to accumulate near the outer wall of the channel, while larger cells accumulated near the inner wall. This behaviour is a result of the balance between Dean and lift forces in the flow. As a result, larger cells could be effectively separated from smaller cells at the outlet of the spiral.

Conversely, meander-like channels consist of repeated U-shaped or S-shaped bends, or zigzag patterns, introducing complex flow patterns and particle behaviour due to inertial effects [17]. The meandering geometry introduces a combination of inertial lift forces, Dean drag forces and secondary flows, resulting in a more complex phenomenon of particle manipulation. Particles experience a combination of lateral migration, particle trapping and focusing effects at different sections of the channel.

Meandering channels alternate between sections of positive and negative curvature. In sections with positive curvature, Dean forces create two Dean vortices, while in sections with opposite curvature, the orientation of these vortices switches, resulting in four Dean vortices. This switching effect can be visualised using tracers flowing through multiple sections of the channel, as demonstrated in an experimental study using two bends with opposite curvature, creating four Dean vortices [18].

In another experimental study [19], researchers focused on the high-throughput extraction of plasma using a secondary flow-aided inertial microfluidic device. The study presented the development of a simple serpentine channel inertial microfluidic device for the efficient separation of blood cells from plasma. The mechanism of operation of the device is based on the bi-directional secondary flow assisted inertial focusing of particles in a serpentine channel. Specifically, blood cells were focused along two sides of the channel, while blood plasma was efficiently collected in the cell-free region at the centre of the channel.

5.2 Computational models

To achieve the objectives outlined in the previous section, we use computational models that include immersed particles (representing relatively rigid cells) and clusters of cells.

The particles, cells or cell clusters are collectively referred to in this study as immersed objects. These objects consist of one or more spheres that are connected to

each other. The nature of these spheres, whether they remain circular or deform into ellipsoidal shapes, depends on the rigidity of the objects. The representation includes a tetrahedral mesh that covers the entire volume of the immersed object. This mesh forms a spring network where each edge of a tetrahedron acts as an elastic spring. By adjusting the stiffness of these springs, the elastic or rigid behaviour of the submerged objects can be adjusted.

In Figure 53, the left side illustrates the tetrahedron mesh for a single spherical object, representing either a rigid particle, a rigid cell, or, in some instances, elastic cells. Additionally, Figure 53 depicts three types of clusters: a bi-cluster comprising two spherical cells of the same size, a four-in-line cluster with four spherical cells of the same size aligned in a straight line, and a tetra-cluster composed of four cells of the same size arranged in a rectangular tetrahedron.

The selection of these clusters reflects common cell arrangements often observed in cell suspensions. Although there are numerous other arrangements, varying in cell position, size and cluster size, we have chosen a relatively small number of clusters for clarity. The doublet represents the most common configuration. The choice of a four-in-line cluster was made to introduce a cluster that is significantly larger in one dimension than the other two, with the aim of investigating whether such a linear cluster exhibits different behaviour to spheres. Finally, the tetrahedron cluster was chosen because of its similarity in shape to a large sphere, allowing us to investigate whether large cell models could serve as proxies for such clusters.

To track the long-term evolution of the fluid, we use tracers as dimensionless points immersed in the fluid. These tracers also propagate due to the dissipative force. As they are dimensionless, their effect on the fluid is negligible and their propagation mimics that of the fluid streamlines.

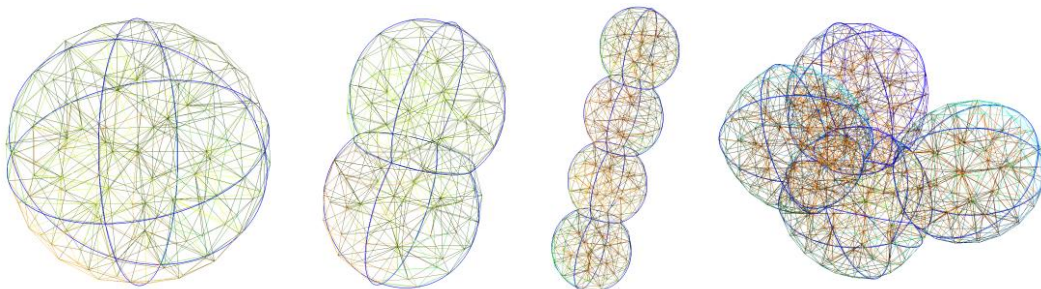


Figure 53: Different cell cluster models

5.3 Dean flow in curved channels

In a straight channel, only two competing forces operate in the main axial direction: Wall interaction lift forces (illustrated on the left in Figure 54) and shear gradient lift forces (depicted in the middle). The Dean effect is not present in straight channels. However, in serpentine or spiral geometries, a secondary flow perpendicular to the main coordinate of the flow can be observed due to centrifugal forces (shown on the right in Figure 54). While the magnitude of the Dean flow velocity is two orders lower than the magnitude of the main axial velocity flow, it significantly influences immersed particles, compelling them to traverse transversely across the channel cross-section.

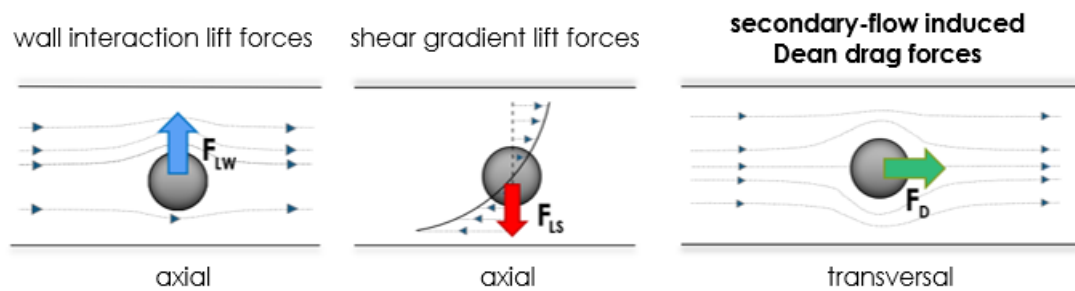


Figure 54: Competing inertial forces in curved channels

The strength and actual direction of the lift and Dean forces depend on several variables. The formula for the magnitude of the lift and Dean force acting on a small spherical particle can be theoretically derived using quantities such as lift coefficient, shear coefficient (both dependent on particle position and Reynolds number), fluid density, maximal fluid velocity, particle diameter, hydraulic diameter of the channel, and the Dean number. The Dean number is defined by the Reynolds number (Re), the curvature radius of the channel (R_c), and the hydraulic diameter of the channel (D_h). For meander-like channels, where the curvature may change, the Dean number may vary from place to place. We can see the dependencies in the following Equation 8:

Equation 8: Definition of Dean Number

$$De = Re \sqrt{\frac{D_h}{2R_c}}$$

The interplay between wall-induced forces, shear-induced forces, and the Dean force is complex, determining the cross-sectional trajectory of a particle. There is no absolute agreement in the literature on the formulas for evaluating Dean forces, and even for existing formulas, numerous assumptions must be satisfied for their validity.

Additionally, position-dependent lift and shear coefficients make the evaluation of forces challenging. Therefore, actual simulations of channel flow with immersed particles are extremely valuable for studying the stabilized positions after focusing.

5.4 Inertial focusing and separation using initial geometry

5.4.1 Microfluidic channel geometry

To study the Dean effect, we used an initial square S-shaped model where right and left turns alternate. In Figure 55, we illustrate two repeating sections of the S-shaped channel. The uniform inlet and outlet are positioned on the left and right sides of the channel. Tracers are continually re-seeded to the seeding line upon reaching it.

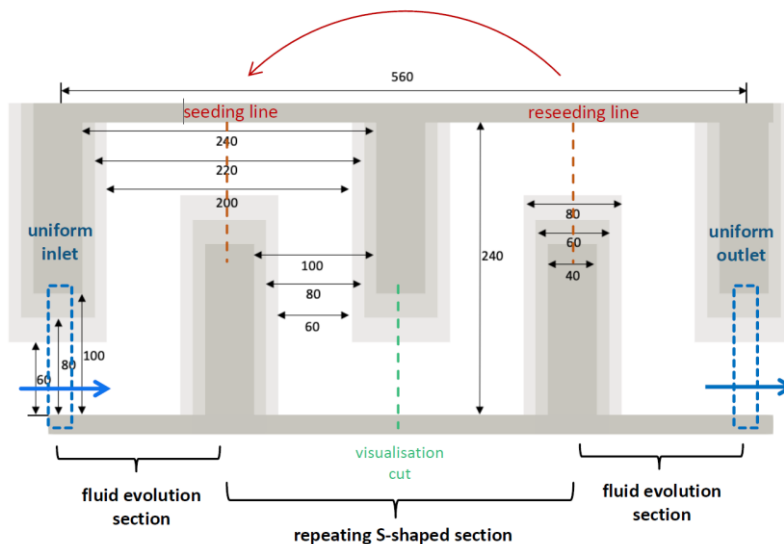


Figure 55: Rectangular channel geometry

This approach allows the tracers to experience the flow as if they were continuously passing through an extended meandering channel. In subsequent sections, we seed and reseed submerged particles and clusters in a similar manner to the tracers.

The simulation box encompasses three cases of cross-sections, each consisting of one repeating S-shaped section enlarged by two fluid evolution sections. The darkest boundaries represent a cross-section of $100 \times 32 \mu\text{m}$, the medium-dark boundaries represent $80 \times 40 \mu\text{m}$, and the brightest boundaries represent $60 \times 52 \mu\text{m}$. The seeding and reseeded line is depicted in red, while the green colour represents the visualization cut for

Dean effect visualization, and the blue colour designates the uniform fluid inlet and fluid outlet.

As we investigate three different cross-sections, the corresponding dimensions of the channels vary for each case. These dimensions are illustrated in Figure 55. It's important to note that the lengths along the axial centre of the channel are consistent.

To define the specific geometry of a serpentine channel, we utilize geometrical shapes such as rhomboids in the ESPResSo scientific simulation package with the PyOIF module [27].

After the initial seeding of tracers (particles and clusters in later sections) at the beginning of the flow on the seeding line in the channel, we record the positions of the tracers (origins of particles and clusters respectively) throughout the flow. When the tracers reach the reseeding line, we reseed them back to the seeding line. This reseeding process, depicted in Figure 55, allows us to simulate a periodic flow without physically constructing the real microchannel.

5.4.2 Fluid set-up

To allow the static fluid at the beginning of the simulation to fully evolve, we conduct a simulation for $500\mu\text{s}$ without the presence of particles. The uniform boundary conditions at the inlet and outlet establish the average velocity in the channel, which is proportionate to the volumetric flow rate. This is achieved in PyOIF using a special velocity boundary, visualized in Figure 55 by dashed rectangles, with predefined constant values of the velocity field at the boundary points. The specific values of the inlet conditions and the corresponding flow rates are detailed in Table 9. Values in channels with other cross-sections are similar.

Table 9: Fluid parameter in rectangular channel with cross-section $80\times 40\mu\text{m}$

Average velocity [m/s]	Reynolds number [-]	Volumetric flow [mL/min]
0.18	19.2	34.56
0.35	37.3	67.2
0.45	48	86.4
0.6	64	115.2

The volumetric flow rate (Q) in fluid dynamics is typically calculated using the Equation 9:

Equation 9: Volumetric flow rate

$$Q = A * V$$

Where:

- Q is the volumetric flow rate,
- A is the cross-sectional area of the pipe or channel through which the fluid is flowing,
- V is the velocity of the fluid.

This equation essentially states that the volumetric flow rate is equal to the product of the cross-sectional area and the velocity of the fluid. It is a fundamental equation in fluid dynamics and is commonly used to analyse and quantify the flow of fluid through pipes, channels or other conduits.

In our study, we focus on investigating flows under conditions that are physiologically relevant. We simulate a fluid with a density and viscosity like physiological solutions, or water, with values of 1000kg/m^3 and $10^{-3}\text{Pa}\cdot\text{s}$ respectively. In the field of inertial microfluidics, the relevant range for the Reynolds number extends up to 100 [45]. The Reynolds number (Re) is typically calculated using an equation:

Equation 10: Reynolds number

$$Re = \frac{\rho * v * D}{\mu}$$

Where:

- ρ is the fluid density (kg/m^3)
- v is the fluid velocity (m/s) – typically measured at the centre of the channel
- D is the hydraulic diameter (m) – for rectangular microchannels: $D = \frac{2*a*b}{a+b}$
- μ is the dynamic viscosity of the fluid ($\text{Pa}\cdot\text{s}$)

To explore a diverse range of flow conditions, we consider four different average velocities, reaching up to 0.6m/s in the channel, resulting in Reynolds numbers up to 64. The maximal velocity, used for Reynolds number evaluation, is set as twice the average velocity. With a cross-sectional area of approximately $3100\mu\text{m}^2$, this corresponds to a volumetric flow rate of up to 115.2mL/min .

5.5 Results using initial geometry

In this section we examine the behaviour of cell clusters within S-shaped channels. We analyse four different clusters, noting that technically one of them is a single cell. However, for the purposes of this section, we will refer to this single cell as a cluster of cells, depending on the context.

During the experiment we used four different models and compared them. Our initial focus was on a single cell, and then we moved on to clusters of two to four cells arranged in different configurations. The chosen cell and cluster models were chosen to cover a wide range of scenarios that may occur during fluid flow. Specifically, we used the single cell model and the cluster models: doublet, four-in-line and tetrahedron cluster. The single cell and doublet were chosen because of their common occurrence, the four-in-line cluster because of its elongated shape, and the tetrahedron cluster because of its close resemblance to a compact spherical shape.

Our investigation focused on two different scenarios. In the first scenario, all cells making up the clusters were the same size, with a diameter of $10\mu\text{m}$. In the second scenario, we maintained the size of the four-in-line and tetrahedron clusters, while increasing the diameters in the single cell model and the doublet. This adjustment was made to ensure that the single cell and doublet had the same volume as the other two clusters. The standardized cell diameter in the initial scenario was established at $10\mu\text{m}$, as informed by an experimental study [2]. Table 10 provides an overview of the cluster parameters.

Table 10: Overview of cluster parameters

	Fixed cell size scenario		Fixed cluster volume scenario	
	Cell diameter (μm)	Cluster volume (μm^3)	Cell diameter (μm)	Cluster volume (μm^3)
Single cell	10.0	524	15.88	2094
Doublet	10.0	1047	12.6	2091
Four-in-line	10.0	2094	10.0	2095
Tetrahedron	10.0	2094	10.0	2097

Simulations were conducted using defined geometries with cross-sections of $60 \times 52 \mu\text{m}$, $80 \times 40 \mu\text{m}$, and $100 \times 32 \mu\text{m}$. Due to the larger spatial size of the clusters, it was necessary to generate initial positions close to the channel centre plane. As a result, the initial seeding approach for clusters differed from that for single cells. After generating their positions, the four-in-line clusters were aligned with the flow direction and then given a slight tilt.

To track the clusters beyond the visualisation section within the flow, we recorded their positions within the channel. Each cell or cluster underwent 21 passes and each simulation contained 28 objects, whether cells or clusters. The number of objects was chosen randomly due to the computational power of the simulations. As more cells are used, the computational effort increases either linearly or exponentially, depending on the number of different interactions used. These objects were evenly distributed within the specific simulation.

5.5.1 Quantitative analysis of flow patterns

In studying the Dean flow patterns, our initial focus was on the Y dimension, which provided a partial insight into the movement of various objects within the flow during the simulations. The aim was to understand whether objects would be concentrated in the centre of the channel or to the sides. From Figure 56, it is evident that most clusters tended to concentrate in the centre, primarily influenced by the chosen channel dimensions.

The comprehensive analysis of the model behaviour with respect to varying volumes and diameters along the Y-coordinate is presented. Four different fluid velocities were investigated, indicated by different colours from slowest (orange) to fastest (blue). All plots represent 21 runs, with each row corresponding to a specific channel geometry: $60 \times 52 \mu\text{m}$, $80 \times 40 \mu\text{m}$, and $100 \times 32 \mu\text{m}$, arranged in ascending order from the first row. In total, six different models were compared.

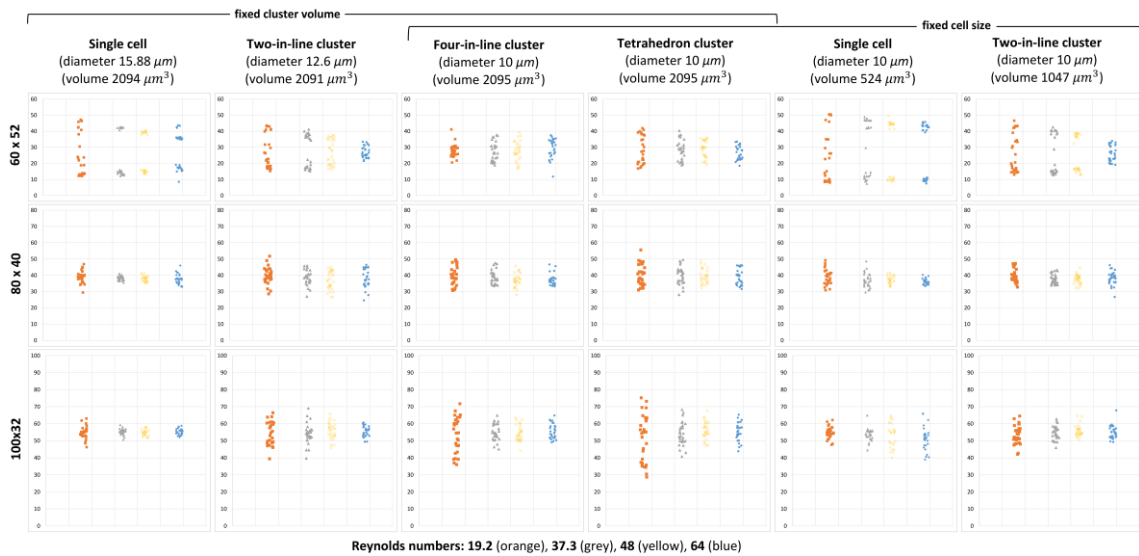


Figure 56: 72 Simulations after 21 passes, where each column represents different fluid velocity (Re = 19.2, 37.3, 48, 64)

A more detailed temporal overview of cluster passes can be observed individually, as depicted in Figure 57 for the 60×52 μm channel geometry and in Figure 58 and Figure 59 for other channel geometries. Notably, single cells and two-in-line clusters exhibited two distinct flows at certain velocities, particularly evident in the diagrams for the 60×52 μm cross-section. It's essential to highlight that when preserving a cell diameter of 10 μm , the single cell and two-in-line models created more pronounced dual flows compared to when preserving the volume.

The study provides an overview of the behaviour exhibited by various models, focusing on different volumes and diameters, particularly in relation to the Y-coordinate. Each diagram in the study involves the observation of 21 passes.

The investigation involved four distinct fluid velocities, organized in rows representing velocities from slowest to fastest, starting with the first row. This arrangement allows for the observation of six different models, all utilizing a channel geometry of 60×52 μm .

Dean Inertial Flows for Cell and Cluster Separation

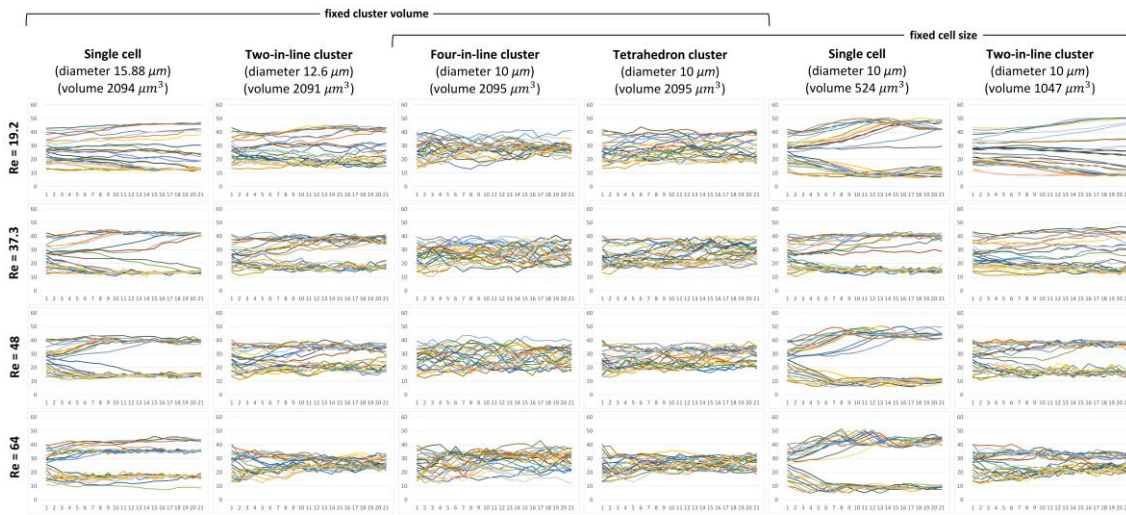


Figure 57: Behavior Analysis of Different Models in cross-section $60 \times 52 \mu\text{m}$ with 40 passes

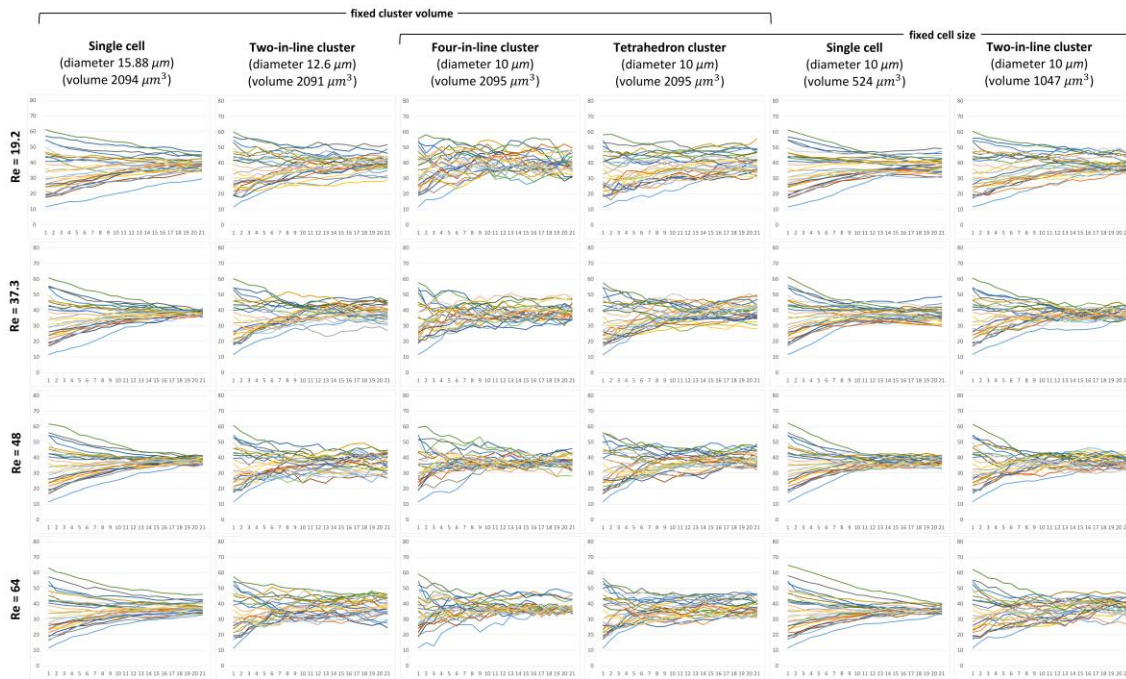


Figure 58: Behavior Analysis of Different Models in cross-section $80 \times 40 \mu\text{m}$ with 40 passes

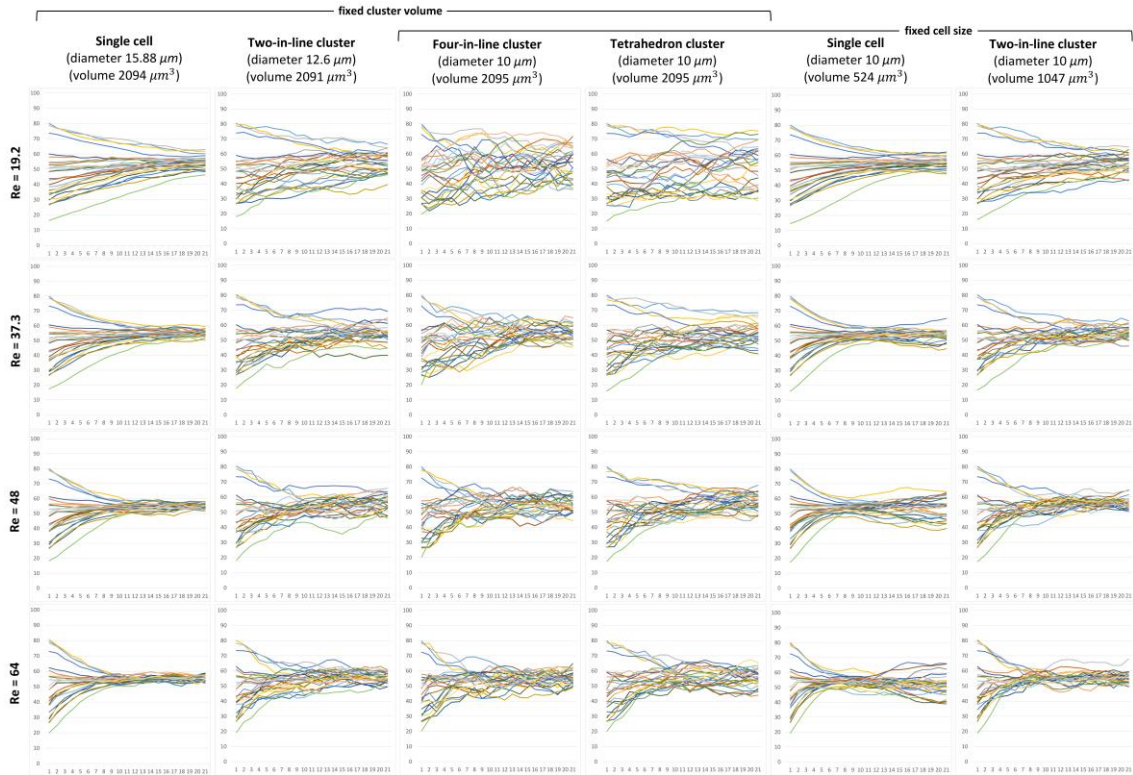


Figure 59: Behavior Analysis of Different Models in cross-section $100 \times 32 \mu\text{m}$ with 40 passes

Subsequently, the exploration extended to how objects moved within the Z dimension of the channel in relation to its Y dimension. Two distinct flows were not limited to a single dimension. For the $60 \times 52 \mu\text{m}$ channel geometry, the most variable results were obtained. Individual single cells mimicked tracer behaviour, concentrating at four distinct locations, as seen in Figure 60 for a $10 \mu\text{m}$ cell diameter.

The diagrams revealed that increasing the cell diameter or the number of cells in a cluster led to objects once again concentrating in the centre of the channel. This behaviour correlated with the findings from the previous study on the Y dimension.

Examining the $80 \times 40 \mu\text{m}$ channel geometry in Figure 61 with a narrower width resulted in objects concentrating in only two positions for individual single cells and at the centre for clusters. Finally, the $100 \times 32 \mu\text{m}$ geometry in Figure 62 with the narrowest channel exhibited a uniform concentration of objects at or close to the centre without significant differentiation. It's important to note that as fluid velocity increases, cells have a greater tendency to accumulate in the centre.

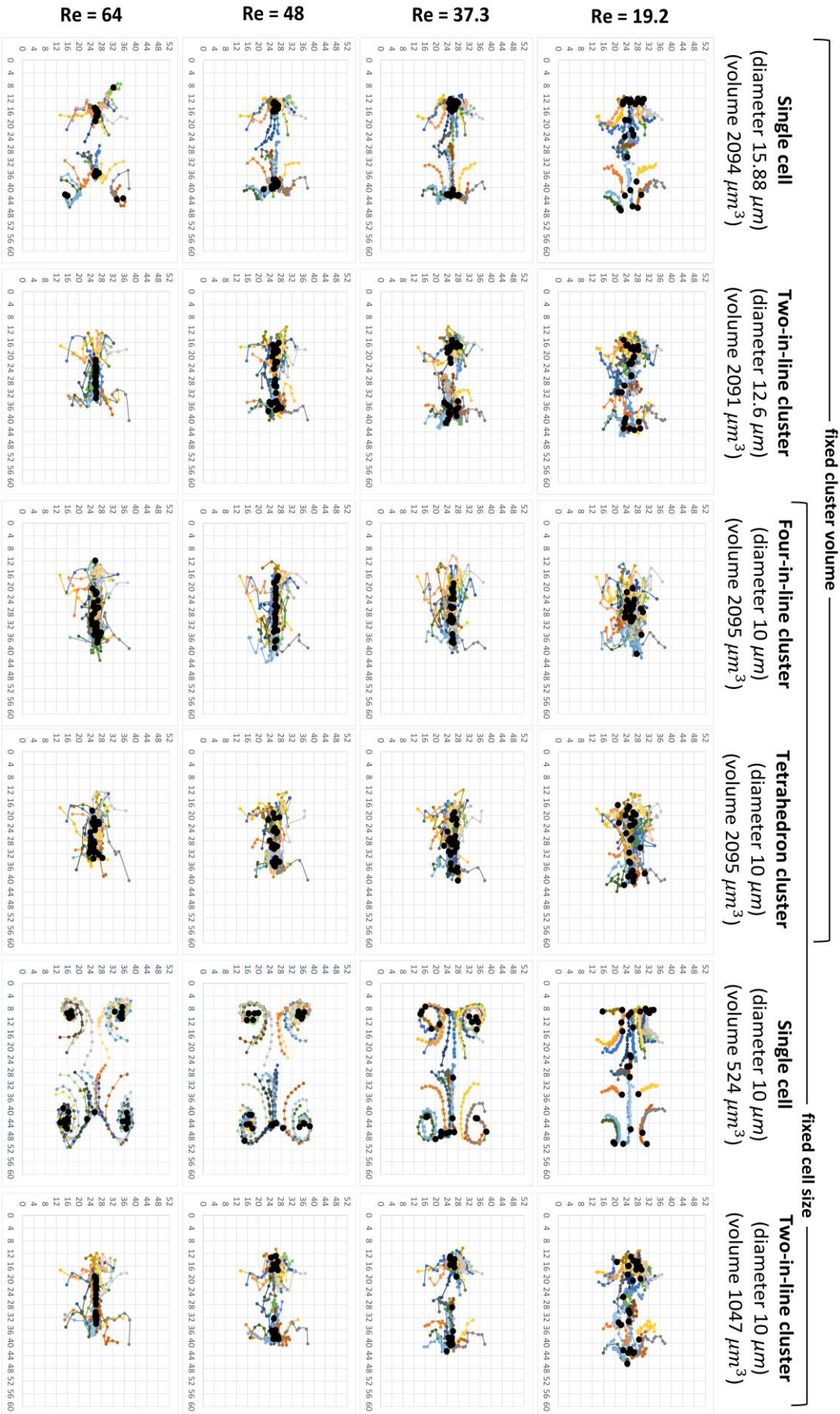


Figure 60: Particle Dynamics in Fluid Flow: Varied Models in a cross-section $60 \times 52 \mu\text{m}$

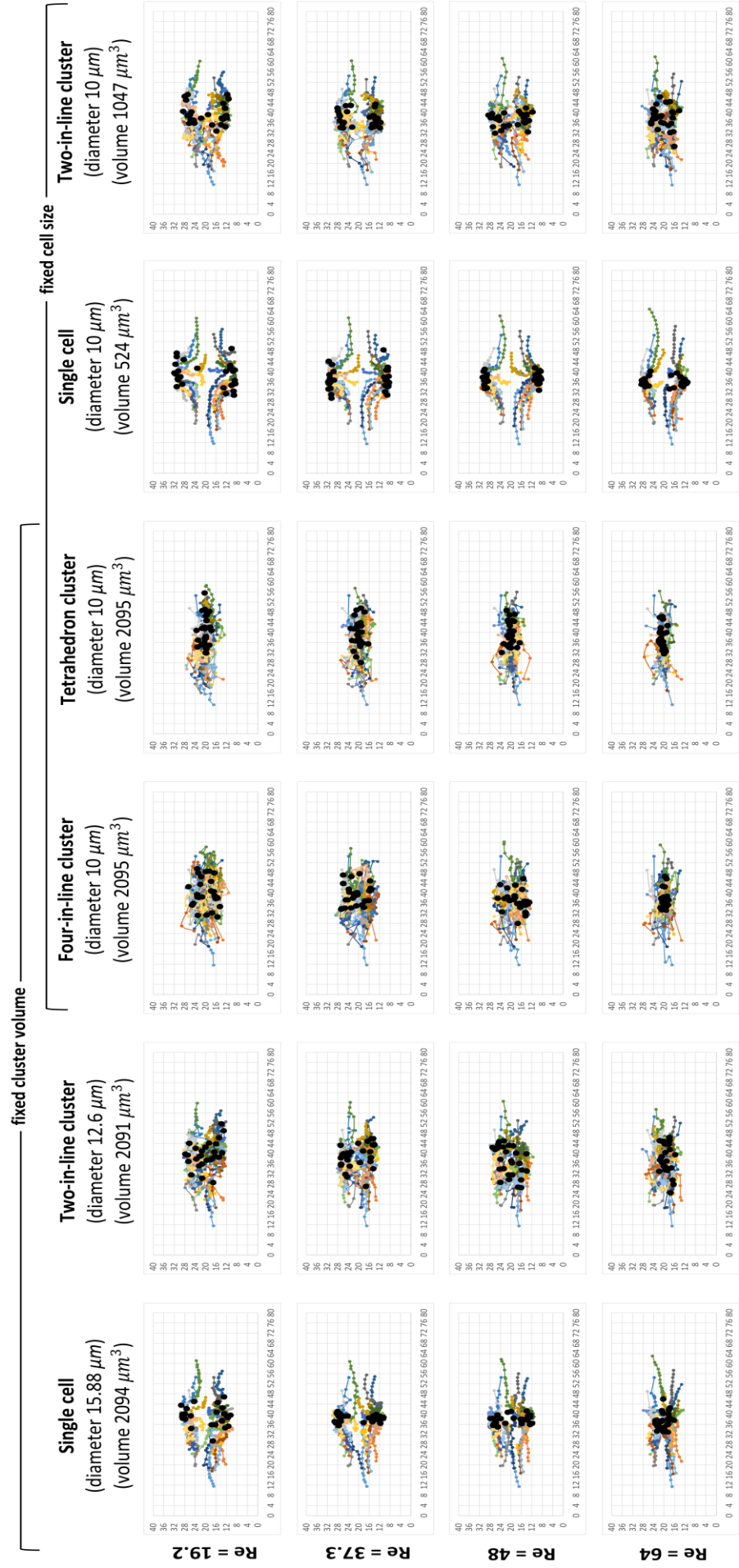


Figure 61: Particle Dynamics in Fluid Flow: Varied Models in a cross-section $80 \times 40 \mu\text{m}$

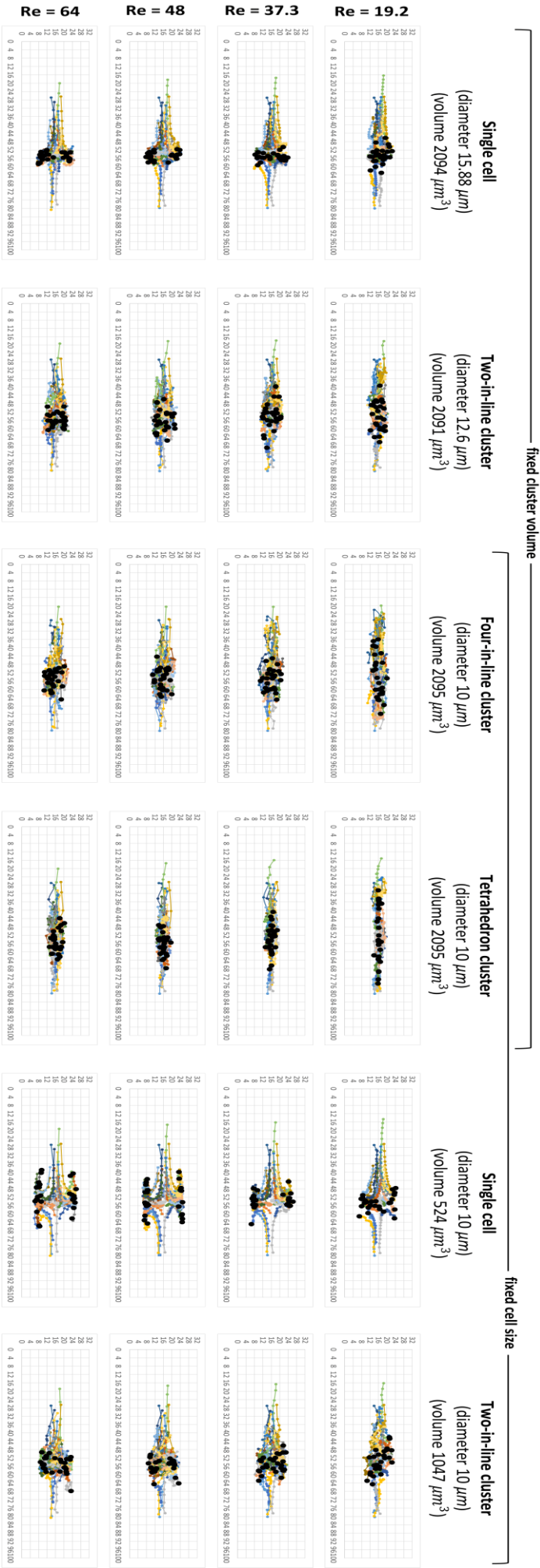


Figure 62: Particle Dynamics in Fluid Flow: Varied Models in a cross-section 100x32 μm

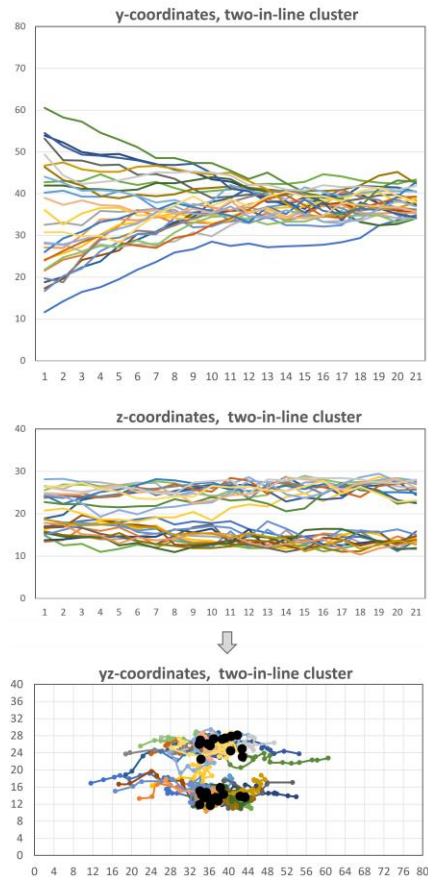


Figure 63: Comparative Analysis of Three Diagrams for a cross-section $80 \times 40 \mu\text{m}$

In the investigation of an $80 \times 40 \mu\text{m}$ geometric configuration at a Reynolds number (Re) of 37.3, three graphical representations are compared. Each diagram encompasses 21 iterations. Analysing the diagrams sequentially, the first two are scrutinized independently with respect to their evolution along the Y-coordinate and Z-coordinate axes. The third and final diagram illustrates the correlation between the Y-coordinate and the Z-coordinate.

Distinguishing disparities among all diagram types is evident in Figure 63. Specifically, the Y-coordinate, though extensive, lacks discernible indications of cluster division into two streams. Conversely, the associated Z-coordinate graph discloses a subtle separation along the Z-axis, notwithstanding its more confined spatial extent. The outcomes of the cluster analysis can be succinctly encapsulated in the subsequent four points:

- I. The preponderance of clusters tends to aggregate towards the central region of the Y-coordinate, except for single-cell and double-cell clusters, which only attempted to configure two streams only in the $60 \times 52 \mu\text{m}$ cross-section.

- II. As fluid velocity escalates, clusters exhibit an increased tendency to concentrate in the central regions of both the Y and Z-coordinates, barring the single-cell cluster with a $10\mu\text{m}$ diameter.
- III. Clusters and single cells with larger diameters, as explained in previous sections, are unable to induce Dean's vortices because their dimensions are sufficiently large relative to the channel size.
- IV. Four-cell clusters (four-in-line and tetrahedron clusters) cannot be distinguished from the data in this quantitative analysis. In all figures, the columns of the graphs for both types of four-cell clusters are very similar. In summary, both categories of clusters show very similar behaviour.

This overview summarises the behaviour of different models in relation to different volumes and diameters, specifically in relation to the Y and Z coordinates. The black dots indicate particle positions after 21 passes through the repeating S-section. The analysis includes four different fluid velocities, with each row describing a velocity from slowest to fastest, starting with the initial row. Consequently, six distinct models can be observed employing a channel geometry of $60\times 52\mu\text{m}$.

5.5.2 Qualitative analysis of flow patterns

Closer examination of the cell clusters revealed an interesting observation. Specifically, the four-cell cluster initially positioned itself close to the visualisation slice and almost parallel to the flow, with a slight random tilt. However, after several passes, its orientation along the X-axis underwent a transition to align parallel to the Y-axis. This new orientation remained stable for the remainder of the simulation. This behaviour is illustrated in Figure 64, where the cluster enters the first S-shaped section with an X-axis orientation, reorients itself to align with the Y-axis during two curves, and subsequently maintains this new orientation.

In contrast, the tetrahedron cluster showed a distinct behaviour. When the cluster was tracked through three S-sections, it was observed that the cluster maintained its original orientation without rotating. Instead, the cluster exhibited a slight oscillating tilt, oscillating three times within the three S-sections. This behaviour is also depicted in Figure 64 at the bottom.

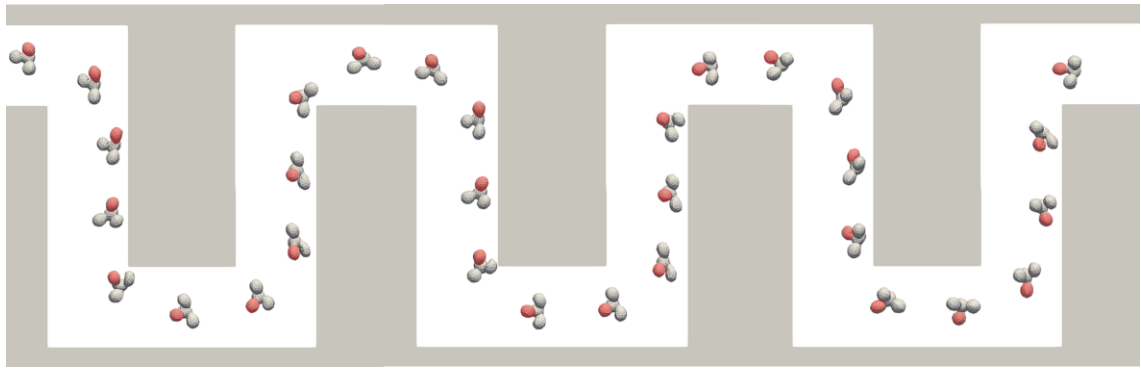


Figure 64: Cluster Motion in High Reynolds Microfluidic Channels

The standard movement patterns of a four-in-line cluster (depicted at the top) and a tetrahedron cluster (depicted at the bottom) within a $60 \times 52 \mu\text{m}$ geometry were observed under the highest Reynolds number (Re) conditions over three passes through the S-shaped channel. For clarity in visualizing rotations, one cell from each cluster is highlighted.

5.6 Inertial focusing and separation of clusters in using larger geometry

The concentration of particles approximately 60% from the tube centreline in straight channels is the result of a dynamic equilibrium between inertial shear gradient buoyancy forces pushing the particles towards the wall and wall repulsion forces generated by increased pressure between the particles and the channel wall. [46]. Changing the channel cross-section or introducing curvature through serpentine or spiral geometries can alter the distribution and positions of lateral equilibria, potentially accelerating the lateral focusing of particles [47].

The forces that govern this behaviour include three main components: the buoyancy forces due to wall interaction, the shear gradient buoyancy forces and the secondary flow induced Dean drag forces. These mechanisms together form a complex system where three different principles interact, all dependent on particle size, channel characteristics, fluid velocity and particle or cell elasticity. Computational modelling serves as a tool to analyse the effects under specific parameters and to evaluate the sorting potential of different suspensions.

In this investigation, we used two different geometries with dimensions of $160 \times 80 \mu\text{m}$ and $200 \times 64 \mu\text{m}$. In particular, we introduced rounded edges into the model, the first time such features have been incorporated to better mimic the curvature observed in

blood vessels in the human body. This departure from the geometries used in the study by [20] was intentional, given that the cells and subsequent cell clusters in our study were approximately twice as large. Consequently, the larger geometries were chosen to provide sufficient space for cell clusters to exhibit greater freedom to settle within the flow.

5.6.1 Microfluidic channel geometry

In the study by [20], a channel geometry with sharp edges was utilized. In our current work, we enhanced the model by introducing rounded edges, resulting in a smoother flow of the fluid, as depicted in Figure 65. To manage computational complexity, given the periodicity of the channel, we modelled only two S-sections with periodic boundaries at the inflow and outflow.



Figure 65: Separation of cells in repeating curved channel

Due to substantial computational demands, our model incorporates only a curved section in the shape of an "S," which is periodically repeated until the clusters stabilize in the flow. The conceptual illustration in Figure 66 outlines the approach: particles or clusters, initially seeded randomly near the observation line, flow through one S-section towards a specific re-seeding line.

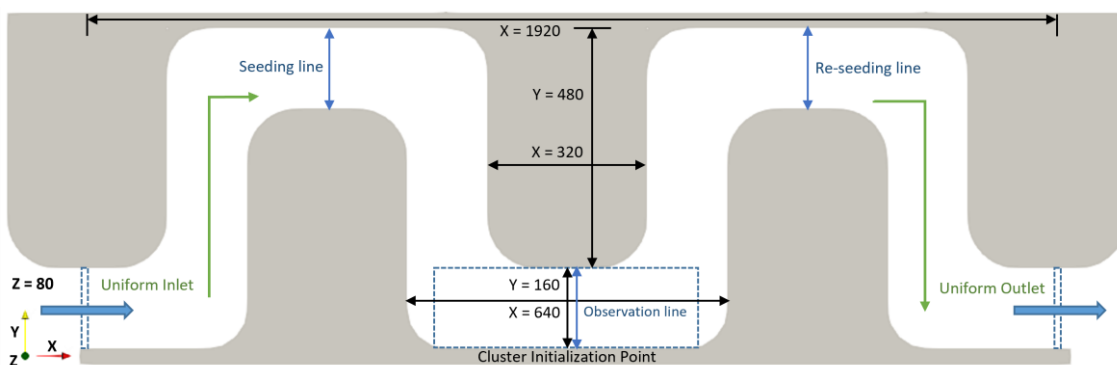


Figure 66: Detailed description of cross-section $160 \times 80 \mu m$

They are then seeded longitudinally back to the seed line by changing the X coordinates while maintaining the Y and Z coordinates. This method allows simulations to

be performed without creating an entire channel of 40 or 80 repeating S-sections, while maintaining the cluster velocity in the fluid after transfer.

In addition to the seeding and reseeded lines, an observation line in the centre of the channel is considered. When a cluster passes through this line, its centre coordinates are recorded in a file. The result for each cluster is represented by its trajectory in a graph showing where the cluster has stabilised.

When experimenting with different cross section sizes, it was observed that clusters of cells need enough space to flow along the walls rather than in the centre. For example, the $80 \times 40 \mu\text{m}$ cross section used in the [20] is considered too narrow for clusters to move away from the centre. These preliminary tests guided the selection of two different channel sizes, with detailed dimensions provided in Figure 66 for the cross-section $160 \times 80 \mu\text{m}$ and Figure 67 for the cross-section $200 \times 64 \mu\text{m}$, with all lengths described in micrometres.

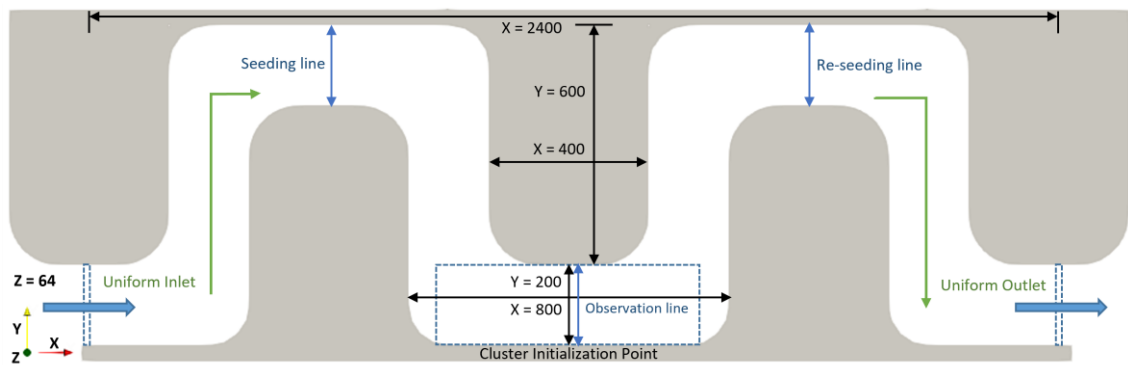


Figure 67: Detailed description of cross-section $200 \times 64 \mu\text{m}$

5.6.2 Fluid set-up

The enforcement of uniform boundary conditions at the inlet and outlet is essential to determine the average velocity within the channel, a parameter directly related to the volumetric flow rate. In the PyOIF framework, this is achieved by implementing a specialised velocity boundary with predefined constant values for the velocity field at the boundary points. The values of the inlet conditions and the corresponding Reynolds numbers are given in Table 11.

Table 11: Fluid velocity parameters

Reynolds number [-]	19.2	37.3	48	64
Average velocity [m/s]	0.18	0.35	0.45	0.6

To encompass a diverse set of conditions, we explore four distinct average velocities within the channel, ranging up to $0.6m/s$, allowing the Reynolds number to vary up to 64.

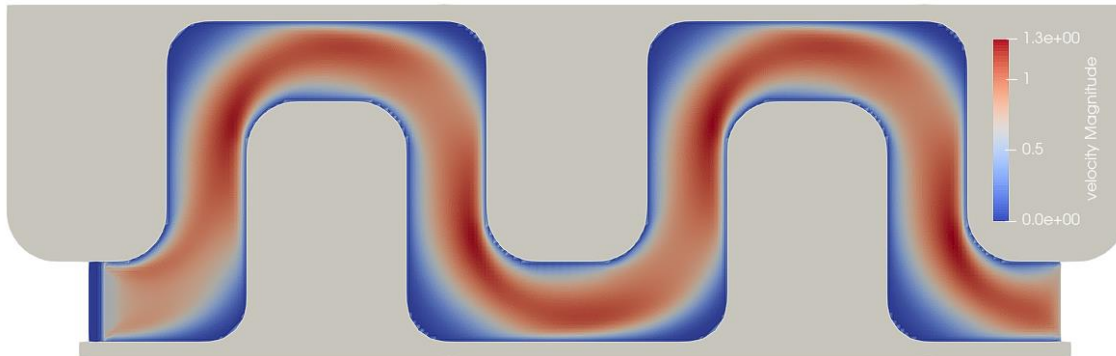


Figure 68: The fluid flowing in the channel at the Reynolds number of 64

A visual representation of the fluid flow throughout the simulation is depicted in Figure 68. Colour saturation reflects fluid velocity, with more saturated red indicating higher velocity and areas of deep blue indicating almost zero fluid velocity. Flow direction is from left to right.

5.6.3 Cell and cluster models

Like the red blood cell membrane model, which consists of a triangular mesh, the cluster model is constructed using a tetrahedral mesh. Recognising the presence of stiffer cancer clusters, we reinforced the interior of the cell by introducing additional edges to form a complete covering of tetrahedrons. This reinforcement aims to limit excessive deformation caused by the high fluid velocity in the simulation. The edges of the tetrahedrons are modelled as springs, each with a specific relaxed length and stiffness. Higher values of edge stiffness were used to achieve stiffer cells or clusters. Figure 69 illustrates the interiors of a single cell and a cluster, respectively.

A spherical shape was chosen to represent cancer cells as it closely approximates the morphology of most real cancer cell types in the body. The length of the tetrahedral edges was determined primarily by the size of the object, while keeping the number of points in the tetrahedral mesh constant.

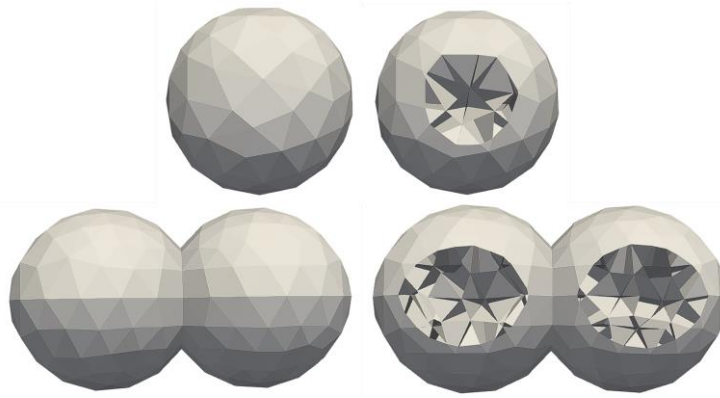


Figure 69: Cluster models and their cuts

Considering the actual sizes of cancer cell clusters, we identified three basic sizes for a single cell cluster and three for a cluster of two cells. On closer inspection, in one scenario the size of a single cell is even equivalent to two cells placed side by side. A visual representation comparing the sizes of clusters containing one or two cells is provided in Figure 70.

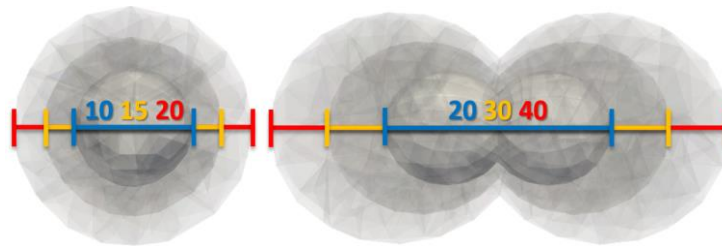


Figure 70: Sizes of cell and cluster models

The simulation of cell adhesion within a cluster can be approached in two different ways. One method is to use an attractive-repulsive Lennard-Jones or Morse-type interaction, where two separate cells are attracted when they are far apart and repelled when they are too close together. This approach allows the cells to slide past each other, and at high fluid velocities it can cause them to separate. However, at the fluid velocities we use, this method often results in the separation of cells, making it unsuitable for our purpose.

An alternative approach to connecting cells within a cluster is through a strong junction that prevents the cells from sliding over each other, essentially fixing the junction. To simulate this behaviour, we chose the second method, connecting cells through a common membrane. In this case, the entire cluster functions as one cohesive object. As depicted in Figure 70 on the right, the cluster contains two connected cells.

For a more in-depth understanding of these methods employed to simulate cell adhesion in a cluster, additional details can be found in the article by [33].

5.7 Results using larger geometry

In this section, we will explore the outcomes of simulations conducted in an S-shaped curved channel, focusing on a fundamental cluster type consisting of two cells, hereafter referred to as the "two-in-line" cluster. Technically, we also treat a single cell as a cluster of cells, referred to as CTC. For each cluster type, we distinguish three different sizes concerning the diameter. For the two-in-line cluster, diameters of 20, 30, and 40 μm were utilized, indicating that one cell in the two-in-line cluster had a diameter of 10, 15, and 20 μm . For the single-cell cluster, we aimed to approximate its largest size to that of the smallest two-in-line cluster, hence using the same diameters of 10, 15, and 20 μm . The cluster sizes were selected based on the article by [2].

In addition to the cluster type and size, the elasticity of the cell was incorporated into the simulations. Clusters were categorized as more and less elastic under the labels "solid" and "solid-elastic". Solid clusters represented the stiffest cells with minimal deformation possibilities during flow in the channels, while elastic ones had the ability to deform. It is essential to note that both types of clusters had an internal fill, and we will discuss one crucial and exclusively used elastic parameter called k_s , representing the edge stiffness. A comparison between an solid-elastic cluster with $k_s = 0.5$ and a solid cluster with $k_s = 1.0$ is illustrated in Figure 71, where the deformation at low shear rates is depicted in top row and at high shear rates in bottom row. The top row depicts clusters near the channel centre with low shear rates, implying minimal deformation. The second row depicts clusters positioned near the wall with high shear rates, leading to significant deformation in the more elastic cluster while the solid one remains relatively rigid. These simulations in Figure 71 were conducted at $\text{Re} = 64$.

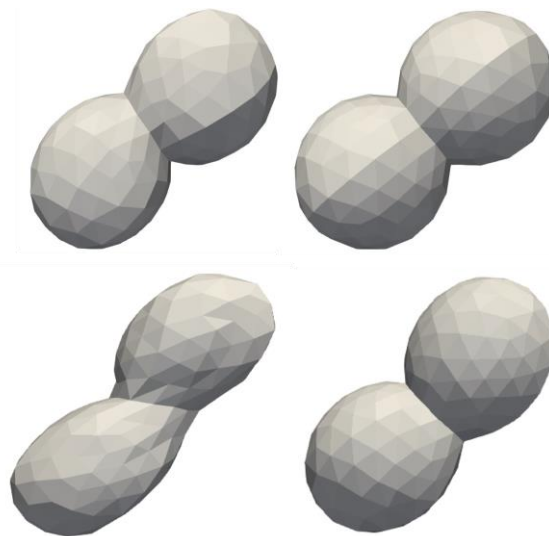


Figure 71: Deformations of a two-in-line cluster

As previously mentioned, simulations were conducted with four fluid velocities corresponding to four values of Reynolds number, as indicated in Table 11. It is important to note that we employed two different channel sizes with cross-sections of $160 \times 80 \mu\text{m}$ and $200 \times 64 \mu\text{m}$.

The initial seeding line for generating cluster positions is outlined in Figure 66 and Figure 67. Different random cluster positions were generated for each geometry. In addition, the initial rotation of the clusters was randomised for each geometry, as there was no clear explanation as to whether the initial rotation significantly affected the simulation results. As these are simple clusters consisting of one or two cells, no significant emphasis was placed on this aspect.

5.7.1 Quantitative analysis of flow patterns

From a quantitative perspective, our analysis focused on categorising the data obtained from the simulations into five key parts for better clarity: channel geometry, fluid velocity, cluster type, cluster size and cluster elasticity, in that order. The main focus was on comparing the separation of different clusters, with inertial flow, in particular the Dean effect, playing a central role.

To provide a general overview, each simulation contained 28 clusters of cells. The number of clusters was chosen randomly due to the computational power of the simulations. As more cells are used, the computational effort increases either linearly or exponentially, depending on the number of different interactions used. The simulation time increased until each cluster crossed the observation line 40 times. However, it is noteworthy that especially at the highest fluid velocity ($Re = 64$) and channel size of $160 \times 80 \mu\text{m}$ with CTCs, it was observed that they did not have sufficient time to stabilize within 40 passes. Therefore, the number of passes was increased to 80 to allow for more effective stabilization within the flow. A significant difference between 40 and 80 passes is evident in Figure 72, Figure 73 and Figure 74 for comparison.

Dean Inertial Flows for Cell and Cluster Separation

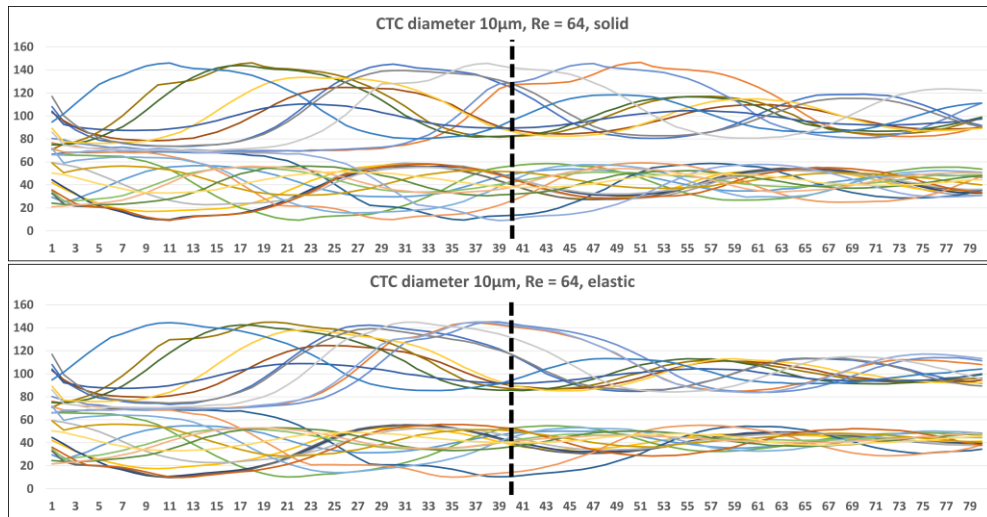


Figure 72: Quantitative Analysis of Cluster Dynamics CTC with 10µm and 80 passes

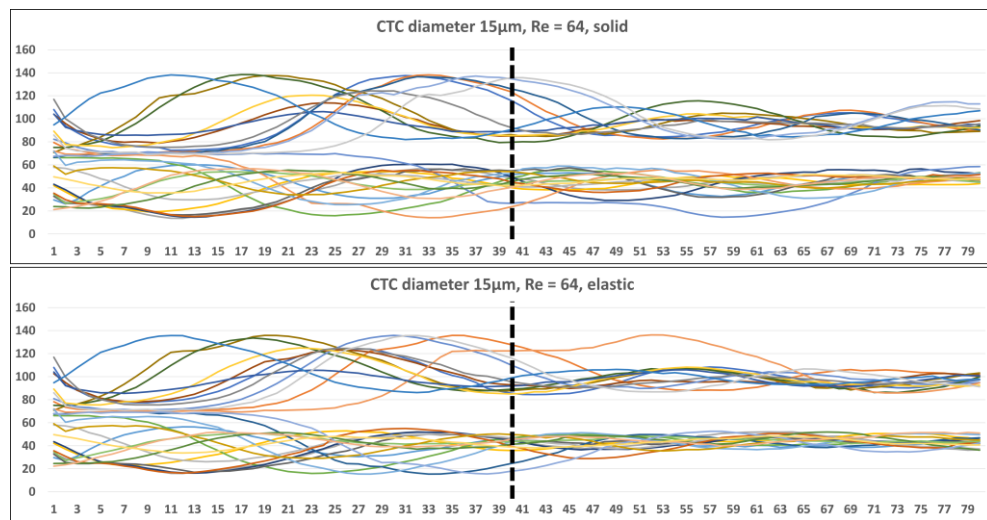


Figure 73: Quantitative Analysis of Cluster Dynamics CTC with 15µm and 80 passes

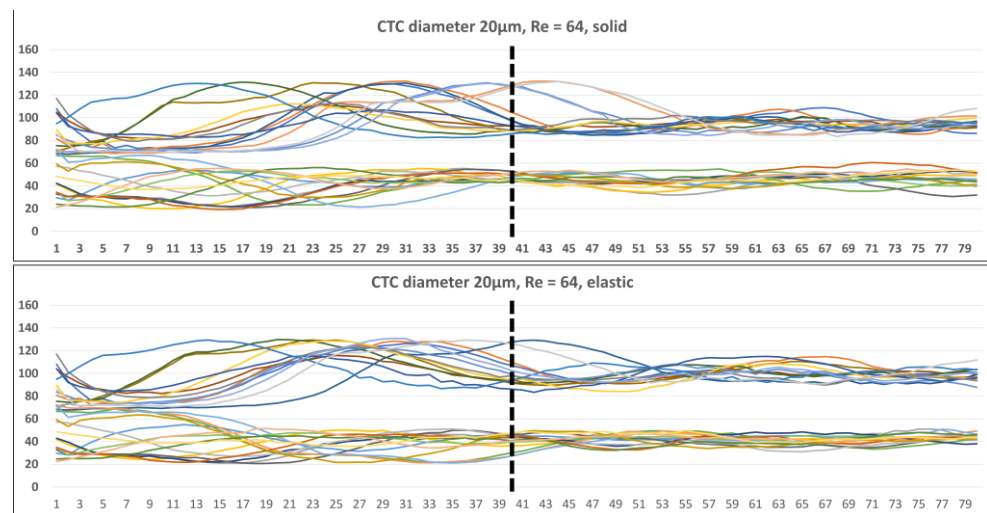


Figure 74: Quantitative Analysis of Cluster Dynamics CTC with 20µm and 80 passes

For all subsequent comparisons in graph form, results from 80 passes were used. Figure 72, Figure 73 and Figure 74 serves as a key quantitative analysis tool, clearly demonstrating that, in some cases, clusters can linger near the channel walls, creating space in the middle of the channel for other clusters that can be separated from the lateral clusters.

We can see more results in Figure 75 with each graph containing precisely 12 simulations. Each graph is structured into 4 columns, corresponding to the 4 Reynolds number values listed in Table 11, arranged from the smallest to the largest from left to right. Within each column, the results are derived from three simulations, each with a different cluster size. The legends on the graphs indicate that blue squares represent the smallest clusters, yellow diamonds represent medium-sized clusters, and red triangles represent the largest clusters.

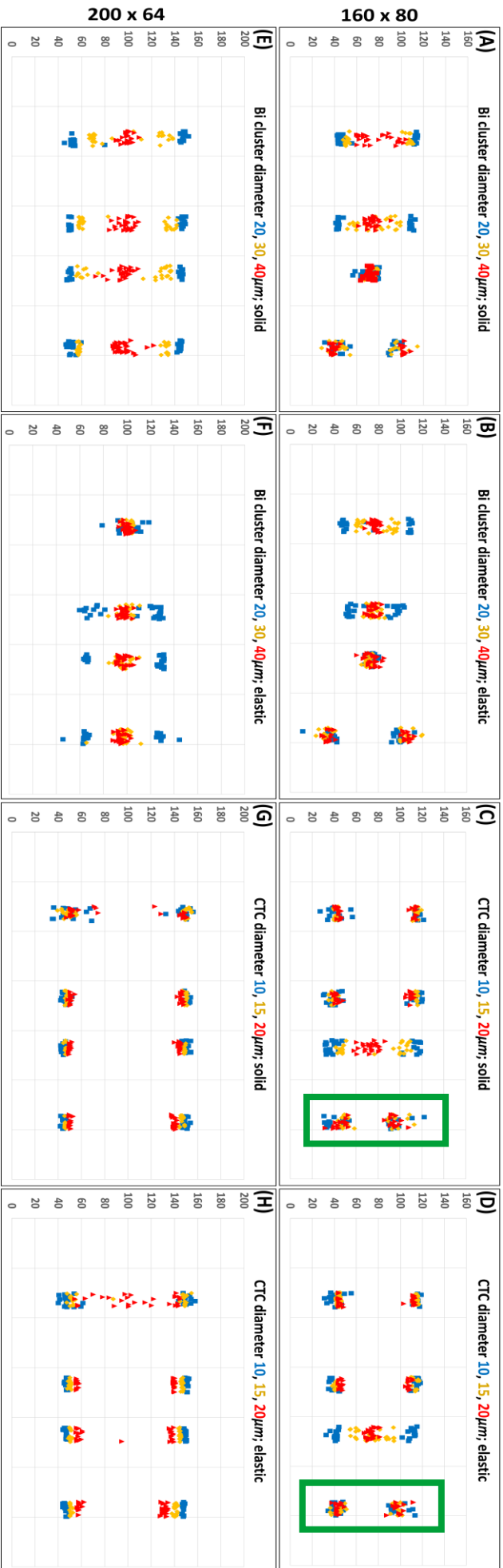


Figure 75: 96 Simulations after 40 passes and 80 passes (green rectangles), where each column represents different fluid

velocity ($Re = 19.2, 37.3, 48, 64$)

These graphs are a condensed transformation of the original 8 graphs to provide a more visually concise representation. Data for the graphs were extracted only from the last passage of all cells in the simulation. All graphs show the locations where cell clusters achieved stabilisation. The first row of graphs (A-D) illustrates the last passage of cells from channels with a cross-section of $160 \times 80 \mu\text{m}$, while the second row (E-H) pertains to channels with a cross-section of $200 \times 64 \mu\text{m}$.

Graphs (A), (B), (E) and (F) show the stabilisation of two-in-line clusters, while graphs (C), (D), (G) and (H) focus on CTCs (circulating tumour cells). Regarding the elasticity of clusters, graphs (A), (C), (E) and (G) show solid clusters, while graphs (B), (D), (F) and (H) show elastic clusters.

Analysis of CTCs

Upon initial observation, CTCs in graphs (C), (D), (G), and (H) exhibit a tendency to linger predominantly along the sides of the channel. The notable distinction arises in the case of solid and elastic CTCs in graphs (C) and (D) for the channel geometry of $160 \times 80 \mu\text{m}$, fluid velocity $\text{Re} = 64$, and a diameter of $20 \mu\text{m}$, where they tend to linger more toward the middle of the channel.

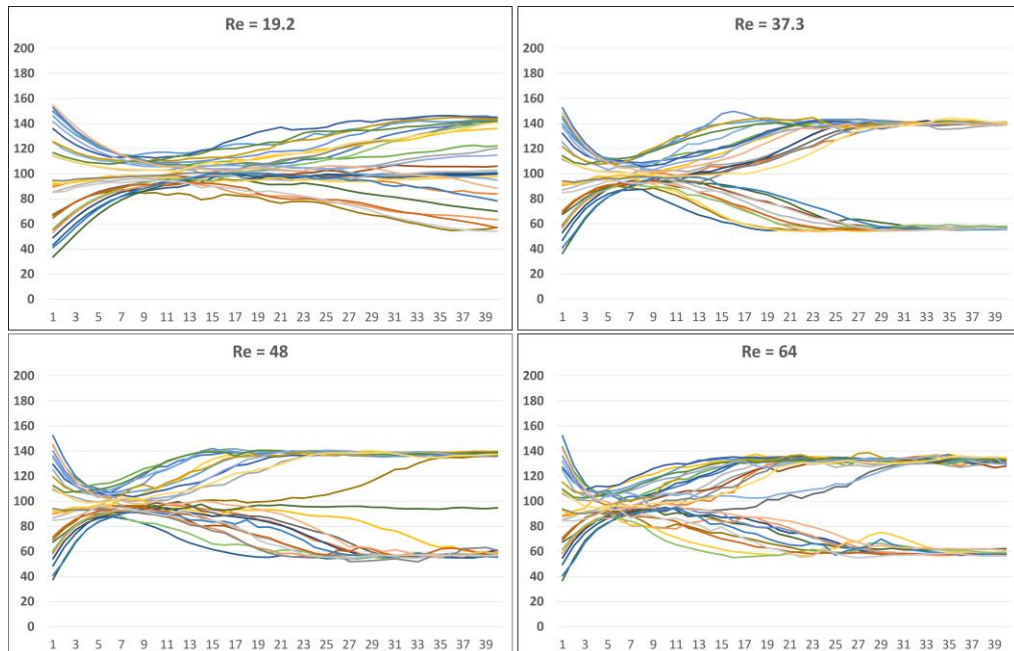


Figure 76: Settling Dynamics of Elastic CTCs in a $200 \times 64 \mu\text{m}$ S-Channel Across Varied Fluid Velocities with 40 passes

This phenomenon suggests a difference in behaviour compared to the smallest CTCs with a diameter of $10\mu m$. It is important to note that in graph (H), the largest CTCs at the slowest speed are distributed across the entire width of the channel. This result can be attributed to the limited number of passes, indicating that the cells have not had sufficient time to settle. For a more complete understanding, the dynamic changes in settling can be viewed in Figure 76.

Analysis of two-in-line clusters

In the context of two-in-line clusters, their behaviour in the flow shows a more complex pattern. The trend for the largest clusters is consistent with that of single cell clusters, concentrating in the centre of the channel. Only at the highest velocity, $Re = 64$, and a geometry of $160 \times 80\mu m$, are there cases where they concentrate at the channel edges, as shown in graphs (A) and (B) in the last columns marked in red. Conversely, the smallest two-in-line clusters, marked in blue, tended to settle regularly at the channel edges, with specific exceptions observed in graphs (B) and (C) at $Re = 48$ and graph (F) at $Re = 19.2$.

Medium sized two-in-line clusters, marked in yellow, generally exhibited similar behaviour to two-in-line clusters, with isolated cases noted in graphs (A) and (E) where the settling level coincided with the smallest two-in-line clusters. From the analysis it can be concluded that there is a possibility of differentiating two-in-line clusters based on their size, as shown in the graph (E) at all fluid velocities or at specific fluid velocities in graphs (A), (B) or (F).

An interesting aspect is the introduction of elasticity as a factor for two-in-line clusters. Notably, clusters with diameters of $20\mu m$ and $30\mu m$, exhibiting different elasticity, could potentially be distinguished. This phenomenon can be seen, for example, by comparing graphs (E) and (F) at the lowest velocity $Re = 19.2$ for the smallest clusters and at all velocities for medium-sized clusters. Here, solid clusters are concentrated at the sides of the channel, while elastic clusters occupy its centre.

Comparison between CTC and two-in-line cluster

In comparing the same geometries but different clusters, specifically CTCs and two-in-line clusters, it is evident that separation is achievable under specific conditions. Focusing on the first row of graphs with the $160 \times 80\mu m$ geometry, the smallest two-in-line clusters with a diameter of $20\mu m$ in graphs (A) and (B) could be differentiated from CTCs in graphs (C)

and (D) with a diameter of $10\mu\text{m}$, particularly at a fluid velocity of $\text{Re} = 48$. This distinction arises because CTCs tend to stabilize at the sides of the channel, while two-in-line clusters stabilize in the centre.

Similar separation possibilities are observed for medium-sized and the largest two-in-line clusters with diameters of 30 and $40\mu\text{m}$. However, the largest two-in-line clusters at a fluid velocity of $\text{Re} = 37.3$ could potentially be separated from CTCs of any size. The same holds true for $\text{Re} = 19.2$ and elastic two-in-line clusters. The geometry of $200 \times 64\mu\text{m}$, offering more space for cell stabilization at the channel sides due to its wider width, provides a clearer separation possibility.

For the smallest elastic two-in-line cluster in graph (F), there is a possibility of separation at the slowest fluid velocity of $\text{Re} = 19.2$ from CTCs of any size in graphs (G) and (H). In this scenario, the separation potential for elastic CTCs would depend on the number of passes. The same principle applies when considering medium-sized and elastic two-in-line clusters in graph (F), where separation is possible regardless of the chosen fluid velocity Re . However, the largest two-in-line clusters could probably be separated most effectively from CTCs of any size, as it is independent of both elasticity and fluid velocity.

5.7.2 Qualitative analysis of flow patterns

From a qualitative standpoint, we closely examined the flow dynamics of CTC and two-in-line clusters in the $160 \times 80\mu\text{m}$ channel. The movement of a single solid two-in-line cluster at the highest velocity is illustrated in Figure 77, capturing the cluster's motion through three consecutive S-sections. The recording commenced after approximately 20 passes, indicating a steady flow.



Figure 77: S-Channel Dynamics: Largest Solid Two-in-Line Cluster at High Velocity

At first glance, collisions with the wall can be seen on every upper right turn. In general, two-in-line clusters show no reason to rotate about their centre. However, during

the gentle shear flow generated by collisions and movement along the wall, the cluster tends to rotate around its own centre several times in succession. This rotation involves a change in the order of the cells, with the most pronounced rotations occurring in the first two upper turns, as the cluster is aligned longitudinally along the x-axis. In the third rotation, where the cluster is oriented width wise, this type of rotation does not occur. In this case, the cluster appears to rotate like a wheel.

It is important to highlight that collisions of CTCs and clusters with walls are of concern from a human health perspective. Further insights into these interactions can be found in the article [32].

5.8 Collaboration with MIT Research Group: Goals and Trade-offs

To date, our experiments have been based primarily on findings and insights from the relevant literature. However, following a fruitful collaboration with a research team from MIT in the United States, the opportunity arose to compare our findings on Dean flow and cell cluster separation with biological experiments. This collaboration not only allowed us to become familiar with the systems and technologies available at MIT for fabricating basic microfluidic devices, but also gave us access to a wide range of objects that can be subsequently integrated into a microfluidic device. These objects allow the controlled delivery of fluid at a constant rate, using the syringe principle. In addition, these objects can accurately replicate the behaviour of white blood cells or cancer cells in a flow.

As our software is based on a mathematical model, it is time consuming. This is due to the complexity and number of mathematical calculations required for each simulation. Conversely, the MIT research group faced challenges primarily related to the fabrication of microfluidic devices. The tools and technologies they use impose predefined minimum and maximum thresholds in each dimension. As a result, they had to compromise on the dimensions compared to our model.

It should be noted that in this case we initially abandoned classical cancer cell clusters in favour of a specialised type of cell cluster consisting of a single cell. This decision was driven by computational complexity and availability, as the implementation of such clusters proved to be simpler. After obtaining and comparing suitable results from both sides, our aim is to gradually move to more complex two-cell clusters.

5.8.1 Microfluidic channel geometry

To align simulations with biological experiments, we opted for three distinct geometries that, according to prior research, are deemed conducive to observing cell separation. A comprehensive depiction of these channels is provided in Figure 78, offering detailed descriptions.

In all three geometries ($160 \times 48 \mu\text{m}$, $200 \times 48 \mu\text{m}$, and $250 \times 48 \mu\text{m}$), adjustments were made to the height (Y-axis) and length (X-axis) of the channel. Given our focus solely on individual cancer cells of varying size and elasticity, height limitations that might apply to larger cell clusters are not a constraint for us.

As previously mentioned in Section 5.4.1, we are reseeded every cell at reseeded line to the seeding line, thus creating one uninterrupted flow. Our data were noted every pass of a cell at the observation line.

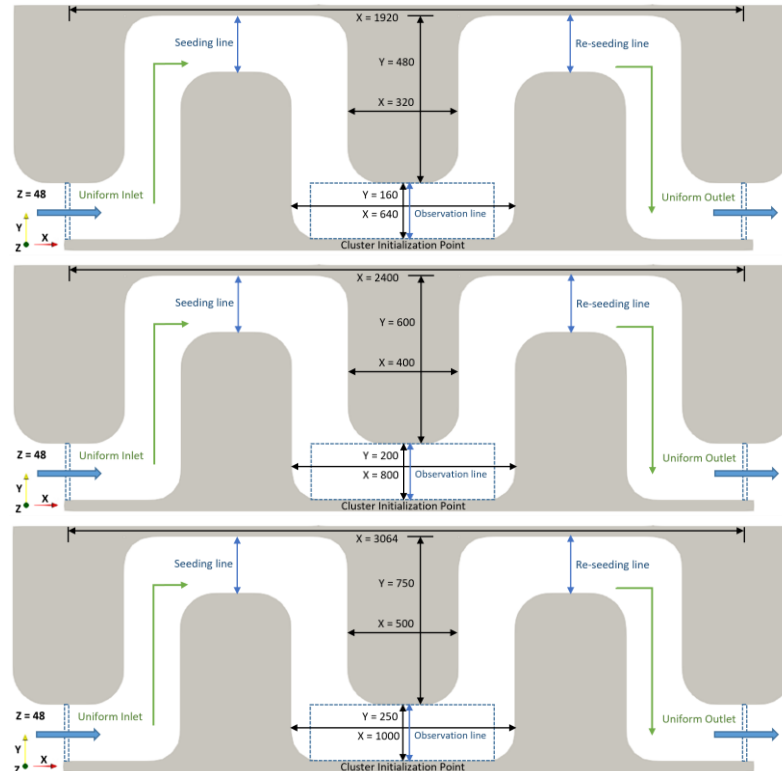


Figure 78: Detailed description of curved channels with cross-sections $160 \times 48 \mu\text{m}$, $200 \times 48 \mu\text{m}$ and $250 \times 48 \mu\text{m}$ from the top to the bottom

5.8.2 Fluid set-up

As depicted in Table 12, consistent volumetric flow rates were employed for intercomparison in the $160 \times 48 \mu\text{m}$ and $200 \times 48 \mu\text{m}$ cross-sections. In contrast, for the $250 \times 48 \mu\text{m}$ cross-section, the initial volumetric flow rate of 158.4 mL/min corresponds to

the slower rates observed elsewhere in the table, while the subsequent value of 799.2 mL/min stands out as the highest across the entire dataset. This cross-section serves as the basis for comparing our simulations with experiments conducted earlier by the MIT group.

Table 12: Fluid parameter in curved channels with different cross-sections

Cross-section [μm]	Average velocity [m/s]	Reynolds number [-]	Volumetric flow [mL/min]
160x48	0.346	53.17	0.166
160x48	0.692	102.2	0.319
160x48	1.038	153.3	0.478
160x48	1.384	204.4	0.638
200x48	0.277	42.89	0.160
200x48	0.554	85.78	0.319
200x48	0.831	128.67	0.479
200x48	1.108	171.56	0.638
250x48	0.22	35.44	0.158
250x48	1.11	178.79	0.799

Regarding the visual depiction of fluid flow within the channel, it is observed that with an increase in fluid velocity, there is a corresponding augmentation in the scale and range of colours, as exemplified in Figure 79. Nonetheless, the principle remains unchanged: areas exhibiting a deeper red hue signify higher fluid velocities. Consequently, the fluid attains its maximum velocity within the curves, approximately around 2.5 m/s .

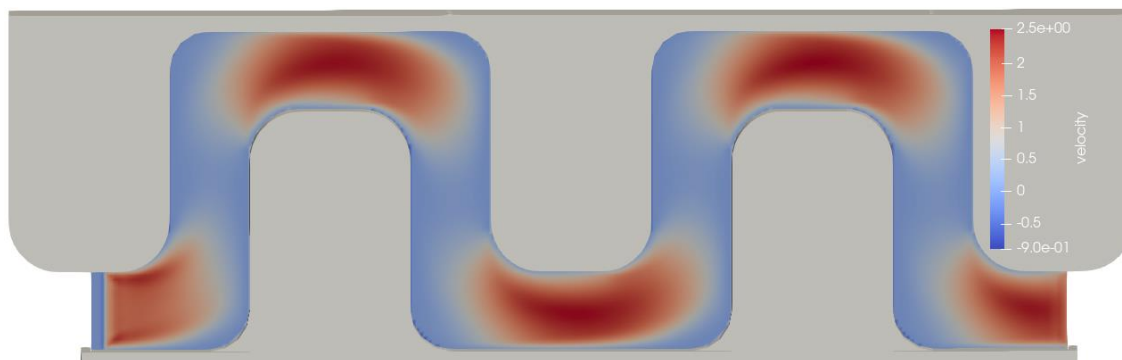


Figure 79: The fluid flowing in the channel at the Reynolds number of 171.56

5.8.3 Cell models

In this section, we delineate the cell models utilized and their respective parameters. Our primary objective was to approximate typical cancer cell sizes, hence we selected two diameters: $8\mu\text{m}$ and $15\mu\text{m}$, as illustrated in Figure 80.

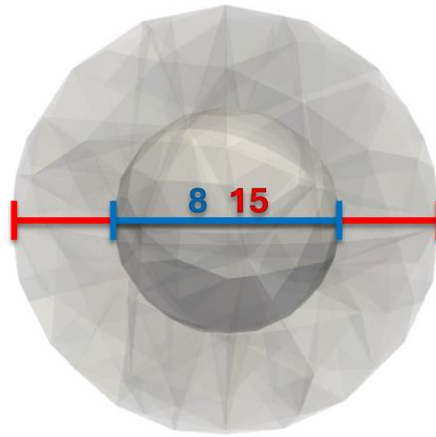


Figure 80: Sizes of cell models

As evident, the cell model bears resemblance in appearance and properties to the cell delineated in Section 5.6.3, with the sole discrepancy being the utilization of two distinct sizes differing from each other.

5.9 Results from collaboration with MIT Research group

The MIT research group has so far provided us with a few videos showing the final part of the branching after 8 S-section passes, showing the division of the objects into individual branches. In this instance, we examined a microfluidic channel possessing a cross-sectional area measuring $250 \times 48\mu\text{m}$.

Figure 81 comprises two sub-figures with $\text{Re} = 35.44$. In the left sub-figure, the positions of $8\mu\text{m}$ cells are depicted, where the fluid velocity remains minimal as the pressure from the syringe begins to exert. Conversely, the right sub-figure illustrates the cell arrangement at maximum achieved velocity. Comparison of these images reveals minimal disparity, indicating negligible cell settling under inertial flows and consequently an inability to facilitate separation in this scenario.

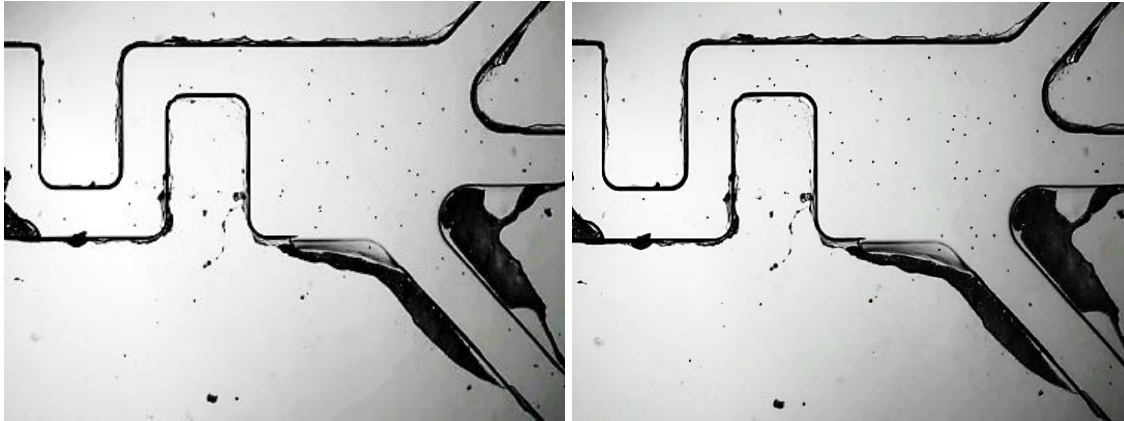


Figure 81: Cell positions at the beginning (left) and at the end (right) of the experiment using $Re = 35.44$

However, upon examining the Figure 82, a substantial contrast emerges between the initial and subsequent images, characterized by $Re = 178.79$. Here it is evident that cells settle along the wall in two distinct streams, directed towards either the upper or lower outlet, while the middle outlet is comparatively neglected. This observation provides an opportunity to exploit larger cells or clusters of cells, as suggested by previous simulations, which are more likely to settle towards the centre of the channel. Such an approach could allow the segregation of smaller cells from their larger counterparts.

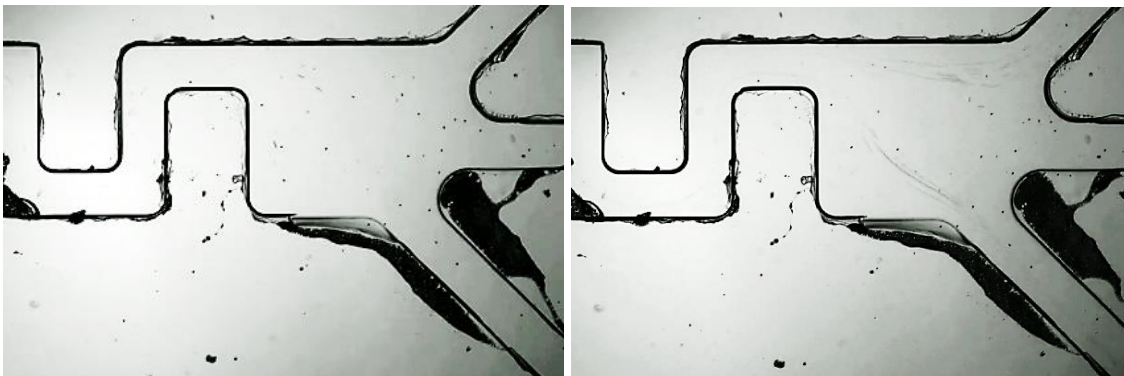


Figure 82: Cell positions at the beginning (left) and at the end (right) of the experiment using $Re = 178.79$

To assess the consistency between our experimental results and simulations, we set up the geometry replicating the microfluidic channel depicted in Figure 81 and Figure 82. The primary aim was to maintain uniformity in channel dimensions and fluid velocities across both scenarios. Specifically, the model retained a cross-sectional area measuring $250 \times 48 \mu m$, with corresponding fluid velocities of $0.22 m/s$ and $1.11 m/s$, respectively.

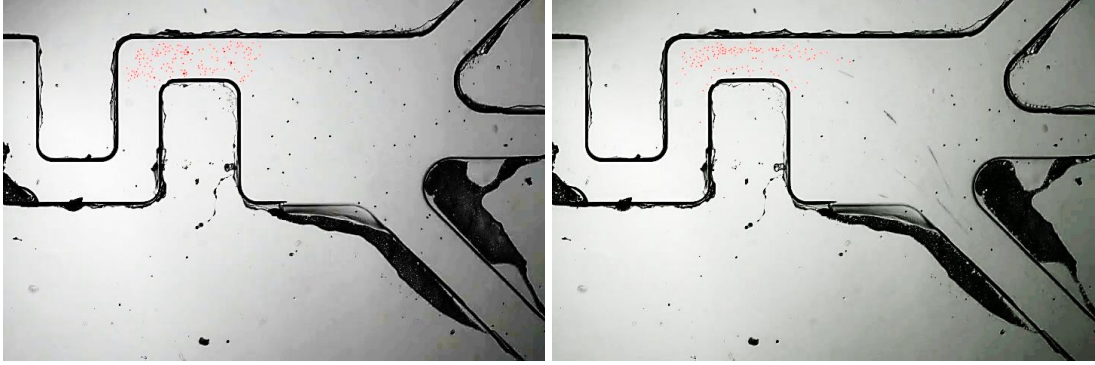


Figure 83: Comparison between positions taken after 8 S-section passes with $Re = 35.44$ (left) and $Re = 178.79$ (right)

To facilitate a comprehensive comparison between the results, we systematically tracked the positions of most of the cells marked with red dots on the terminal curve of the channel for both flow velocities, as shown in Figure 83. Therefore, a visual examination reveals that in the left image, cells are distributed across the entire width of the channel, indicating minimal room for segregation. Conversely, in the right image, cells tend to cluster near the walls, resulting in a significantly larger gap between clusters, and therefore a greater potential for separation.

5.9.1 Quantitative analysis of flow patterns

To facilitate a comparison between the data collected from the biological experiment and our simulation results, we transformed the red dots observed in Figure 83 into graphical representations. For both Reynolds numbers ($Re = 35.44$ and $Re = 178.79$), we randomly selected 40 recorded cell positions from the biological experiment and plotted them on the numerical Y-axis, corresponding to the channel width. The comparison between our simulation data (represented by blue dots) and the cell positions from the biological experiment (represented by orange dots) can be observed in Figure 84. On each graph, there are 40 orange dots and 40 blue dots.

Based on the observations from Figure 84, it is evident that our simulation outcomes closely align with the findings derived from biological experiments. At a Reynolds number (Re) of 35.44, the scattered distribution of cells across the channel width indicates the absence of significant separation potential. Conversely, at $Re = 178.79$, partial separation becomes feasible as cells tend to concentrate closer to the channel walls.

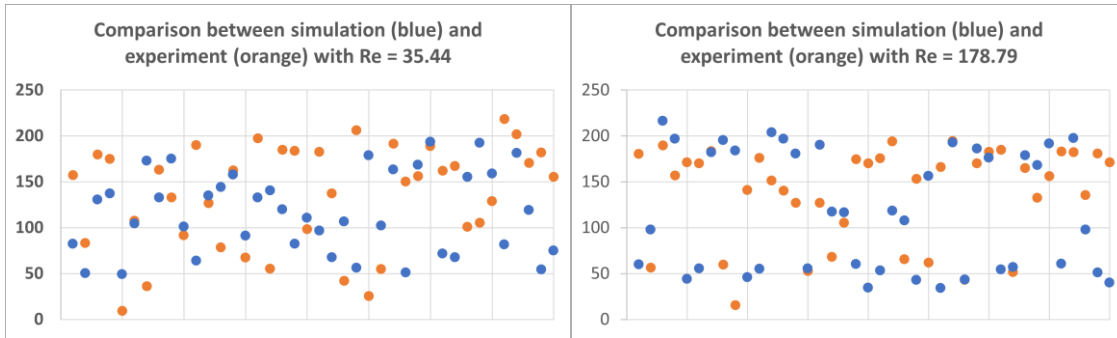


Figure 84: Comparisons between our simulations (blue) and MIT experiments (orange) after 8 S-section passes using $8\mu\text{m}$ solid CTCs

Given the match between our findings and those of the MIT group, we mutually decided to fabricate channels with cross-sections of $200 \times 48\mu\text{m}$ and $160 \times 48\mu\text{m}$. Table 12 outlines the respective fluid velocities corresponding to each geometry size, which we will interpret in terms of Reynolds number. In this context, we concurrently introduced cells of two different sizes: $8\mu\text{m}$ with solid properties and $15\mu\text{m}$ with solid-elastic properties. Twenty cells of each size were used. We adopted the same elasticity settings as in Section 5.7, albeit now involving single cells rather than simple two-cluster configurations.

The simulation results for the $200 \times 48\mu\text{m}$ cross-section are illustrated in Figure 85, while those for the $160 \times 48\mu\text{m}$ cross-section are depicted in Figure 86. In both figures, cell positions were recorded after 40 S-section passes, ensuring a steady cell flow. Each column in the graph represents a different fluid velocity, and consequently, a different Reynolds number, progressing from left to right. The first column corresponds to the lowest fluid velocity, while the fourth and last column represent the highest fluid velocity.

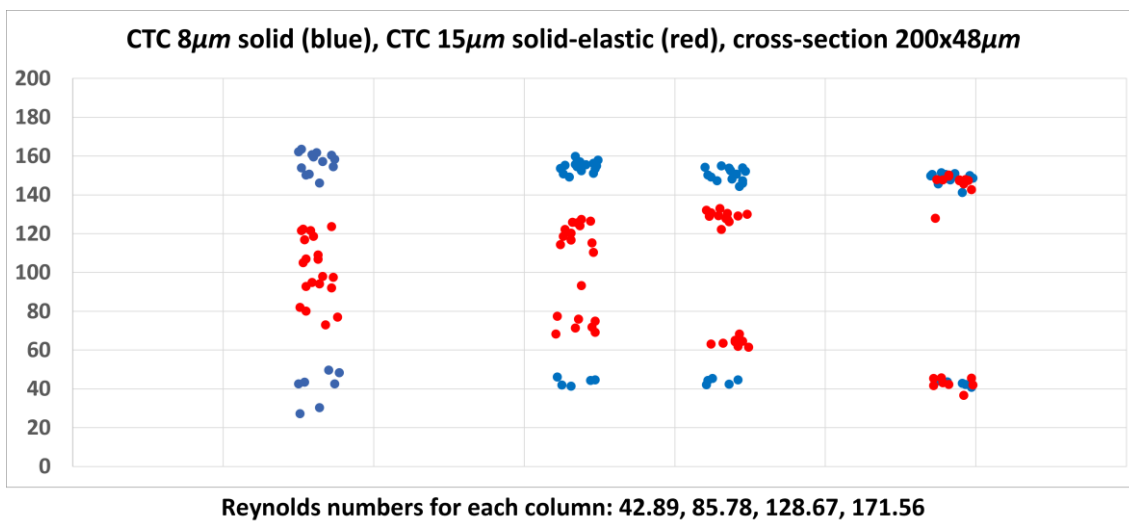


Figure 85: Comparison between different cells using cross-section $200 \times 48\mu\text{m}$ after 40 S-section passes

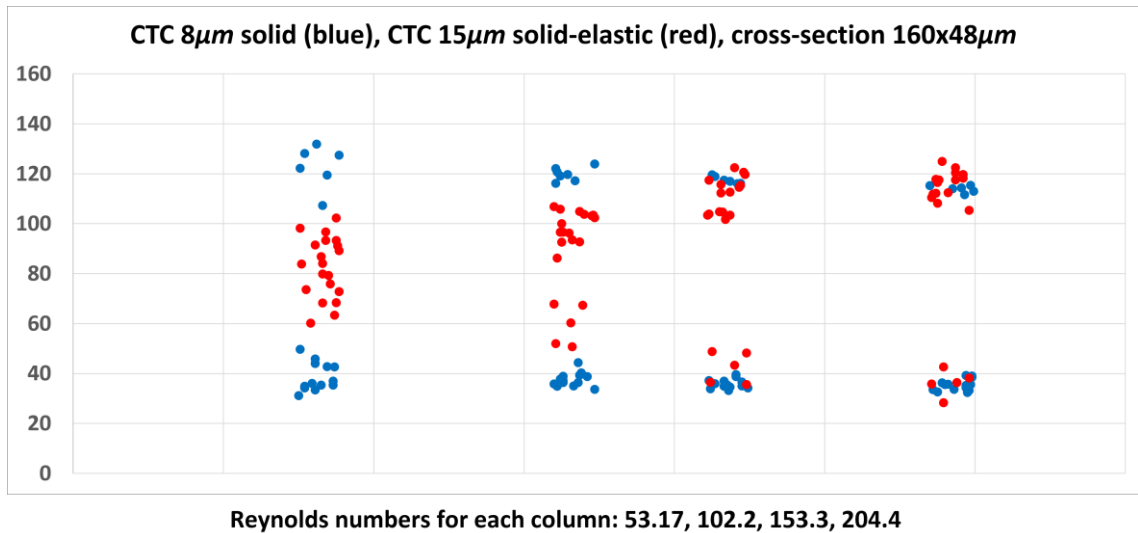


Figure 86: Comparison between different cells using cross-section 160x48 μ m after 40 S-section passes

In the case of a cross-section measuring 200x48 μ m in Figure 85, an interesting observation emerges at the lowest fluid velocity corresponding to $Re = 42.89$. The larger and more elastic cells tend to cluster closer to the centre of the channel, while the smaller solid cells are predominantly located along the channel edges. This spatial distribution suggests a potential for effective separation between the two cell types. However, as the fluid velocity increases there is a noticeable shift with the larger cells becoming increasingly concentrated nearer to the channel walls. Consequently, this trend gradually reduces the possibility of effective separation between the larger and smaller cells.

Figure 86 exhibits similar cell behaviour observed when utilizing a 160x48 μ m cross-section. In particular, at the lowest fluid velocity corresponding to $Re = 53.17$, there appeared to be a plausible possibility of cell separation. However, as the fluid velocity increased, the likelihood of mutual cell separation decreased.

A comparative analysis between the two channels reveals that the 200x48 μ m cross-section provides more ample space within its channel width, thus facilitating the potential stabilization of cell flow compared to the 160x48 μ m cross-section. This discrepancy is also reflected in the results, wherein the 160x48 μ m cross-section exhibits a greater dispersion of cells across the channel width compared to its counterpart. The most discernible distinction is observed at the slowest fluid velocity, despite the values being slightly disparate.

5.10 Conclusion

In the following subsections, we describe the conclusions drawn from three previous experiments on Dean inertial flows.

5.10.1 Inertial focusing and separation using initial geometry

In previous computational analyses of particle and cell flow within an S-shaped channel featuring various cross-sections, a broad spectrum of cell sizes and cluster types were considered. Comprehensive computational results were obtained through multiple approaches.

To investigate the influence of cell composition on their trajectories in S-shaped channels, calculations were performed with four different clusters in two scenarios: one with four clusters of equal volume and another with clusters composed of cells of equal size. In both scenarios, we observed that four-in-line clusters and tetrahedral clusters exhibited very similar behaviour, making them indistinguishable. A notable observation was that the only differences between clusters were seen in the cross section $60 \times 52\mu\text{m}$.

The explanation for the uniform behaviour of all clusters can be attributed to the narrowness of the channel for relatively large clusters. These clusters did not have the necessary space to rotate. The finding that the only discernible difference was in the $60 \times 52\mu\text{m}$ cross section supports this explanation, as this channel has the greatest height, providing the most space for clusters to rotate.

5.10.2 Inertial focusing and separation using larger geometry

The basis of this study is rooted in the principles of inertial flows, specifically Dean flows. Using these flows, we were able to observe the gradual stabilisation of clusters within a microfluidic channel after several passes, either at the centre or at the edges of the channel. This phenomenon became the focus for studying the separation dynamics of cell clusters, influenced by their inherent properties and the characteristics of the environment within the model.

Initially, our work focused on a microfluidic channel model with an S-shaped configuration with rounded edges to facilitate smoother fluid flow.. Subsequently, we introduced new channel geometries with dimensions of $160 \times 80\mu\text{m}$ and $200 \times 64\mu\text{m}$, providing increased space for the stabilization of cell clusters.

Our primary focus was on investigating a simple cluster composed of a single cell, and a two-in-line cluster formed by two cells. Fluid was introduced at four different velocities, represented by the Reynolds numbers $Re = 19.2, 37.3, 48, \text{ and } 64$, releasing clusters with varying cell diameters of $10, 15, \text{ and } 20\mu\text{m}$. These clusters also exhibited two distinct elasticities - some were solid ($k_s = 1.0$), while others were elastic ($k_s = 0.5$), allowing for greater deformation during the simulation.

In terms of computational complexity, each simulation was run for 3 to 7 days until each cluster reached a specified number of passes, typically 40 passes. In cases where additional time was required for the clusters to stabilise, the number of passes was increased to 80.

The numerical data detailing the cluster positions from each simulation was meticulously analysed using appropriate graphs. The graphs produced provided clear insights into the stabilisation tendencies of the clusters - whether they favoured the edges or the central part of the channel in terms of the y-axis. In particular, certain combinations of CTC and cluster sizes and elasticities suggested a high probability of separation.

5.10.3 MIT Research group collaboration

Establishing a collaboration with the MIT group was a major step forward, allowing for the first-time direct validation of our simulation results through biological experiments. A critical aspect of this collaboration was to align our microfluidic channel designs with their experimental capabilities.

Initially, we focused on defining common dimensions for the microfluidic channels, specifically the Y and Z dimensions to express the cross-section ratio. We chose cross sections of $250 \times 48\mu\text{m}$, $200 \times 48\mu\text{m}$ and $160 \times 48\mu\text{m}$ for investigation. In addition, we wanted to match the fluid velocities as closely as possible to those found in human blood vessels. We therefore chose four different velocities, expressed as Reynolds numbers. Given the variation in cancer cell diameter (from $8\mu\text{m}$ to $15\mu\text{m}$) and their elasticity, we selected both sizes for investigation, prioritising larger cells to account for higher elasticity.

We then compared the results of our simulations and the MIT group's experiments, initially focusing on a $250 \times 48\mu\text{m}$ cross-section, two fluid velocities, and 40 $8\mu\text{m}$ solid cells. To facilitate comparison, we transformed their video results into graphical representations, which showed a close correspondence between our results. Due to the limitations of the biological experiment, cells were allowed to pass through the S-section a maximum of 8 times. At lower fluid velocities, cell flow was uniform across the channel width, whereas at

higher velocities, cell flow stabilised closer to the channel walls, suggesting a potential for cell separation. For the $200 \times 48 \mu\text{m}$ and $160 \times 48 \mu\text{m}$ cross sections, we relied on our simulations due to the challenges associated with creating and running experiments with such microfluidic channels. Here we added 20 larger cells of $15 \mu\text{m}$ diameter to the 20 smaller cells. We selected four different fluid velocities for each of the cross sections. We evaluated the results after 40 S-section passes. Remarkably, our simulation results mirrored previous findings, with larger and more elastic cells concentrating towards the channel centre and smaller solid cells accumulating along the channel walls. In addition, increasing fluid velocity caused cells, including larger ones initially located in the centre, to concentrate along the channel edges.

6 DISCUSSION

The thesis covers a wide range of topics, leaving ample room for further experimentation and exploration of new areas. It focuses primarily on addressing critical issues related to cancer, a pernicious disease that claims a significant number of lives worldwide every day. Despite extensive research efforts, a universal cure for cancer remains elusive, underscoring the urgent need for innovative approaches to prevention, mitigation and eradication.

One potential avenue for future solutions lies in the field of microfluidic devices, which could revolutionise cancer treatment by offering less invasive, cost-effective and time-efficient alternatives to current modalities such as chemotherapy. These devices, when strategically placed in the human body, hold the promise of inhibiting the spread of cancer through a variety of mechanisms. In this context, our research has primarily focused on investigating different microfluidic devices, with a particular emphasis on cancer cell clusters. These clusters pose a greater threat than individual cancer cells due to their increased ability to survive in the body, making them more difficult to eliminate. Our research efforts are divided into three main areas:

1. Shear flow and narrow capillaries
2. Bifurcations
3. Dean flow

In the first part of our research, we focused primarily on observing the behaviour of cancer cell clusters under varying shear flow conditions, with particular emphasis on the number of contacts and the size of the contact area. Understanding these dynamics is crucial because the likelihood of metastasis in human blood vessels increases with the intensity and size of contacts between cancer cell clusters and the vessel walls. Similarly, when a cancer cell cluster encounters a constricted capillary, it may deform and rearrange its cells to pass through, potentially contacting the vessel walls in the process.

Following on from this premise, the second part of our research looked more closely at the behaviour of cell clusters when they hit the centre of dividing walls in microfluidic channels. This scenario mirrors real life processes where cell clusters navigate through junctions and impact channel walls. We investigated the intensity and size of contact areas between cell clusters and channel walls after impact, shedding light on the mechanisms at play in such scenarios.

Discussion

However, the bulk of our research was in the third section, where we explored the potential of using inertial and Dean flows to separate different types of cancer cells and clusters. The idea was to develop microfluidic devices capable of separating and trapping individual healthy cells from malignant cancer cell clusters. By collaborating with the MIT research group, we gained valuable insights into live microfluidic devices, which further enhanced our understanding. The remarkable agreement between our group's results and those of the MIT group represents a significant step forward and underlines the importance of ongoing collaboration for the advancement and application of cell cluster research.

6.1 Contribution of this thesis

The main contribution that this dissertation makes to applied computer science can be summarized in the following points:

- The design and creation of the following models of cancer cell clusters:
 - A simple cluster formed by two cells
 - A cluster formed by three cells
 - A cluster formed by four cells in the shape of a chain and a tetrahedron
- Detailed analysis of the behaviour of cancer cells and cell clusters in
 - Shear flow
 - Constricted capillaries
 - Bifurcated channels
 - Inertial flows
- Substantial calibration of coefficients related to:
 - Cell membrane elasticity
 - Lennard-Jones interactions between cells
- Design and development of appropriate channel models:
 - With constricted capillaries
 - With simple bifurcation
 - S-shaped with rounded edges
- Graphical, quantitative or qualitative representation and intercomparison of all results obtained

All published results obtained within the scope of the thesis are listed at the end of the document in the "Attachments" section.

6.2 Future research directions

Informatics is playing an increasingly important role in biomedicine, serving as an indispensable tool for driving progress and innovation. The integration of informatics into modern biomedical research has been transformative, enabling advances that would otherwise have been unattainable. In this dynamic landscape, the pursuit of novel approaches and interdisciplinary connections serves to enrich both fields, with the only limit being our imagination.

For our research group, this means a wealth of topics to explore, as evidenced by the breadth of our thesis, which encompasses three major areas for future investigation. Our research efforts are constrained not only by the availability of information from published biological experiments, but also by the capabilities of our software. As the ESPResSo software continues to evolve, we anticipate the opportunity to adopt new methodologies and take our research forward.

We are currently collaborating with a leading research group at MIT through the Global Seeds Slovakia programme. The MIT group specialises in microfluidic devices with a focus on cell deformation and cancer cell separation. Together we are investigating the use of inertial flow for cell suspension separation to validate our results and develop new channel prototypes.

Our collaboration extends beyond research activities to include joint meetings and discussions, fostering a rich exchange of ideas. Through first-hand exposure to MIT's advanced technologies, we have gained invaluable insight and experience. Initial comparisons of our results have shown promising alignment, guiding our next steps in collaborative research.

Following the successful collaboration, we plan to document our procedures and results in a comprehensive paper that will contribute to the advancement of both fields. Beyond publication, our future efforts will include modelling microfluidic channels and cell clusters to address unanswered questions and further our understanding.

In conclusion, the future of microfluidic devices is very promising and we anticipate that continued collaboration and exploration will lead to significant advances. By joining forces with other research groups, we aim to collectively advance our knowledge and ultimately contribute to a successful cure for cancer.

7 REFERENCES

- [1] Cell-in-fluid Biomedical Modelling and Computation Group, *Research group webpage*, January, 2020, <http://cellinfluid.fri.uniza.sk>.
- [2] K. J. Anderson, A. de Guillebon, A. D. Hughes, W. Wang and M. R. King, "Effect of circulating tumor cell aggregate configuration on hemodynamic transport and wall contact," *Mathematical Biosciences*, no. 294, pp. 181-194, 2017.
- [3] S. H. Au, B. D. Storey, J. C. Morre, Q. Tang and et. al., "Clusters of circulating tumor cells traverse capillary-sized vessels," *Proceedings of the National Academy of Sciences of the United States of America*, no. 113, p. 4947–4952, 2016.
- [4] Y. Hong, F. Fang and Q. Zhang, "Circulating tumor cell clusters: What we know and what we expect," *International journal of oncology*, vol. 49, p. 2206–2216, 2016.
- [5] M. E. Warkiani, G. Guan, K. B. Luan, W. C. Lee, A. A. S. Bhagat, P. Kant Chaudhuri, D. S.-W. Tan, W. T. Lim, S. C. Lee, P. C. Y. Chen, C. T. Lim and J. Han, "Slanted spiral microfluidics for the ultra-fast, label-free isolation of circulating tumor cells," *Lab Chip*, vol. 14, pp. 128-137, 2014.
- [6] N. Aceto, A. Bardia, D. T. Miyamoto and et al., "Circulating tumor cell clusters are oligoclonal precursors of breast cancer metastasis," *Cell*, vol. 158, p. 1110–1122, 2014.
- [7] S. Regmi, A. Fu and K. Q. Luo, "High Shear Stresses under Exercise Condition Destroy Circulating Tumor Cells in a Microfluidic System," *Nature Scientific Reports*, vol. 7, 2017.
- [8] D. G. Duda, A. M. Duyverman and M. e. a. Kohno, "Malignant cells facilitate lung metastasis by bringing their own soil," *Proc Natl Acad Sci U S A*, vol. 107, pp. 21677-21682, 2010.
- [9] J. F. Edd, A. Mishra, T. D. Dubash, S. Herrera, R. Mohammad, E. K. Williams, X. Hong, B. R. Mutlu, J. R. Walsh, F. M. de Carvalho and others, "Microfluidic concentration and separation of circulating tumor cell clusters from large blood volumes," *Lab on a Chip*, vol. 20, p. 558–567, 2020.
- [10] M. Daoudi, E. Lavergne, A. Garin, N. Tarantino, P. Debre, C. F. C. Pincet and P.

References

- Deterre, "Enhanced adhesive capacities of the naturally occur-," *J Biol Chem*, vol. 279, no. 19, pp. 19649-57, 2004.
- [11] M. Pepona, P. Balogh, F. P. Puleri, W. F. Hynes, C. Robertson, K. Dubbin, J. Alvarado, M. L. Moya and A. Randles, "Investigating the Interaction Between Circulating Tumor Cells and Local Hydrodynamics via Experiment and Simulations," *Cellular and Molecular Bioengineering*, vol. 13, p. 527–540, 2020.
- [12] P. Balogh and P. Bagchi, "Analysis of red blood cell partitioning at bifurcations in simulated microvascular networks," *Physics of Fluids*, vol. 30, p. 051902, 2018.
- [13] K. Hood, S. Lee and M. Roper, "Inertial migration of a rigid sphere in three-dimensional Poiseuille flow," *J. Fluid Mech.*, vol. 765, p. 452–479, February 2015.
- [14] X. Xu, X. Huang, J. Sun, R. Wang, J. Yao, W. Han, M. Wei, J. Chen, J. Guo, L. Sun and others, "Recent progress of inertial microfluidic-based cell separation," *Analyst*, vol. 146, p. 7070–7086, 2021.
- [15] N. Nivedita, P. Ligrani and I. Papautsky, "Dean flow dynamics in low-aspect ratio spiral microchannels," *Scientific Reports*, vol. 7, p. 44072, 2017.
- [16] N. Liu, C. Petchakup, H. M. Tay, K. H. H. Li and H. W. Hou, "Spiral inertial microfluidics for cell separation and biomedical applications," *Applications of Microfluidic Systems in Biology and Medicine*, p. 99–150, 2019.
- [17] N. Xiang and Z. Ni, "Inertial microfluidics: current status, challenges, and future opportunities," *Lab on a Chip*, vol. 22, p. 4792–4804, 2022.
- [18] S. Tripathi, A. Kumar, Y. V. Bala Varun Kumar and A. Agrawal, "Three-dimensional hydrodynamic flow focusing of dye, particles and cells in a microfluidic device by employing two bends of opposite curvature," *Microfluidics and Nanofluidics*, vol. 20, p. 1–14, 2016.
- [19] J. Zhang, S. Yan, W. Li, G. Alici and N.-T. Nguyen, "High throughput extraction of plasma using a secondary flow-aided inertial microfluidic device," *RSC Adv.*, vol. 4, no. 63, pp. 33149-33159, 2014.
- [20] A. Bugáňová and I. Cimrák, "Computational Study of Particle Separation Based on Inertial Effects in Rectangular Serpentine Channels with Different Aspect Ratios," in *Proceedings of the 16th International Joint Conference on Biomedical Engineering Systems and Technologies (BIOSTEC 2023) - Volume 3: BIOINFORMATICS*, 2023.

- [21] T. Tanaka, T. Ishikawa, K. Numayama-Tsuruta, Y. Imai, H. Ueno, N. Matsuki and T. Yamaguchi, "Separation of cancer cells from a red blood cell suspension using inertial force," *Lab Chip*, vol. 12, p. 4336–4343, November 2012.
- [22] D. R. Gossett, H. T. K. Tse, S. A. Lee, Y. Ying, A. G. Lindgren, O. O. Yang, J. Rao, A. T. Clark and D. D. Carlo, "Hydrodynamic stretching of single cells for large population mechanical phenotyping," *Proceedings of the National Academy of Sciences*, vol. 109, pp. 7630-7635, 2012.
- [23] F. Weik, R. Weeber, K. Szuttor, K. Breitsprecher, J. de Graaf, M. Kuron, J. Landsgesell, H. Menke, D. Sean and C. Holm, *ESPResSo 4.1 - An extensible software package for simulating soft matter systems*, GitHub, 2020.
- [24] T. Krueger, H. Kusumaatmaja, A. Kuzmin and E. Viggien, "The Lattice Boltzmann Method - Principles and Practice," *Springer*, 2017.
- [25] M. Bušík, M. Slavík and I. Cimrák, "The Lattice Boltzmann Method - Principles and fluid and immersed objects for modelling of cells in flow.," *Computational and Mathematical Methods in Medicine*, no. 7842857, 2018.
- [26] I. Cimrák, M. Gusenbauer and I. Jančigová, "An ESPResSo implementation of elastic objects immersed in a fluid," *Computer Physics Communications*, vol. 185, pp. 900-907, 2014.
- [27] I. Jančigová, K. Kovalčíková, R. Weeber and I. Cimrák, "PyOIF: Computational tool for modelling of multi-cell flows in complex geometries," *PLOS Computational Biology*, vol. 16, pp. 1-21, October 2020.
- [28] A. Bohiniková, I. Jančigová, I. Cimrák and J. J. Feng, "Sensitivity analysis of adhesion in computational model of elastic doublet," *Springer International Publishing*, pp. 220-233, 2022.
- [29] I. Jančigová, K. Kovalčíková, A. Bohiniková and I. Cimrák, "Springnetwork model of red blood cell: From membrane mechanics to validation," *International Journal for Numerical Methods in Fluids*, 2020.
- [30] A. Bohiniková and K. Bachratá, "Calibration of Circulating Tumor Cell's Model in Narrow Flow," *EPJ Web of Conferences*, no. 02006, p. 213, 2019.
- [31] A. Bohiniková, I. Jančigová and I. Cimrák, "Modeling red blood cell viscosity contrast using inner soft particle suspension," *Micromachines*, vol. 12, no. 8, p. 974, 2021.

References

- [32] I. Jančigová, M. Mulík and I. Cimrák, "Contact area of cell cluster in a simple bifurcation," *2022 ELEKTRO (ELEKTRO)*, pp. 1-5, 2022.
- [33] I. Jančigová, A. Bohiníková, M. Mulík and I. Cimrák, "Modelling cell clusters and their near-wall dynamics in shear flow," *Computational Particle Mechanics*, no. 10, pp. 991-1004, 2023.
- [34] E. Schuster, R. Taftaf, C. Reduzzi, M. K. Albert, I. Romero-Calvo and H. Liu, "Better together: circulating tumor cell clustering in metastatic cancer," *Trends in Cancer*, vol. 7, no. 11, pp. 1020-1032, 2021.
- [35] G. Bendas and L. Borsig, "Cancer cell adhesion and metastasis: selectins, integrins, and the inhibitory potential of heparins.," *Int.J.Cell Biol.*, no. 10, 2012.
- [36] A. Henderson, "ParaView Guide, A Parallel Visualization Application," 2007.
- [37] W. Schroeder, K. Martin and B. Lorensen, *The Visualization Toolkit (4th ed.)*, Kitware, 2006.
- [38] S. Regmi, A. Fu and K. Q. Luo, "Aby sme kvantifikovali prítomnosť buniek v blízkosti stien, merali sme adhézy potenciál rolovania zhlukov v blízkosti steny vyhodnotením metrik zahŕňajúcich čas kontaktu a kontaktnú plochu.," *Nature Scientific Reports*, no. 7, p. 39975, 2017.
- [39] S. H. Au, J. Edd, A. E. Stoddard, K. H. K. Wong, F. Fachin, S. Maheswaran, D. A. Haber, S. L. Stott, R. Kapur and M. Toner, "Microfluidic isolation of circulating tumor cell clusters by size and asymmetry," *Scientific reports*, vol. 7, p. 1–10, 2017.
- [40] J. L. Maitre, H. Berthoumieux, S. F. Krens, G. Salbreux, F. Julicher, E. Paluch and C. Heisenberg, "Adhesion functions in cell sorting by mechanically coupling the cortices of adhering cells," *Science*, vol. 338, no. 6104, pp. 253-256, 2012.
- [41] M. A. Panteleev, N. Korin, K. D. Reesink, D. L. Bark, J. E. Cosemans, E. E. Gardiner and P. H. Mangin, "Wall shear rates in human and mouse arteries: Standardization of hemodynamics for in vitro blood flow assays: Communication from the isth ssc subcommittee on biorheology.," *Journal of Thrombosis and Haemostasis*, vol. 19, no. 2, pp. 588-595, 2021.
- [42] H. Bate, "Blood viscosity at different shear rates in capillary tubes," *Biorheology*, vol. 14, no. 5-6, pp. 267-275, 1977.

- [43] M. Bert, S. Lang, M. Dominiotto, M. Rudin, G. Schulz, H. Deyhle, M. Germann, F. Pfeiffer, C. David and T. Weitkamp, "High-resolution tomographic imaging of microvessels," *Proc SPIE*, no. 7078, p. 70780B, 2008.
- [44] N. Xiang, J. Wang, Q. Li, Y. Han, D. Huang and Z. Ni, "Precise size-based cell separation via the coupling of inertial microfluidics and deterministic lateral displacement," *Analytical chemistry*, vol. 91, p. 10328–10334, 2019.
- [45] Y. Ying and Y. Lina, "Inertial Focusing and Separation of Particles in Similar Curved Channels," *Scientific reports, nature research*, vol. 391, p. 123570, 2020.
- [46] J.-P. Matas, J. F. Morris and É. Guazzelli, "Lateral force on a rigid sphere in large-inertia laminar pipe flow," *J. Fluid Mech.*, vol. 621, p. 59–67, February 2009.
- [47] J. M. Martel and M. Toner, "Inertial focusing in microfluidics," *Annu. Rev. Biomed. Eng.*, vol. 16, p. 371–396, July 2014.
- [48] M. Mulik and Cimrak Ivan, "Particle and Cell Cluster Separation Based on Inertial Effects in Rectangular Serpentine Channels.," *In Proceedings of the 17th International Joint Conference on Biomedical Engineering Systems and Technologies*, vol. 1, pp. 553-560, 2024.

ATTACHMENTS

List of Attachments

- List of publications
- CD with dissertation thesis

LIST OF PUBLICATIONS

I. Jančigová, M. Mulík and I. Cimrák, “Contact area of cell cluster in a simple bifurcation,” 2022 ELEKTRO (ELEKTRO), pp. 1-5, 2022.

I. Jančigová, A. Bohiníková, M. Mulík and I. Cimrák, “Modelling cell clusters and their near-wall dynamics in shear flow,” Computational Particle Mechanics, no. 10, pp. 991-1004, 2023.

M. Mulik and Cimrak Ivan, “Particle and Cell Cluster Separation Based on Inertial Effects in Rectangular Serpentine Channels.,” In Proceedings of the 17th International Joint Conference on Biomedical Engineering Systems and Technologies, vol. 1, pp. 553-560, 2024.